Nickel-based Nanomaterials for Electrochemical Supercapacitors

Dissertation by

Nuha Alawi Alhebshi

In Partial Fulfillment of the Requirements

For the Degree of

Doctor of Philosophy (Ph.D.) in Materials Science and Engineering

King Abdullah University of Science and Technology

Thuwal, Kingdom of Saudi Arabia

November 2015

The Ph.D. dissertation of Nuha Alawi Alhebshi is approved by the examination committee.

Committee Chairperson

Prof. Husam Niman Alshareef

Committee Members

Prof. Hala Abdulaziz Aljawhari

Prof. Iman Salem Roqan

Prof. Khaled Nabil Salama

Prof. Osman Mohammad Bakr

© November 2015

Nuha Alawi Alhebshi

All Rights Reserved

ABSTRACT

Nickel-based Nanomaterials for Electrochemical Supercapacitors

Nuha Alawi Alhebshi

The demand for energy storage technologies is rapidly increasing in portable electronics, transportation, and renewable energy systems. Thus, the objective of this research is to develop and enhance the performance of Ni-based electrochemical supercapacitors by optimizing synthesis conditions and design of the electrode materials. Conventional and on-chip supercapacitors were developed with notable performance enhancement.

For conventional supercapacitors, a uniform and conformal coating process was developed to deposit $Ni(OH)_2$ nanoflakes on carbon microfibers *in-situ* by a simple chemical bath deposition at room temperature. The microfibers conformally-coated with $Ni(OH)_2$ make direct physical contacts with essentially every single nanoflakes, leading to more efficient electron transport. Using this strategy, we have achieved devices that exhibit five times higher specific capacitance compared to planar (non-conformal) $Ni(OH)_2$ nanoflakes electrodes prepared by drop casting of $Ni(OH)_2$ on the carbon microfibers (1416 F/g vs. 275 F/g).

For on-chip storage applications, microfabricated supercapacitors were developed using a combination of top-down photolithography and bottom-up CBD. The resulting $Ni(OH)_2$ micro-supercapacitors show high-rate redox activity

up to 500 V/s and an areal cell capacitance of 16 mF/cm^2 corresponding to a volumetric stack capacitance of 325 F/cm^3. This volumetric capacitance is 2-fold higher than carbon and metal oxide based micro-supercapacitors. Furthermore, these micro-supercapacitors show a maximum energy density of 21 mWh/cm^3, which is superior to the Li-based thin film batteries.

To enhance cycling stability, Ni-Cu-OH and Ni-Co-OH ternary electrodes have been prepared with different Ni:Cu and Ni:Co ratios by CBD at room temperature on carbon microfibers. It is observed that the electrodes with Ni:Cu and Ni:Co composition ratio of 100:10 results in an optimum capacitance and cycling stability. For the optimum composition, Ni-Co-OH with graphene and carbon nanofibers electrode was tested, with resultant improvement in electrode potential window, equivalent series resistance, and cyclic stability.

To further increase energy density, $Ni(OH)_2$//Graphene asymmetric supercapacitor were fabricated with areal capacitance of 253 mF/cm^2 at 5 mA/cm^2 which is higher than NiO//rGO prepared by hydrothermal method. Ni-Co-OH/G-CNF//Graphene asymmetric supercapacitor results in a maximum power of 23 mW within an operating voltage of 2.2 V which are higher than of $Ni(OH)_2$//Graphene (15.94 mW within 1.8 V). Our asymmetric supercapacitors have flexible-electrodes, low-cost fabrication process and environmentally friendly materials.

ACKNOWLEDGEMENTS

I would like to thank my advisor, Prof. Husam Alshareef. My Ph.D. research could not be done without his valuable guidance and continued support. It was a great opportunity for me to work in his advanced laboratory: Functional Nanomaterials and Devices Laboratory. I acknowledge collaborations and discussions with Dr. Narendra Kurra and Dr. Rakhi Raghavan-Baby, both of whom are post-docs in our group.

In addition, it is an honor for me to have several distinguished faculty in my Ph.D. examination committee, including Prof. Hala Aljawhari, Prof. Iman Roqan, Prof. Khaled Salama, and Prof. Osman Bakr. I appreciate their valuable comments on my Ph.D. proposal and dissertation.

Last but not least, I offer my sincere gratitude to my parents, Alawi Alhebshi and Ameerah Ageel for their continues care and unconditional love.

TABLE OF CONTENTS

LIST OF ABBREVIATIONS

AC	Activated carbon
BET	Brunauer-Emmett-Teller
CBD	Chemical bath deposition
CD	Charge-discharge
CV	Cyclic voltammetry
DI	Deionized
EDLC	Electrical double layer capacitors
EIS	Electrochemical impedance spectroscopy
FC	Faradic capacitors
G-CNF	Graphene-carbon nanofibers
LED	Light emitting diode
$Ni(OH)_2$	Nickel hydroxide
Ni-Co-OH	Nickel-cobalt hydroxides
Ni-Cu-OH	Nickel-copper hydroxides
PEN	Polyethylene naphthalate
rGO	Reduced graphene oxide
SAED	Selected area electron diffraction
SEM	Scanning electron microscope
SCE	Saturated calomel electrode
TEM	Transmission electron microscope
TMAH	Retra-methyl-ammonium-hydroxide
XRD	X-ray diffraction

LIST OF SYMBOLS

a	Alpha-phase
β	Beta-phase
ε	Dielectric permittivity
γ	Gamma-phase
μ	Micro
Ω	Ohm
Δt	Time interval
ΔV	Voltage interval
C	Capacitance
C_A	Areal capacitance
C_s	Specific capacitance
E	Energy
I	Current
m	Mass
P	Power
Q	Charge

LIST OF FIGURES

LIST OF TABLES

LIST OF PUBLICATIONS

1. Nuha A. Alhbeshi and H. N. Alshareef, *Flexible and low-cost asymmetric supercapacitors based on Ni-Co-OH and Graphene-carbon Nanofibers Electrodes*, to be submitted.

2. Nuha A. Alhebshi and H. N. Alshareef, *Ternary Ni-Cu-OH and Ni-Co-OH Electrodes for Electrochemical Energy Storage*, **Materials for Renewable and Sustainable Energy**, 4(4), 1-9, doi: 10.1007/s4024301500647 (2015).

3. N. Kurra*, Nuha A. Alhebshi* and H. N. Alshareef, *Microfabricated Pseudocapacitors Using $Ni(OH)_2$ Electrodes Exhibit Remarkable Volumetric Capacitance and Energy Density*. **Advanced Energy Materials**, 5, 1401303, doi: 10.1002/aenm.201401303 (2015), *Contributed equally.

4. R. B. Rakhi, Nuha A. Alhebshi, D. H. Anjum and H. N. Alshareef, *Nanostructured cobalt sulfide-on-fiber with tunable morphology as electrodes for asymmetric hybrid supercapacitors*. **Journal of Materials Chemistry A**, 2, 16190-16198, doi: 10.1039/C4TA03341H (2014).

5. Nuha A. Alhebshi, R. B. Rakhi and H. N. Alshareef, *Conformal coating of $Ni(OH)_2$ nanoflakes on carbon fibers by chemical bath deposition for efficient supercapacitor electrodes*. **Journal of Materials Chemistry A**, 1, 14897-14903, doi: 10.1039/C3TA12936E (2013).

Chapter 1 . INTRODUCTION

1.1. MOTIVATION

The demand for electrical energy storage devices, batteries and electrochemical supercapacitors is rapidly increasing in many crucial applications such as portable electronics, electric transportations and renewable energy systems. In fact, the global market for electrochemical supercapacitors is currently valued in the hundreds of millions of dollars, and it is expected to continue to grow as demonstrated in **Figure 1.1** and **Figure 1.2**.[1,2] Therefore improved energy storage systems need to be developed.

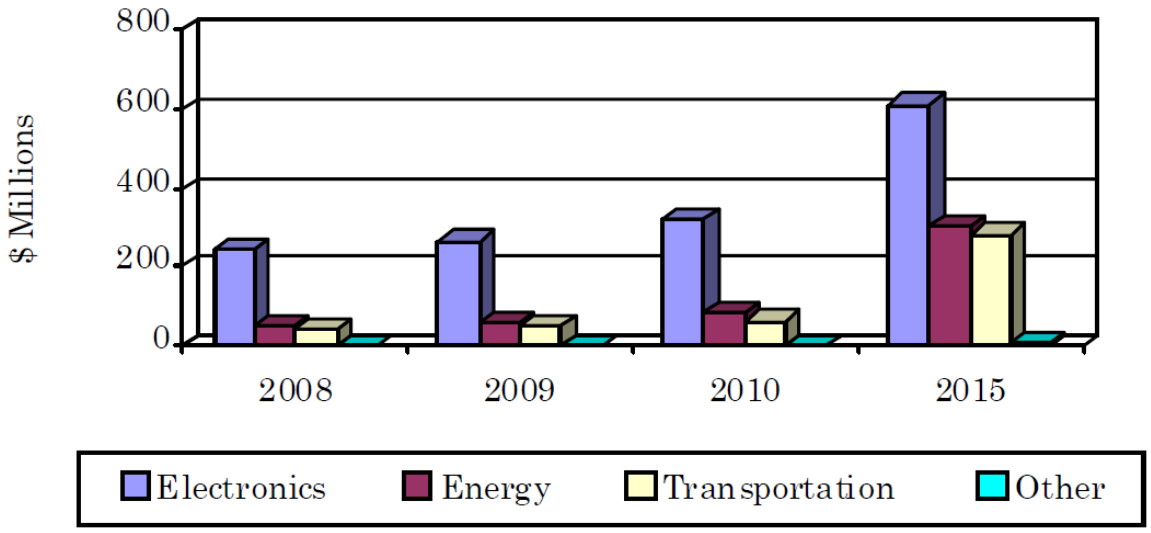

Figure 1.1 Global market for electrochemical supercapacitors, 2008-2015. Source: BCC Research.[1]

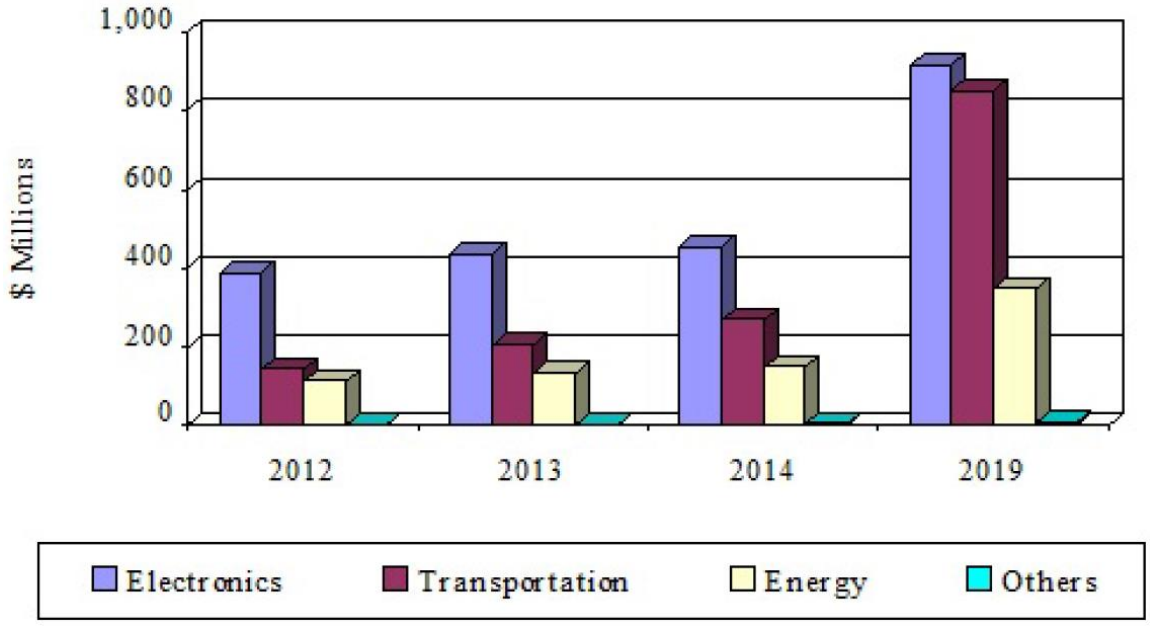

Figure 1.2 Global market for electrochemical supercapacitors, 2012-2019. Source: BCC Research.[2]

Electrochemical supercapacitors can be useful in many applications either as stand-alone (e.g., in regenerative braking systems) or in combination with batteries (e.g., in electric vehicles).[3] In addition, electrochemical supercapacitors find applications as uninterruptible power supplies, DC power systems, mobile devices and rechargeable toy and camera motors. As a specific example, electrochemical supercapacitors are considered an alternating power source in solar watches where electrochemical supercapacitors power the watch for several nights after being completely charged during days.[4]

1.2. BACKGROUND

Electrochemical supercapacitors are energy storage devices that electrochemically store electrical charges with superior capacitance than that

of electrostatic capacitors. Electrostatic capacitors consist of two parallel conductive sheets, called electrodes, separated by an insulator, called dielectric. When a voltage difference is applied between the electrodes, the dielectric will be polarized. Therefore, electrical energy is stored on the electrodes by electrostatic force.[5] The capacitance of parallel-plate electrostatic capacitors can be calculated by:

$$\mathbf{C} = \frac{\mathbf{A\varepsilon}}{\mathbf{d}} \qquad \textbf{Equation 1.1}$$

where *A* is electrode area, ε is dialectic permittivity and *d* is the distance between electrodes (the thickness of the dielectric). The capacitance of electrostatic capacitors ranges from nanofarads to millifarads, while the capacitance of electrochemical supercapacitors ranges from millifarads to kilofarads due to the superior surface area of porous electrodes used in electrochemical supercapacitors.[5]

Electrochemical supercapacitors can be classified into electrical double layer capacitors (EDLC) and Faradic capacitors (FC), also known as pseudocapacitors. In EDLC, electrical charges are held at the interfacial double layer between a porous electrode and a liquid electrolyte as illustrated in **Figure 1.3**.[5] Electrode materials used in EDLC should be porous with large surface to achieve larger capacitance, with the ideal pore size in the range of few nanometers.[5] The electrode material should also be electrically conducting to facilitate electron flow to the collector.

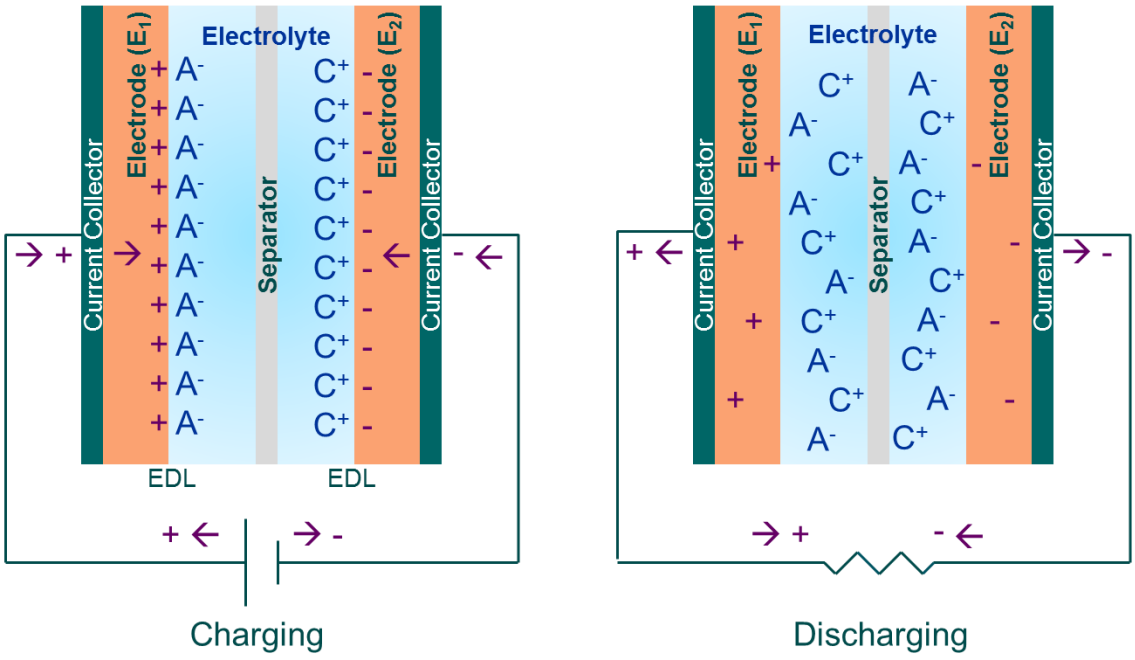

Figure 1.3 Sketch of electrical charge storage mechanism in EDLC.

In Faradic capacitors, electrical charges are stored through Faradic oxidation-reduction (redox) reactions depending upon the electrode potential as illustrated in **Figure 1.4**.[5] The preferred Faradic electrode materials should have multi-oxidation states in order to facilitate reversible oxidation and reduction during the charging and discharging processes. Due to the differences in the energy storage mechanisms between EDLC and FC, the latter normally exhibit higher capacitance but weaker cyclic stability than those of ELDC. The supercapacitor community has recently become interested in combining both porous materials and transition metals into the same electrode (called a hybrid electrode) in order to leverage the large surface areas of porous electrodes and the higher capacitance of some pseudocapacitive (Faradic) materials.

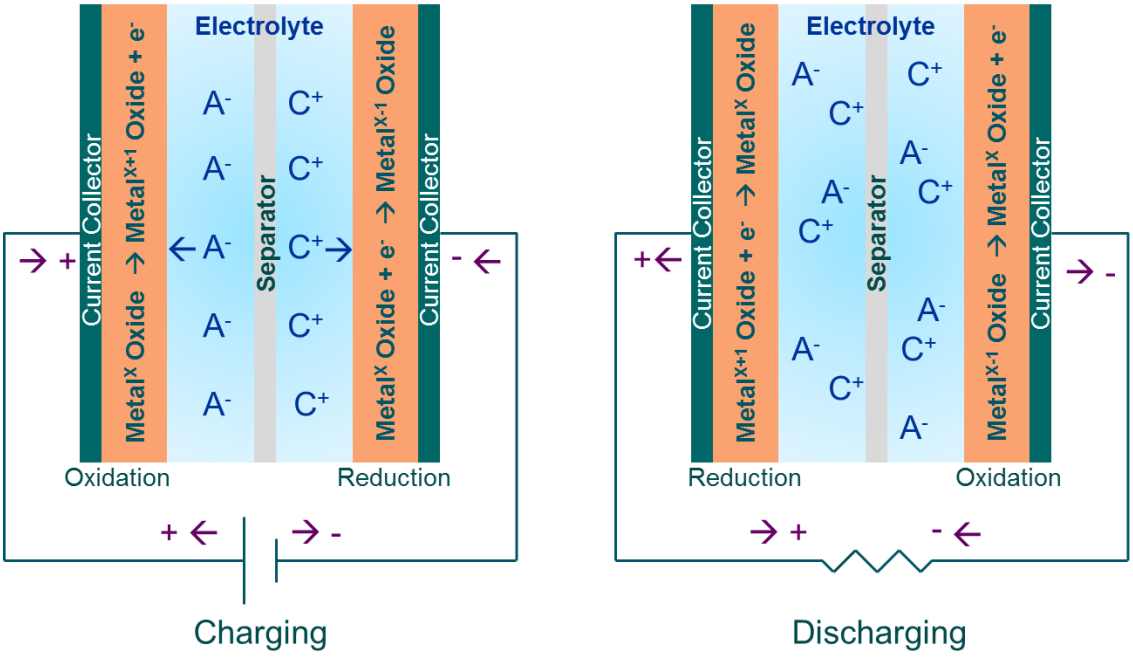

Figure 1.4 Sketch of electrical charge storage in FC.

1.3. LITERATURE REVIEW

Conducting porous materials such as graphene have been extensively investigated for both fundamental understanding and practical implementations in ELDC.[6,7] For FC, transition metal oxide/hydroxides and electrical conductive polymers have been intensively reported in the literature.[8-12] Among metal oxide electrode materials, RuO_2-based electrodes have the highest theoretical capacitance, but Ru metal is extremely expensive.[13] IrO_2-based electrodes are even more expensive than RuO_2.[14] MnO_2-based electrodes are cost-effective candidates but they have been extensively studied and results in lower capacitances than that of Ru_2O-based electrodes.[15] VO_x-based electrodes were also used but they are toxic materials.[16] MoO_3-based

electrodes exhibit lower specific capacitance than the previous oxides.[17] NiO-based electrodes[18,19] and Co_3O_4-based electrodes and their hydroxides[20] have higher specific capacitances than MnO_2 and MoO_3, lower cost than RuO_2, much lower toxicity than VO_x, and relatively fewer studies than MnO_2 -based electrodes.

Nickel hydroxide ($Ni(OH)_2$) is one of the most promising electrode materials for energy storage device due to its electrochemical redox reactivity,[21] natural abundance, environmental friendliness and low cost. $Ni(OH)_2$ has been typically used for alkaline rechargeable batteries because its Faradic discharge behavior is characterized by a flat (constant) voltage region over a long discharge time (in hours).[22] The electrical charges are stored on $Ni(OH)_2$ electrodes during Faradic oxidation-reduction reaction:

$$NiOOH + e^- + H_2O \leftrightarrow Ni(OH)_2 + OH^- \qquad \textbf{Equation 1.2}$$

The theoretical maximum specific capacity for one-electron reaction of $Ni(OH)_2$ battery electrodes is calculated by the following equation to be 290 mA.h/g :

$$C_S = \frac{n.F}{M} = \frac{96485\ [\mathrm{C/mol}]}{92.7\ [\mathrm{mol/g}]} = 1041[\mathrm{C/g}] = 290\ [\mathrm{mA.h/g}] \qquad \textbf{Equation 1.3}$$

Where C_s is capacity [mA.h/g], n is number of transferred electrons [e], F is Faraday constant [C/mol] and M is molar mass of electrode material [mol/g].

On the other hand, the supercapacitor behavior is recognized by the characteristic sloping curve of discharge voltage over short discharge time (in seconds).[5] Some battery materials, including $Ni(OH)_2$, show supercapacitor behavior when designed at the nanoscale or in thin film form because the electrolyte diffusion into the entire nanostructured or thin film electrodes is faster than into the bulk-structured electrodes.[23] This phenomenon is based on fact that nanomaterials and thin films have larger surface to volume ratio than bulk materials.

The theoretical maximum specific capacitance for one-electron reaction of $Ni(OH)_2$ supercapacitor electrodes are calculated by the following equation:

$$C_S = \frac{n.F}{M.E} = \frac{96485\ [\mathrm{C/mol}]}{92.7\ [\mathrm{mol/g}] \times 0.6\ [\mathrm{V}]} = 1735\ [\mathrm{F/g}] \qquad \textbf{Equation 1.4}$$

where E is electrode potential window [V] which is typically 0.6 V for $Ni(OH)_2$ electrodes in KOH aqueous electrolyte solution.

The main issue of $Ni(OH)_2$ electrodes is the capacitance decay during long charge-discharge (CD) cycling. For instance, a high specific capacitance of 2222 F/g at 1 A/g has been achieved using $Ni(OH)_2$ electrode, prepared by chemical bath deposition on nickel foam at room temperature, but with a capacitance retention of 62% after only 2000 CD cycles at 1 A/g.[24] It has been reported in the same study that the major contributor to such capacitance decay is the phase transformation from α-$Ni(OH)_2$/γ-NiOOH to β-$Ni(OH)_2$/β-NiOOH redox coupled phases, at relatively low discharge current densities.[24]

Table 1.1 Summary of published reports on $Ni(OH)_2$ electrodes prepared by hydrothermal and CBD.

Morphology	Synthesis Method	Specific Capacitance	Ref.
β-$Ni(OH)_2$ nanosheets	Solvothermal method	1528 F/g at 1 A/g	[25]
Coin-like β-$Ni(OH)_2$ nanoplates	Coordination homogeneous precipitation	1300 F/g at 1 A/g	[26]
β-$Ni(OH)_2$ cross-linked nanowalls	Hydrothermal treatment at 100 °C	2675 F/g at 0.005 A/cm^2.	[27]
β-$Ni(OH)_2$ hierarchical hollow microspheres	Hydrothermal 180 °C	1398.5 F/g at 0.005 A/cm^2	[28]
Honeycomb-like $Ni(OH)_2$ thin film	CBD at 60 °C on stainless steel substrates.	398 Fg at a scan rate of 5 mV/s	[29]
Interconnected honeycomb-like $Ni(OH)_2$	CBD at 70 °C on stainless steel substrates	296 F/g at 0.005 A/cm^2	[30]
Interconnected $Ni(OH)_2$ nanoflakes	CBD at 70 °C on stainless steel substrates	468 F/g at 0.005 A/cm^2	[30]
α-$Ni(OH)_2$ interconnected nanoflakes	CBD at room temperature on Ni foam	2200 F/g at 1 A/g, 40% drop after 2000 cycles	[24]
β-$Ni(OH)_2$ / α-NiOOH composite film	CBD at room temperature on Ni foam	1420 F/g at 1A/g, tested stability for 1000 cycles	[31]

There are several studies indicating that high specific capacitance can be achieved using $Ni(OH)_2$ electrodes prepared by hydrothermal synthesis method. However, one of the disadvantages of this method is that it is time consuming and has heightened sensitivity of oxide morphology to hydrothermal process conditions, which make it difficult to scale up to the industrial scale. Chemical bath deposition (CBD), on the other hand, is a much simpler process

and can be performed at room temperatures. It is also highly scalable suggesting that it has the potential to be more cost effective compared with other chemical synthesis methods. Substrates used in CBD can be conductive or nonconductive materials in contrast to those used in electrodeposition. The first study of using CBD for NiO preparation was carried out by Pramanik *et al.*[32] The chemical bath used in that study, an aqueous mixture of nickel sulfate, potassium persulfate and ammonia solution, was later used by others to prepare $Ni(OH)_2$ and NiO.[33] **Table 1.1** summarizes reported performance for $Ni(OH)_2$ electrochemical capacitors electrodes prepared by hydrothermal and CBD.

Table 1.2 Summary of published reports on Ni-Co-OH//graphene asymmetric supercpators that thier $Ni(OH)_2$ electrodes were prepared by CBD.

Positive //Negative Electrode	Synthesis Methods	Specific Capacitance	Voltage - Electrolyte	Ref.
$Ni(OH)_2$/CNT//rGO	Modified hummers method for CNT CBD for $Ni(OH)_2$	78.33 F/g At 2 A/g	1.8 V in KOH	34
$Ni(OH)_2$/CNT//AC	CVD for CNT CBD for $Ni(OH)_2$	110.6 F/g at 5 mA/cm^2	1.8 V in KOH	35
Ni-Co-OH//rGO	Chemical reduction for rGO CBD for Ni-Co-OH	84.3 F/g at 5 mV/s	1.5 V in KOH	36
Co_3O_4/$Ni(OH)_2$//rGO	Chemical reduction for rGO Hydrothermal for Co_3O_4 CBD for $Ni(OH)_2$	95.7 F/g at 5 mA/cm^2	1.7 V in KOH	37

Another capacitive device structure that has become interesting recently is the asymmetric supercapacitor.[38] Asymmetric supercapacitors consist of two

dissimilar types of electrodes: double layer electrode and one Faradic electrode. For example, a typical two-electrode asymmetric device construction includes a carbon-based electrode and a Faradic electrode material. The main feature of asymmetric supercapacitors is a wider cell voltage than symmetric supercapacitors hence getting higher energy in addition to utilization of both storage mechanisms of electrical double layer by porous materials and redox reactions by metal oxides/hydroxides.

An asymmetric supercapacitor of $Ni(OH)_2$/CNT//reduced graphene oxide (rGO), prepared by modified hummers method and CBD, has been reported with a specific capacitance of 78.33 F/g and a specific energy of 35.24 Wh/kg at 2 A/g.[34] Similar asymmetric supercapacitor of $Ni(OH)_2$/CNT//activated carbon (AC), prepared by chemical vapor deposition (CVD) and CBD, has been reported with a specific energy of 50.6 Wh/kg and a cyclic stability of 17% C_s loss after 3000 cycles.[35] It has been achieved a higher specific energy, 77.8 Wh/kg, for a $Ni(OH)_2$/rGO//porous graphene asymmetric supercapacitor, with a cell voltage of 1.6 V, specific capacitance of 218.4 F/g and 5.7% C_s loss after 3000 cycles.[39] Ni-Co-OH//rGO asymmetry supercapacitor, prepared by CBD and chemical reduction, has been reported with a cell voltage of 1.5 V and a specific power range from 0.32 kW/kg to 5 kW/kg.[36] $Co_3O_4/Ni(OH)_2$//rGO asymmetric supercapacitor, prepared by CBD, hydrothermal and chemical reduction, has been reported with a specific capacitance of 95.7 F/g at 5 mA/cm^2.[37] **Table 1.2** shows a summary of published reports on Ni-Co-OH//graphene asymmetric supercapacitors that their $Ni(OH)_2$ electrodes were prepared by CBD.

1.4. OBJECTIVES

The energy stored in a parallel-plat capacitor device is given by **Equation 1.5.** In order to increase the energy (E) stored in electrochemical supercapacitors, we can increase either the capacitance (C) or the operating voltage (V) of the device.

$$\mathbf{E} = \frac{\mathbf{1}}{\mathbf{2}}\ \mathbf{C}\ \mathbf{V^2} \qquad \textbf{Equation 1.5}$$

The capacitance can be increased by increasing the surface area (area of contact between the porous electrodes and liquid electrolyte). The surface area can be increased by developing 3-dimensional (3D) nanostructured electrodes that allow efficient electrolyte penetration and contact with active sites on the surface of the porous electrode. The operating voltage can be increased by adding carbon materials to transition metals electrodes, fabricating asymmetric supercapacitors, changing electrolyte, and connecting several supercapacitors in series.

In this work, $Ni(OH)_2$ nanomaterial has been selected for detailed studies due to its several attractive features. These features include significant electrochemical redox reactivity,[21] larger specific surface area than that for $Ni(OH)_2$ bulk-material, higher theoretical capacitance, natural abundance, environmental friendliness, and low cost. However, the main issue of $Ni(OH)_2$ electrode is the capacitance decay during long-term charge-discharge (CD) cycling. Therefore, the specific objectives of this research are to fabricate Ni-

based electrochemical supercapacitors with high capacitance, wide operating voltage window, good stability, and low cost. In addition, we will evaluate this material in conventional and microfabricated device structures and study their synthesis-structure-property relationships in $Ni(OH)_2$ electrodes and electrochemical devices.

1.4.1. Conventional Supercapacitors

Conventional conducting planar substrates such as stainless steel and carbon paper are usually used as current collectors in reported and commercial supercapacitors. In this work, we focus on preparing Ni-based electrodes by optimizing CBD conditions to achieve the desired nanostructure and surface area on 3-dimensional current collectors. In particular, we optimized the process to develop conformal coatings on of flexible carbon microfibers by controlling process conditions such as solution composition and deposition time.

The microfibers conformally-coated with $Ni(OH)_2$ make direct physical contacts with essentially every single nanosheet since the nanosheets nucleate directly out of the microfiber surface. In this way, nanosheets make direct electrical contact with conducting carbon microfibers, leading to more efficient electron transport. Using this strategy, we are able to develop uniform 3-dimensional nanostructured electrodes with larger surface area and higher capacitance than 2- dimensional planar $Ni(OH)_2$ electrodes.

In order to improve cycling stability, we studied doping the $Ni(OH)_2$ electrodes with various types of dopants including Cu, Co, graphene and carbon nanofibers. In order to increase the operation voltage and energy density, we focus on fabricating Ni-based asymmetric supercapacitors in which the positive electrode contains Ni-based nanomaterials and the negative electrodes contains graphene.

1.4.2. On-chip Supercapacitors

Supercapacitors can be designed and fabricated at micro-scale level and used as on-chip devices. In this work, we focus on employing a combination of top-down photolithographic process and bottom-up chemical bath deposition (CBD) to fabricate Ni-based on-chip supercapacitors, also known as μ-supercapacitors. In particular, we optimized the process to develop a uniform $Ni(OH)_2$ nanosheets over Pt/Ti/glass current collectors by inserting different additional thin layers, such as Ni and Au, between $Ni(OH)_2$ and Pt/Ti/glass.

In fact, the small separation distance (in micro-scale) between micro-interdigitated finger electrodes is the key parameter in the fast movement of the electrolyte ions, leading to high-rate redox activity. Using this strategy, we are able to develop Ni-based on-chip supercapacitors with higher redox rate activity than the conventional supercapacitors (that have a separation distance in milli-scale between the electrodes).

In addition, we fabricate flexible on-chip supercapacitors by depositing $Ni(OH)_2$/Ni/Pt/Ti on polyethylene naphthalate (PEN) plastic substrate instead of glass. In order to further increase the operation voltage and potential applications, we use series-connected capacitors for powering a light emitting diodes.

Chapter 2 . EXPERIMENTAL TECHNIAUES

2.1. MATERIALS SYNTHESIS TECHNIQUES

2.1.1. Chemical Bath Deposition

One of the simplest and cost-effective techniques for depositing nanomaterials on substrates is chemical bath deposition (CBD). It can be performed at very low temperatures in contrast with hydrothermal method.[40] Substrates used in CBD can be conductive or nonconductive materials in contrast with that used in electrodeposition.[40] In addition, CBD is considered as an inexpensive technique that is suitable for large-scale production.[40] The first study of using CBD for NiO preparation was done by Pramanik *et al.*[32] The chemical bath used in that study, an aqueous mixture of nickel sulfate, potassium persulfate and ammonia solution, were later used by others to prepare $Ni(OH)_2$ and NiO.[41]

(a) CBD on carbon substrate (b) CBD on metallic substrate

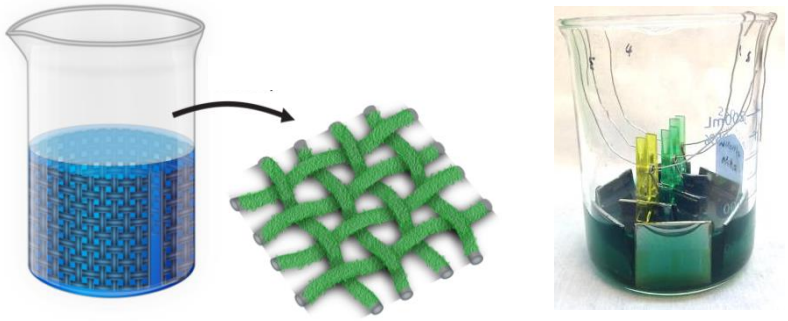

Figure 2.1 Sketch and photograph of chemical bath deposition (a) on carbon microfibers substrate. (b) on metallic substrate.

In the research of this dissertation, carbon microfibers substrates, metallic substrates and flexible substrates were immersed in chemical bath containing a clear-green mixture of 1 M of nickel(II) sulfate hexahydrate ($NiSO_4.6H_2O$), 0.15 M of potassium persulfate ($K_2S_2O_8$) in deionized (DI) water (H_2O) at room temperature. Ammonium hydroxide solution (30-33% NH_3 in H_2O) was then added to the mixture drop by drop with stirring for few seconds. As the reactions progressed, the mixture became dense, and the color turned into dark blue. The solution was then kept at room temperature. To optimize the synthetic conditions for the deposition of conformal $Ni(OH)_2$, the same procedure was repeated for different deposition times of 1h, 2h and 5h and at different ammonium hydroxide concentrations of 1.5 mL, 3 mL and 5 mL. The chemically coated substrates were afterwards taken out, washed by DI H_2O several times and dried at room temperature for 1h in air.

The fundamental chemistry of $Ni(OH)_2$ formation can be explained by a simple reaction involving the release of nickel cations and hydroxyl group anions from the precursors undergoing nucleation and precipitation of $Ni(OH)_2$ nanoparticles. This mechanism has been well-established in the literature [41, 42] and is can be represented by the simple reaction:

$$Ni^{2+} + 2OH^- \rightarrow Ni(OH)_2 \qquad \textbf{Equation 2.1}$$

2.1.2. Chemical Exfoliation

One of the simplest and cost-effective techniques for preparing graphene is the chemical exfoliation of graphite.[43] Chemical exfoliation is an

environmentally friendly method as it does not require strong acids in contrast with Hummer's method, or high temperature and high pressure in contrast with hydrothermal method. In addition, it can produce large quantity of high electrical conductive graphene since it is exfoliated directly from graphite without forming graphene oxide.[43] The fundamental principle of chemical exfoliation process depends on the intercalation of a chemical material such as 1-pyrenecarboxylic acid (PCA) into graphite sheets by sonication.[43] Using longer sonication time, the graphene nanosheets can be scrolled onto themselves forming carbon nanofibers or nanoscrolls.[44]

Graphene and carbon nanofibers (G-CNF) were prepared by chemical exfoliation in this research. A mixture of 100 mg of graphite and 16.5 mg of PCA in 50 mL of methanol were sonicated for 45 minutes (BRANSON Ultrasonic Cleaner 2510). Then, additional 200 mL of DI H_2O was added to the mixture with continuous sonication for several hours. G-CNF were collected by vacuum filtering using nanoporous membrane (Celgard 3501). The collected G-CNF were dissolved in ethanol and casted drop by drop on carbon microfibers substrate at 60^oC followed by washing with DI H_2O several times and drying in air overnight.

2.1.3. Photolithography

In order to fabricate micro-supercapacitors that can be integrated as on-chip energy storage in portable electronic devices, micro-electrodes should be designed. Photolithography is an optical printing technique that transfers a design pattern on a substrate.[45] The fundamental principle of photolithography

depends on the light exposure such as ultra-violet (UV) through a micro-fabricated mask, which is an transparent substrate with selective opaque areas, on a substrate coated by a photoresist layer, which is a photosensitive materials such as methoxy-propyl acetate (PGMEA).[45]

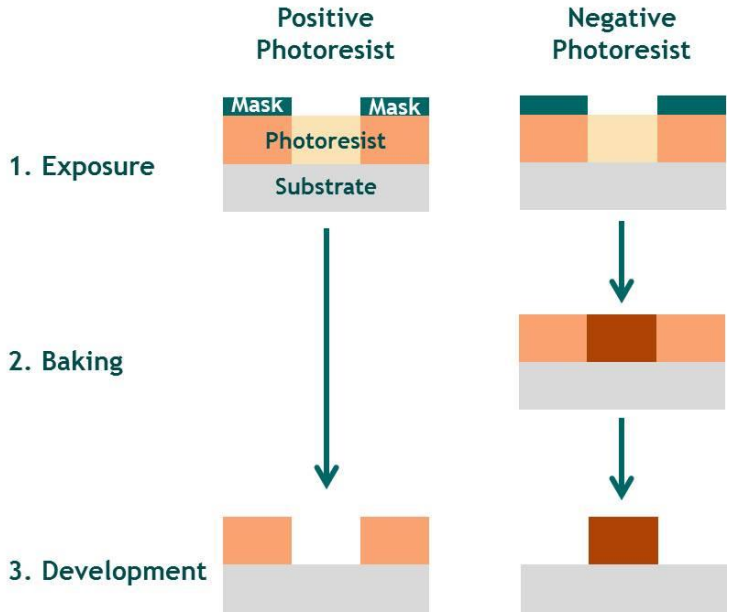

Figure 2.2 Sketch of positive and negative photolithography (re-sketched).[46]

When a positive photoresist is used, the exposed area of the photoresist is interacted and removed by a developer which is a chemical solution such as tetra-methyl-ammonium-hydroxide (TMAH). When a negative photoresist is used, the unexposed area of the photoresist is interacted and removed by a developer. In both positive and negative cases, a micro-pattern of photoresist is remained on the substrate as compared in Figure [45]

In our research, glass substrates (Fischer) were cut into 1x1" size, cleaned with a soap solution to remove the dirt, followed by ultrasonication in

acetone, isopropanol, and DI water sequentially for 5 minutes each, and then dried by blowing nitrogen. Plastic substrates based on polyethylene naphthalate (PEN) sheets were employed to fabricate flexible solid-state μ-supercapacitors. AZ9260 positive photoresist of PGMEA was spun coated at 3000 rpm for 60 seconds over the glass or PEN substrates to get 10 μm thick photoresist layers. Photoresist coated substrates were soft baked at 110 ºC for 3 minutes. The UV exposure was carried out using EVG contact aligner at a constant dose of 1800 mJ/cm^2 through the Cr/Glass mask having interdigitated micro-patterns. After exposure, samples were developed in AZ726 developer solution TMAH for 6 minutes which resulted in the formation of micor-patterns in the photoresist layer. Metal layers of 50 nm Ni/200 nm Pt/20 nm Ti were deposited by sputtering (Equiment Support Co., Cambridge, England) over the patterned photoresist layer. Before the lift-off process, the samples were immersed in the CBD bath containing precursor for the $Ni(OH)_2$ for 1-2 hrs. During the CBD process, $Ni(OH)_2$ nanoflakes were precipitated on the entire substrate uniformly. The lift-off was then performed in acetone to remove the unexposed photoresist layer along with the metal layers and $Ni(OH)_2$ deposits present on it. This process has resulted in the $Ni(OH)_2$ deposits over the interdigitated planar Ni/Pt/Ti electrodes. In this study, we have employed 30 interdigitated fingers (15 electrodes for each polarity) with a typical width of each finger 100 μm, and spacing between the fingers of 50 μm; the total area of all the fingers is 0.15 cm^2.

2.2. MATERIALS CHARECRIZATION TECHNIQUES

2.2.1. Scanning Electron Microscope

Scanning electron microscope (SEM) is considers as one of the most powerful techniques for characterizing the surface morphology of bulk and nanomaterials. The working principle of SEM is based on scanning a small-diameter electron probe with a focused primary electrons over the sample. Then, secondary electrons from each atom on the specimen are emitted, detected, amplified and forming an image of the scanned area.[47] In addition to the secondary electrons, X-ray is emitted from the sample when a higher-energy electron beam interacts with sample atoms. Such energy dispersive X-ray spectroscopy (EDXS) is characteristic for each element so that it is used to determine the elements present in the sample.

We have used Nova Nano SEM 630 (FEI Company) with Everhart-Thornley detector (ETD) as secondary electrode detector. A lower accelerating voltage of 5 kV was used in order to confined the beam interaction with the sample to regions very close the surface. Therefore, the images are much rich in surface details compared to those images that could be obtained at higher accelerating voltage (15-30 kV) where the beam penetrates in depth of the sample. In addition, a short working distance (WD) of around 5 mm was obtained in order to reduce the probe size and hence increase the resolution. In addition, the elemental spectra and mapping distribution in Ni-Cu-OH and Ni-Co-OH samples was confirmed by EDXS equipped with SEM using higher acceleration voltage of

10 kV as X-ray requires higher energy to be emitted from the sample atoms than the secondary electrons.

2.2.2. X-ray Diffraction

X-ray diffraction (XRD) is considered as one of the fundamental techniques to characterize the crystal structure. The physical fundamental of XRD is based on the path deference between the X-ray waves scattered by atoms from adjacent lattice planes (hkl) of spacing d_{hkl}.[48] The resultant intensity peaks on XRD pattern at each measured angle shows the condition of the constructive interference according to Bragg's law:

$$n\lambda = 2d_{hkl}\, sin\theta \qquad \textbf{Equation 2.2}$$

where *n* is an integer represents the order of diffraction, λ is the wavelength of the X-ray source, and θ is the angle between the incidence and diffraction to the lattice planes.[48]

For the crystal structure characterization of our samples, D8 Advance XRD System (Bruker Corporation) equipped with Cu Kα X-ray source (λ = 0.15406 nm) was used. The XRD measurement that was used is theta/2theta scan measurement where the X-ray source and detector are coupled to move simultaneously while the sample location is fixed. As each crystal structure and phase have characteristic XRD patterns, our resultant patterns were compared to database sheets in order to determine the crystal structure and the phases present in our samples.

2.2.3. Transmission Electron Microscope

In order to further characterize the crystal structure, high resolution transmission electron microscope (HRTEM) and selected area electron diffraction (SAED) were used. The main working principle depends on transmitting a high accelerated electrons beam through a thin sample. If the sample is crystalline, the electrons are diffracted by atomic planes inside the sample.[47] Arrangements of atoms and interplanar distance can be seen and measured by HRTEM images. SAED resultant patterns can be considered as analogue to the patterns of X-ray diffraction.[47]

We have used Titan Super Twin G2 60-300 TEM (FEI Company) with a high accelerating voltage of 300 kV. Such higher-energy electrons can penetrate distances of several microns into the sample in contrast with SEM.

2.2.4. Raman Spectroscopy

Raman spectroscopy technique is widely used in order to characterize the molecular structure of the materials. The physical principal of Raman spectroscopy is based on the inelastic scattering of the electromagnetic radiation of a source by the molecules of a sample.[49] Raman spectrum records the frequency changes between radiation and scattering frequency which is called Raman Shifts. Such frequency changes corresponds to the energy difference between the initial and final energy level of molecular vibration excited by the photon energy of the incident radiation.[49]

Raman spectroscopy (LabRAM ARAMIS, Horiba-Jobin Yvon) was used in this research and acquired with notch filters cutting at 100 cm^{-1} using a He-Ne laser (633 nm, 5 mW at source) and a laser spot size of 1.5 μm.

2.3. ELECTROCHEMICAL PERFORMANCE TECHNIQUES

2.3.1. Cyclic Voltammetry

Cyclic voltammetry (CV) is widely used to study the redox reaction reversibility and determine the voltage window of electrodes or devices. The principle of CV is to measure the resulting current simultaneously when applying a linear voltage to an electrode or a device between two preset voltage limits.[50]

In the research of this dissertation, CHI 660D and VMP3 multichannel electrochemical workstations (CH Instruments Incorporation and Bio-Logic) were used for CV experiments. CV experiments were carried out at different scan rates selected from 1 mV/s to 100 mV/s for conventional supercapacitors and from 10 mV/s to 500 V/s for on-ship micro-supercapacitors.

2.3.2. Galvanostatic Cycling (Chronopotentiometry)

Galvanostatic cycling (CD) is widely used to calculate the capacitance and cycling stability of electrodes or devices. The principle of CD is to measure the resulting voltage simultaneously when applying a constant current to an electrode or a device between two preset voltage limits.[50]

CHI 660D and VMP3 multichannel electrochemical workstations (CH Instruments Incorporation and Bio-Logic) were used for our CD experiments. CD experiments were carried out at different current densities selected from 1 A/g to 20 A/g for conventional supercapacitors and from 50 μA/cm^2 to 250 μA/cm^2 for on-ship micro-supercapacitors.

2.3.3. Electrochemical Impedance Spectroscopy

The equivalent series resistance, charge transfer resistance and diffusion impedance of electrochemical devices can be studied by electrochemical impedance spectroscopy (EIS). The main difference between EIS and CV that in EIS a sinusoidal voltage signal is imposed at a range of frequencies and the resulting current is measured, while a linear voltage is applied in CV.[50]

CHI 660D and VMP3 multichannel electrochemical workstations (CH Instruments Incorporation and Bio-Logic) were used for our EIS experiments. EIS experiments were performed in the frequency range from 100 kHz to 0.1 Hz at open circuit potential by applying a small sinusoidal voltage with an amplitude of few millivolts (5-10 mV). All electrochemical measurements were carried out at room temperature in 1 M of KOH aqueous electrolyte.

Chapter 3 . CONFORMALLY-COATED NICKEL HYDROXIDE NANOSTRUCTED ELECTRODES

Nuha A. Alhebshi, R. B. Rakhi and H. N. Alshareef, *Conformal coating of $Ni(OH)_2$ nanoflakes on carbon fibers by chemical bath deposition for efficient supercapacitor electrodes*. **Journal of Materials Chemistry A**, 1, 14897-14903, doi: 10.1039/C3TA12936E (2013)

ABSTRACT

A novel supercapacitor electrode structure has been developed in which a uniform and conformal coating of nanostructured $Ni(OH)_2$ flakes on carbon microfibers is deposited *in-situ* by a simple chemical bath deposition process at room temperature. The microfibers conformally-coated with $Ni(OH)_2$ nanoflakes exhibit five times higher specific capacitance compared to planar (non-conformal) $Ni(OH)_2$ nanoflakes electrodes prepared by drop casting of $Ni(OH)_2$ powder on the carbon microfibers (1416 F/g vs 275 F/g). This improvement in supercapacitor performance can be ascribed to the preservation of the three-dimensional structure of the current collector, which is a fibrous carbon fabric, even after the conformal coating of $Ni(OH)_2$ nanoflakes. The 3D network morphology of the fibrous carbon fabric leads to more efficient electrolyte penetration into the conformal electrode, allowing the ions to have greater access to active reaction sites. Cyclic stability testing of the conformal and planar $Ni(OH)_2$ nanoflakes electrodes, respectively, reveals 34% and 62% drop in

specific capacitance after 10000 cycles. The present study demonstrates the crucial effect that electrolyte penetration plays in determining the pseudocapacitive properties of the supercapacitor electrodes.

3.1. INTRODUCTION

In the face of increasing energy demand and the development of alternative sources to meet such demand, energy storage technologies are increasingly becoming a crucial component of many renewable energy systems. Supercapacitors, which fill the gap between batteries and conventional electrostatic capacitors in terms of power and energy densities, are considered as a very important element of energy storage applications.[51] They can be useful in many applications either as stand-alone (e.g., in regenerative braking systems) or in combination with batteries in hybrid electric vehicles.[3] To increase the energy density of supercapacitor we must increase either the capacitance or operating voltage of the devices. By increasing the specific surface area at the interface between electrodes and electrolyte, the capacitance can be increased. This goal can be realized by developing nanostructured electrodes that allow efficient electrolyte penetration and maintain low resistance. Several classes of materials have been reported in this respect, including carbon-based materials,[52] transition metal oxides/hydroxides,[53] and conductive polymers.[54]

It is desirable that simple and cost-effective materials and processes are used to fabricate the electrodes. For example, RuO_2 is one of the best

pseudocapacitive materials, but is expensive.[55] Nanostructured $Ni(OH)_2$ has been considered as a promising candidate as supercapacitor electrode due to its well-defined electrochemical redox reactions, large specific surface area, tunable morphology by modifying synthetic conditions, environmental friendliness, and comparatively low cost of its precursors. There are several studies indicating that high specific capacitance can be achieved using $Ni(OH)_2$ electrodes. Gong *et al.*[25] synthesized ß-$Ni(OH)_2$ nanosheets using solvothermal method and showed a specific capacitance of 1528 F/g at 1 A/g. Coin-like ß-$Ni(OH)_2$ nanoplates with a specific capacitance around 1300 F/g at 1 A/g were synthesized using coordination homogeneous precipitation method by Li *et al.*[26] ß-$Ni(OH)_2$ cross-linked nanowalls prepared by Lu *et al.*[27] using hydrothermal treatment at 100 ^oC exhibited a specific capacitance of 2675 F/g at 0.005 A/cm^2. Hydrothermal processing was also used to prepare different morphologies by changing the treatment temperature. For instance, a specific capacitance of 1398.5 F/g at 0.005 A/cm^2 for ß-$Ni(OH)_2$ hierarchical hollow microspheres prepared at 180 ^oC was reported by *Yang et al.*[28] The previous reports indicate that the cross-linked nanowalls morphology provides promising supercapacitor performance. However, one of the disadvantages of the hydrothermal method is that it is time consuming and has heightened sensitivity of oxide/hydroxide morphology to hydrothermal process conditions, which make it difficult to scale up to industrial scale. Chemical bath deposition, on the other hand, is a much simpler process and can be performed at very low temperatures. Therefore, it has the potential to be more cost

effective. Substrates used in CBD can be conductive or nonconductive materials in contrast with that used in electrodeposition. In addition, CBD is considered as an inexpensive technique that is suitable for large-scale production. The first study of using CBD for NiO preparation was done by Pramanik *et al.*[32] The chemical bath used in that study, an aqueous mixture of nickel sulfate, potassium persulfate and ammonia solution, were later used by others to prepare $Ni(OH)_2$ and NiO.[41]

Few papers have studied the utilization of CBD in preparing nanostructured $Ni(OH)_2$ for supercapacitor applications. Patil *et al.*[56] prepared honeycomb-like $Ni(OH)_2$ thin film via a CBD at 60 ^oC on stainless steel substrates. The resultant specific capacitance was 398 F/g at a scan rate of 5 mV/s. A specific capacitance of 296 F/g at 0.005 A/cm^2 was obtained for interconnected honeycomb-like $Ni(OH)_2$, and a specific capacitance of 468 F/g at 0.005 A/cm^2 was exhibited by interconnected $Ni(OH)_2$ nanoflakes prepared using CBD at 70 ^oC on stainless steel substrates by Dubal *et al.*[57] Further, α-$Ni(OH)_2$ interconnected nanoflakes was synthesized using CBD at room temperature on Ni foam and resulted in a high specific capacitance of 2200 F/g at 1 A/g by Hu *et al.*[24]. However, the electrode in that particular study suffers from a 40% relative specific capacitance drop after only 2000 cycles.[24] A recent paper showed that β-$Ni(OH)_2$/γ-NiOOH composite film with interconnected nanoflakes prepared by CBD at room temperature on Ni foam exhibited a specific capacitance of 1420 F/g at 1A/g. However, its cyclic stability test was measured only for 1000 cycles.[58] In addition, it is not clear what the

contribution of the Ni foam may have been to the overall capacitance of these devices in those studies.

In the present study, we demonstrate a novel and simple method for obtaining a conformal coating of $Ni(OH)_2$ nanoflakes on fibrous carbon fabric using CBD at room temperature. We show that the three dimensional structure of conformal $Ni(OH)_2$ electrode exhibits a higher specific capacitance by increasing electrolyte penetration, giving easy access to the active $Ni(OH)_2$ sites on the electrode. It also gives a significantly improved cycling performance compared with previous reports on CBD of $Ni(OH)_2$ electrodes.

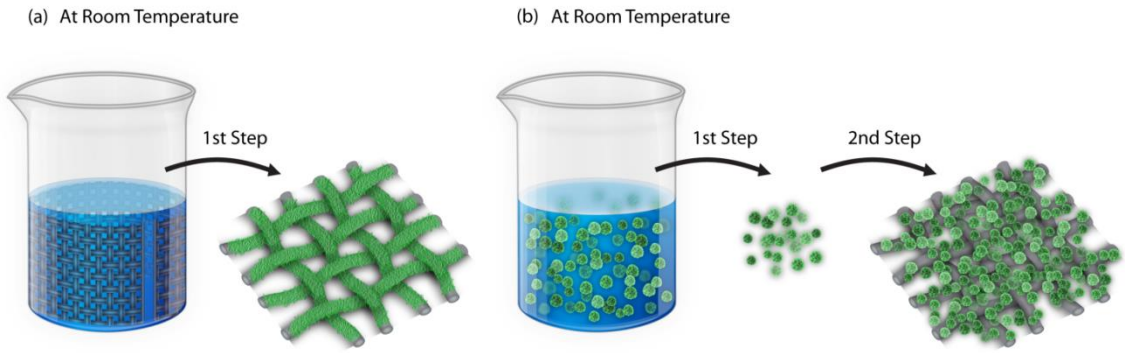

Figure 3.1 Schematic of the synthesis of $Ni(OH)_2$ interconnected nanoflakes by CBD and fabrication of (a) conformal $Ni(OH)_2$ electrode and (b) planar $Ni(OH)_2$ electrode.

3.2. EXPERIMENTAL METHODS

3.2.1. Synthesis of Conformal $Ni(OH)_2$ Nanoflakes

A piece of a commercial fibrous carbon fabric (carbon cloth 7302003, Fuel Cell Store) was used as a substrate, which has 99% carbon content and a

mass density of 11.5 mg/cm^2. This substrate was immersed in a chemical bath containing a clear-green mixture of 5.26 g of nickel(II) sulfate hexahydrate ($NiSO_4.6H_2O$), 1 g of potassium persulfate ($K_2S_2O_8$) and 45 mL of deionized (DI) water (H_2O) in a 150 mL Pyrex beaker at room temperature. 3 mL of ammonium hydroxide solution (30-33% NH_3 in H_2O) was then added to the mixture drop by drop with stirring for few seconds. As the reactions progressed, the mixture became dense, and the color turned into dark blue. The solution was then kept without stirring at room temperature for 1h. To optimize the synthetic conditions for the deposition of conformal $Ni(OH)_2$, the same procedure was repeated for longer deposition times of 2h and 5h and at different ammonium hydroxide concentrations of 3 mL and 5 mL. The chemically coated substrates were afterwards taken out, washed by DI H_2O several times and dried at 60 ^oC for 1h in air. Four samples of conformal $Ni(OH)_2$ were prepared on fibrous carbon fabric pieces of different areas of 1.94, 1.32, 2.00 and 1.75 cm^2 with magnitudes of mass loading of 2.07, 2.02, 1.11 and 0.44 mg/cm^2, respectively. The mass loading, for each sample, was calculated by means of weighing the carbon substrates before and after the deposition using a microbalance (XP26, METTLER TOLEDO).

3.2.2. Synthesis of Planar $Ni(OH)_2$ Nanoflakes

The same mixture of chemicals as in the above experiment, using 5mL of ammonium hydroxide and deposited for 2h, without the fibrous carbon fabric insertion into the reaction beaker was used for the synthesis of stand-alone

$Ni(OH)_2$ nanoflakes. The resultant dense-dark blue solution was filtrated to collect a pasty precipitated product, washed by DI H_2O several times and dried at 60 ^oC for 1h in air. The collected $Ni(OH)_2$ nanoflakes powder was then mixed with ethanol and casted drop by drop on the fibrous carbon fabric. The substrate coated by drop casting was afterwards taken out and dried at 60 ^oC for 1h in air. Two samples of planar $Ni(OH)_2$ were prepared on fibrous carbon fabric pieces of different areas of 1.58 and 1.50 cm^2 with magnitudes of mass loading of 1.76 and 1.06 g/cm^2. All the chemicals used in these experiments were analytical grade (SIGMA-ALDRICH) and without further purification.

3.2.3. Materials Characterization

The structure of the conformal and planar $Ni(OH)_2$ nanoflakes was analyzed using X-ray diffraction (XRD). A D8 Advance System from Bruker Corporation, equipped with Cu Kα X-ray source (λ = 0.15406 nm) was used. In addition, a selected area electron diffraction (SAED) pattern and high resolution transmission electron microscope (TEM) images (Titan Super Twin G2 60-300 TEM, FEI Company) with 300 kV were used to investigate both the structure and microstructure of the $Ni(OH)_2$ powder. Physical adsorption-desorption of Kr at the liquid-nitrogen temperature of -195.85°C using Accelerated Surface Area and Porosimetry (ASAP 2420 System, Micromeritics Company) with the Brunauer-Emmett-Teller (BET) method were used to measure the porosity and the specific surface area of the conformal $Ni(OH)_2$ nanoflakes. The surface structure and morphology of conformal and planar

$Ni(OH)_2$ nanoflakes were observed using scanning electron microscope (SEM) images (Nova Nano SEM 630, FEI Company) at different magnifications.

3.2.4. Electrochemical Measurements

The electrochemical properties of conformal and planar $Ni(OH)_2$ electrodes were investigated in standard three-electrode configuration using an electrochemical workstation (CHI 660D, CH Instruments Incorporation) by carrying out cyclic voltammetry (CV), galvanostatic (CD) and electrochemical impedance spectroscopy (EIS) measurements. Fibrous carbon fabric coated with $Ni(OH)_2$ nanoflakes were used as working electrodes in electrochemical cell containing 1 M KOH aqueous electrolyte solution. A saturated calomel electrode (SCE) and a Pt wire were used as a reference electrode and a counter-electrode, respectively. In addition, symmetric supercapacitor devices based on conformal $Ni(OH)_2$ on fibrous carbon fabric were fabricated. A coin cell of stainless steel (CR2032, MTI Corporation) containing 1 M KOH in standard two-electrode configuration was investigated using the electrochemical workstation.

CV experiments were carried out at different scan rates selected from 1 mV/s to 50mV/s. CD experiments were performed using current densities selected from 1 A/g to 10 A/g. EIS experiments were carried out at a direct current (DC) with 0V bias and a sinusoidal signal of 5 mV in a frequency range from 0.01 Hz to 100 kHz. EIS data was analyzed using a complex plane impedance plot (Nyquist plot).

3.3. RESULTS AND DISCUSSIONS

3.3.1. Materials Properties

Conformal $Ni(OH)_2$ nanoflakes were directly deposited on fibrous carbon fabrics by a simple CBD method sketched in **Figure 3.1 (a)**. The same chemical bath mixture, without the fibrous carbon fabric insertion into the reaction beaker, was used for the synthesis of stand-alone $Ni(OH)_2$ nanoflakes sketched in **Figure 3.1 (b)**. The chemistry of $Ni(OH)_2$ formation can be explained by a simple reaction involving the release of nickel cations and hydroxyl group anions from the precursors undergoing homogeneous nucleation and precipitation of $Ni(OH)_2$ nanoparticles. This mechanism has been well-established in the literature [41, 42] and it can be represented by the simple reaction:

$$Ni^{2+} + 2OH^{-} \rightarrow Ni(OH)_2 \qquad \textbf{Equation 3.1}$$

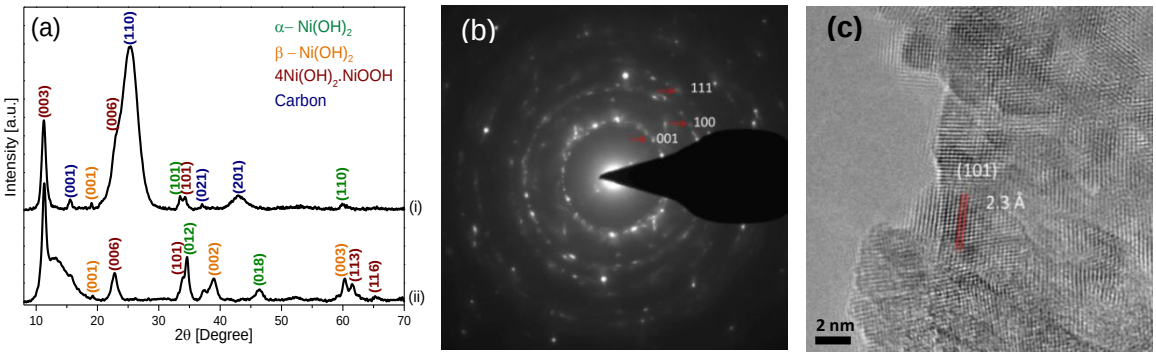

Figure 3.2 Structural characterization of $Ni(OH)_2$ nanoflakes by (a) XRD patterns of (i) conformal $Ni(OH)_2$ on fibrous carbon fabric and (ii) $Ni(OH)_2$ powder, (b) SAED pattern of $Ni(OH)_2$ powder, and (c) lattice resolved HRTEM image of $Ni(OH)_2$ powder.

The XRD pattern in **Figure 3.2 (a)** shows that both conformal and planar $Ni(OH)_2$ nanoflakes have mixed phases of α-$Ni(OH)_2$ (JCPDS 00-038-0715), ß-$Ni(OH)_2$ (JCPDS 00-014-0117) and $4Ni(OH)_2$-NiOOH (JCPDS 00-006-0044). The polycrystalline nature of the resultant nickel hydroxide has been predicted based on the fact that $Ni(OH)_2$-phase can be oxidized to NiOOH-phase using persulfate as indicated in the following molecular level heterogeneous reaction:[42]

$$2Ni(OH)_2 + S_2O_8^{2-} \rightarrow 2NiOOH + 2SO_4^{2-} + 2H^+ \qquad \textbf{Equation 3.2}$$

Figure 3.2 (b) shows SAED performed on $Ni(OH)_2$ powder. The pattern confirms the existence of ß-$Ni(OH)_2$ crystal structure in our sample. The lattice resolved HRTEM image shown in Figure 2c identifies the (101) atomic planes of a hexagonal crystal structure for the $Ni(OH)_2$ powder with an interplanar distance of 2.3Å.

Kr adsorption-desorption isotherm of conformal $Ni(OH)_2$ nanoflakes on fibrous carbon fabric, shown in **Figure 3.8 (a)** of Supporting Information, indicates that they are neither mesoporous nor microporous structures, which results in lowering the surface area of our sample. The specific surface area of conformal $Ni(OH)_2$ nanoflakes on fibrous carbon fabric was measured from the attached BET plot shown in **Figure 3.8 (b)** of Supporting Information. Since our fibrous carbon fabric consists of microfibers, instead of nanofibers or nanotubes, a small specific surface area is expected. The result revealed that our conformal $Ni(OH)_2$ nanoflakes on fibrous carbon fabric has a specific surface

area of 0.7 m^2/g which is smaller than the 0.8 m^2/g in which reported for $Ni(OH)_2$/carbon nanotubes core/shell nanostructures on Ni foam substrate.[35] It is well-known that carbon nanotubes/fibers have larger specific surface areas than that of carbon microfibers. Therefore, it can be concluded that the specific surface area of our $Ni(OH)_2$ and the reported one are comparable.

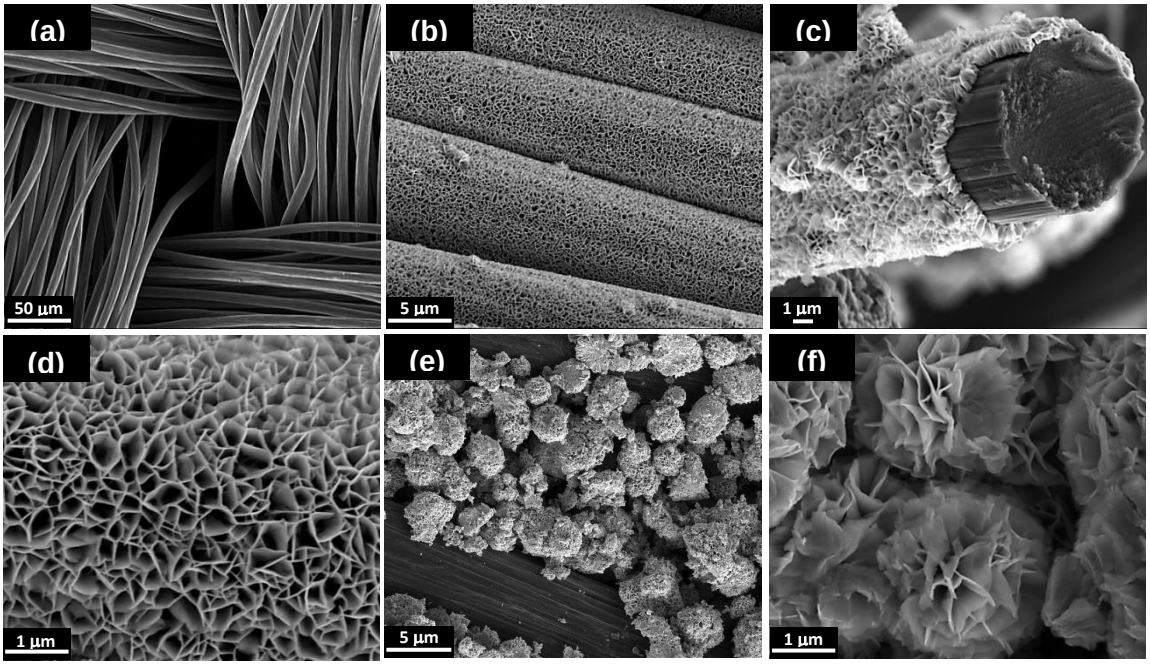

Figure 3.3 SEM images of (a) fibrous carbon fabric, (b), (c)and (d) conformal $Ni(OH)_2$ nanoflakes on fibrous carbon fabric at different magnifications, (e) and (f) planar $Ni(OH)_2$ nanoflakes on fibrous carbon fabric at different magnifications.

Figure 3.3 (a) shows an SEM image of the fibrous carbon fabric. It can be seen that this substrate has a 3D structure consisting of a network of microfibers. Such spun-yarn fabric structure provides additional flexibility to the substrate. **Figure 3.9** of Supporting Information shows SEM images of conformal $Ni(OH)_2$ nanoflakes prepared at different synthetic conditions . It can be noticed that carbon microfibers have no uniform coating of $Ni(OH)_2$

prepared using 3 mL of ammonium hydroxide and deposited for 1 h shown in **Figure 3.9 (a)** of Supporting Information. Similar observations can be seen in **Figure 3.9 (b)-(d)**. Our goal was to carefully optimize the CBD process to achieve a direct and conformal precipitation of $Ni(OH)_2$ nanoflakes on the microfibers in the carbon fabric substrate. **Figure 3.3 (b) and (c)** show that we have been successful in conformally coating $Ni(OH)_2$ nanoflakes on fibrous carbon fabric using 5 mL of ammonium hydroxide deposited for 2 h. Figure 3d shows a high magnification SEM image of the conformal $Ni(OH)_2$ coating on fibrous carbon fabric. It can be seen that the coating of $Ni(OH)_2$ are composed of interconnected nanoflakes. In addition, the conformal coating of $Ni(OH)_2$ nanoflakes on fibrous carbon fabric have also been achieved using a 3 mL of ammonium hydroxide deposited for 5 h shown in **Figure 3.9 (c)** of the Supporting Information. Based on the SEM comparisons of our samples, it is thought that the nucleation and growth of conformal $Ni(OH)_2$ on fibrous carbon fabric requires either high ammonium hydroxide concentration with short deposition time or low ammonium hydroxide concentration with long deposition time.

Figure 3.3 (e) shows the morphology of the planar $Ni(OH)_2$ electrode. As discussed earlier, this electrode was formed by first precipitating $Ni(OH)_2$ powder in the beaker using the CBD process. The powder was then coated by drop casting on the carbon fabric substrate. This method covers not only some of the microfibers, but also the spaces between them, and hence resulted in planar coating (as opposed to 3D coating as shown in **Figure 3.3 (b) and (c)**.

Figure 3.3 (f) shows that the planar coating of $Ni(OH)_2$ are composed also of interconnected nanoflakes.

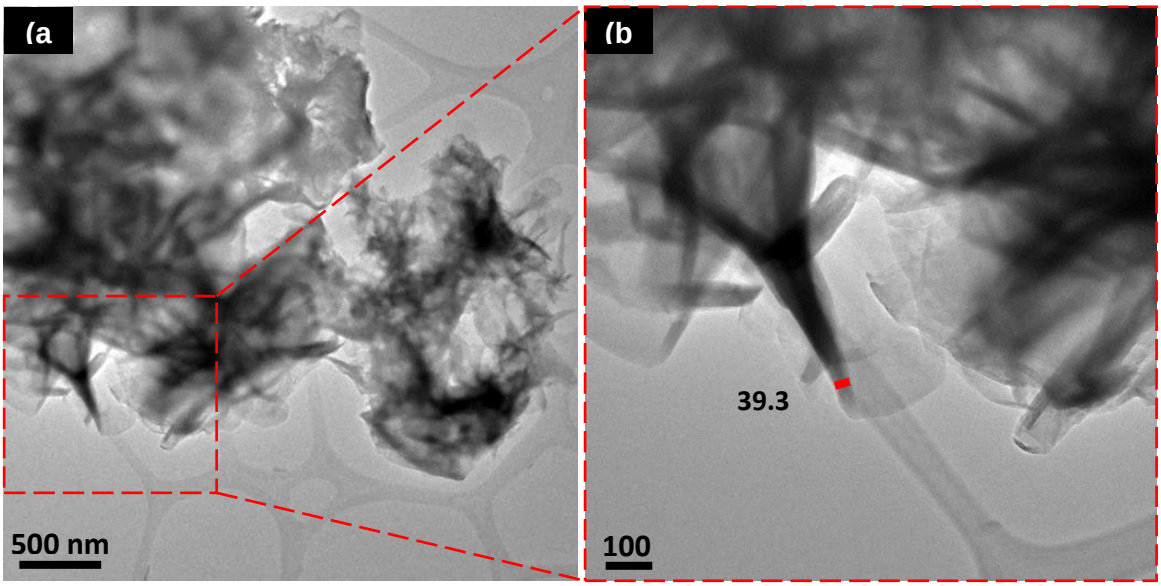

Figure 3.4 TEM images of (a) $Ni(OH)_2$ interconnected nanoflakes (b) a high resolution TEM image of (a).

Detailed structural analysis of these interconnected $Ni(OH)_2$ nanoflakes can be obtained from the analysis of TEM images. The structure in **Figure 3.4 (a)** has neither mesopores nor micropores, which is comparable with the result of the previous isotherm in **Figure 3.8 (a)**. Individual nanoflakes have an average thickness of nearly 39.3 nm as measured from the high resolution TEM image as shown in **Figure 3.4 (b)**.

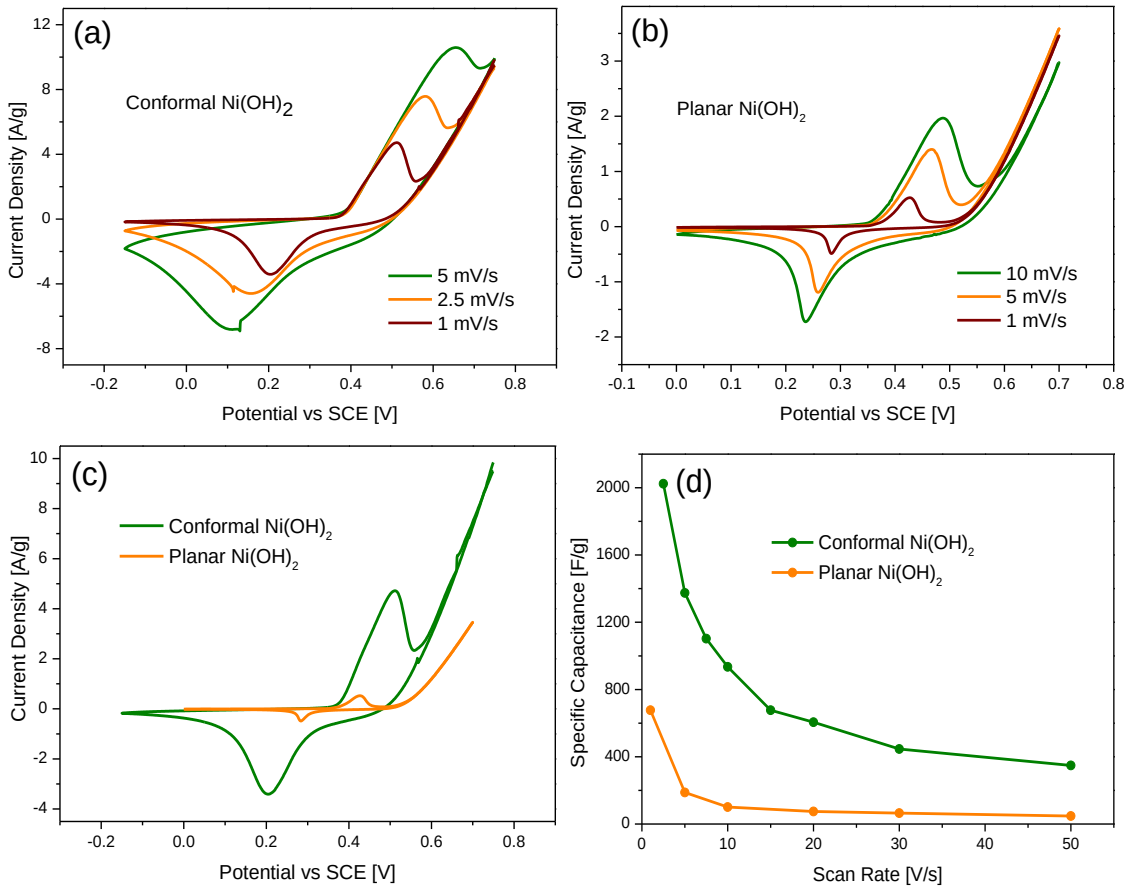

Figure 3.5 CV plots of (a) conformal $Ni(OH)_2$ electrode, (b) planar $Ni(OH)_2$ electrode, both at lower scan rates, and (c) comparison of CV loops of both samples measured at 1 mV/s (d) Specific capacitance as a function of scan rates for both electrodes.

3.3.2. Electrochemical Performance

CV curves of conformal and planar $Ni(OH)_2$ electrodes in 1 M KOH electrolytes were carried out by three-electrode electrochemical cell configuration (half-cell) and presented in **Figure 3.5 (a) and (b)**. Additional CV plots of both samples at higher scan rates are shown in **Figure 3.10 (a) and (b)** of Supporting Information. Both reduction (cathodic) and oxidation (anodic) current peaks are clearly visible. It is well-known that electrons can be stored and then released during the following redox reaction:

$NiOOH + e^- + H_2O \leftrightarrow Ni(OH)_2 + OH^-$ **Equation 3.3**

Therefore, the shapes of all CV curves in this study indicate that the charging-discharging mechanism of our electrodes is mainly based on reversible redox (or Faradic) reaction between Ni(II) and Ni(III). In addition, the absence of the rectangular shape of CV plots, which is the characteristic CV of an electrochemical double layer formed at the electrode/electrolyte interface, indicates that fibrous carbon fabrics has no obvious role in the charging-discharging mechanism of our electrodes. In order to confirm this observation, fibrous carbon fabric electrode was examined in 1 M KOH. The specific capacitance of fibrous carbon fabric electrode, calculated form discharge curves, was found to be less than 1 F/g although its CD curves (**Figure 3.13**) have the trigonal shapes, which are the ideal shapes of electrochemical double layer capacitors based on carbon materials. Therefore, the specific capacitance of our $Ni(OH)_2$ on fibrous carbon fabric electrode can be ascribed mainly to the redox reaction of $Ni(OH)_2$ and not to carbon microfibers.

In **Figure 3.5 (a) and (b)** and **Figure 3.10 (a) and (b)** of Supporting Information, there is a shift in oxidation and reduction potentials caused by changing scan rates. It is well-known that only outer active sites can sustain redox reactions completely at high scan rates. Therefore, specific capacitances at low scan rates can utilize both outer and inner active sites. **Figure 3.5 (c) and (d)** concludes that the specific capacitance of the conformal $Ni(OH)_2$ electrode is significantly higher than that of planar $Ni(OH)_2$ electrode.

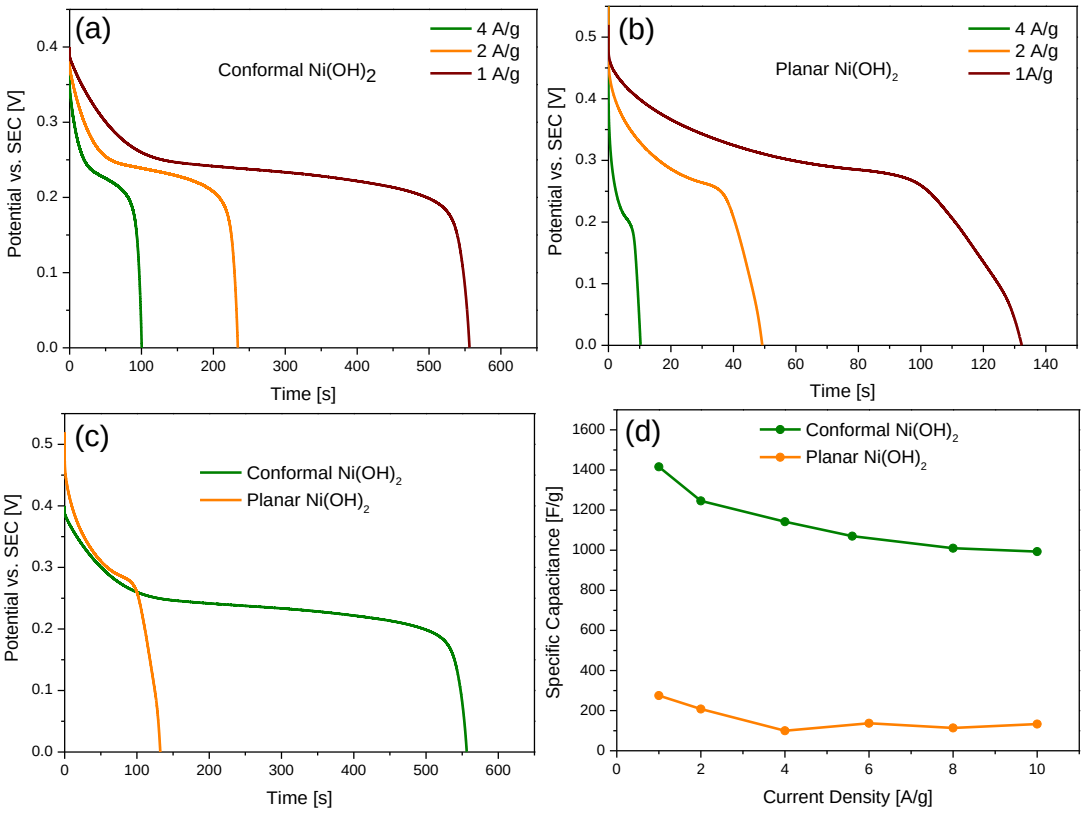

Figure 3.6 Discharge curves of (a) conformal $Ni(OH)_2$ electrode, (b) planar $Ni(OH)_2$ electrode, both at lower current densities, and (c) comparison of discharge curves of both samples measured at 1A/g. (d) Specific capacitance as a function of current densities.

Discharge curves of conformal and planar $Ni(OH)_2$ electrodes in 1 M KOH electrolytes are presented in **Figure 3.6 (a) and (b)**. Additional discharge curves of both samples at higher current densities are shown in **Figure 3.10 (c) and (d)** of Supporting Information. It can be seen that the discharge times for conformal $Ni(OH)_2$ electrode are longer than those for planar $Ni(OH)_2$ electrode. These discharge curves were used to calculate the specific capacitance at different current densities using **Equation** 2.5 of Supporting Information. As a result, the conformal $Ni(OH)_2$ electrode exhibited a specific capacitance of 1416 F/g at 1A/g which is five times higher than that of 275 F/g

at 1A/g for planar $Ni(OH)_2$ electrode, both of these values were derived from **Figure 3.6 (c)**. **Figure 3.6 (d)** shows that over a range of current densities, the conformal $Ni(OH)_2$ electrode shows significantly higher specific capacitance. It can be seen that at high current densities discharge times decrease to few seconds, and the potential drop caused by electrical resistance (IR drop) increases. CD experiments were also carried out on additional conformal $Ni(OH)_2$ electrodes at different mass loadings and current densities, as shown in **Figure 3.11** and **Figure 3.12** of Supporting Information. The magnitudes of mass loading of $Ni(OH)_2$ for the studied samples were 0.44 , 1.11 and 2.07 mg/cm^2. As expected, the magnitude of specific capacitance increases with decreasing mass loading.

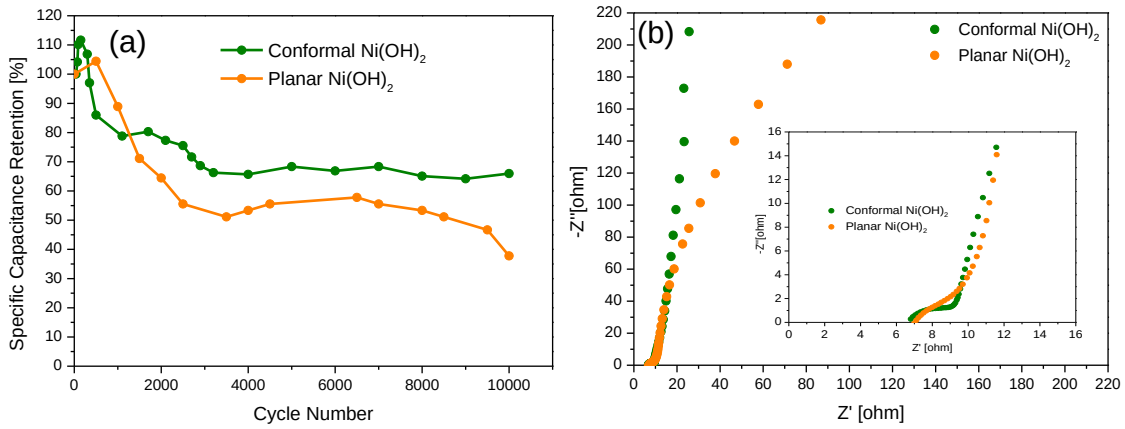

Figure 3.7 (a) Specific capacitance retention of conformal and planar $Ni(OH)_2$ electrodes for 10000 cycles at a current density of 20 A/g. (b) Nyquist plots of conformal and planar $Ni(OH)_2$ electrodes with an enlarged scale in the inset.

One important aspect of evaluating a supercapacitor performance for industrial applications is its cyclic stability. **Figure 3.7 (a)** shows the specific capacitance retention of conformal and planer $Ni(OH)_2$ electrodes after 10000

cycles at a current density of 20 A/g. The magnitudes of mass loading of conformal and planer $Ni(OH)_2$ were 2.02 and 1.06 mg/cm^2, respectively. The rise in specific capacitances during the first 150 cycles, as shown in **Figure 3.7 (a)**, can be explained by considering that pseudocapacitive materials are usually required to undergo several CD cycles to be fully activated and provide maximum Faradic capacitance. Comparing the values of the specific capacitance decrease after cycling observed in this work with those reported in the literature, an enhancement in cyclic stability performance has been achieved in our samples. Specifically, 22% specific capacitance drop is observed after 2000 for conformal $Ni(OH)_2$ electrode, as shown in **Figure 3.7 (a)**, compared to 37.6% specific capacitance drop after only 2000 cycles was reported for α-$Ni(OH)_2$ prepared using similar synthetic conditions.[24] Cyclic stability testing of the conformal and planar $Ni(OH)_2$ nanoflakes electrode respectively reveals 34% and 62% drops in specific capacitance after 10000 cycles, respectively.

Figure 3.7 (b) shows Nyquist plots obtained from EIS experiments for conformal and planar $Ni(OH)_2$ electrodes with an enlarged scale in the inset. The ideal shape of Nyquist plot consists of a semicircle in the high frequency region and a vertical straight line in the low frequency region. It is evident that the ideal shape is achieved in the case of conformal $Ni(OH)_2$ electrode while a small deviation is observed in the case of the planar electrode. It is well-accepted that the ionic diffusion of the electrolyte ions in electrodes can be indicated by the slope of the straight line in the low frequency region. It can be

noticed from **Figure 3.7 (b)** that the slope of the conformal $Ni(OH)_2$ electrode is larger hence it has a higher diffusion rate of electrolyte ions than that planar $Ni(OH)_2$ electrodes. This result can be attributed to the 3D nature of the structure of conformal $Ni(OH)_2$ electrode, which facilitates the accessibility of electrolyte ions to active materials. In addition, it can be calculated that both conformal and planar $Ni(OH)_2$ electrodes have a solution electrolyte resistance and charge-transfer resistance of ~6.9Ω and ~2Ω, respectively. The low charge-transfer resistances were achieved by the efficient attachment of $Ni(OH)_2$ nanoflakes on fibrous carbon fabric current collector, providing an ideal pathway for electron transport. Both the high diffusion rate of the electrolyte ions and the low charge-transfer resistance of conformal $Ni(OH)_2$ electrode explain its enhanced specific capacitances, as previously discussed.

Electrochemical performance of symmetric supercapacitor devices based on conformal $Ni(OH)_2$ on fibrous carbon fabric were evaluated by two-electrode electrochemical cell configuration (full-cell) as shown in **Figure 3.13** and **Figure 3.14** of Supporting Information. **Figure 3.14 (a)** shows CV curves at different scan rates of the full device showing well-behaved CV curves. The discharge curves at different current densities are shown in **Figure 3.14 (b) and (c)**. **Figure 3.14 (d)** and its inset show consistent specific capacitance values as obtained from CV and CD measurements using **Equation 3.6** and **Equation 3.7** of Supporting Information, respectively. Specifically, the specific capacitance as functions of current density gives a maximum specific capacitance of 368 F/g at 0.25 A/g (615 mF/cm^2). Nyquist

plots of this symmetric supercapacitor with an enlarged scale in the inset of **Figure 3.14 (e)** results in electrical resistance of 15 Ω and solution resistance of 1.22 Ω. Ragone plot, energy vs. power densities, was driven from discharged curves as shown in **Figure 3.14 (f)**. Our symmetric supercapacitor have a maximum energy density of 18.4 Wh/kg at 150 W/kg and a maximum power density of 980 W/kg at 0.3 Wh/kg, calculated using **Equation 3.8** and **Equation 3.9** of Supporting Information, respectively.

3.4. CONCLUSIONS

In this study, a conformal and uniform coating of interconnected $Ni(OH)_2$ nanoflakes was directly (in-situ) deposited on a fibrous carbon fabric substrate by CBD at room temperature. The conformal $Ni(OH)_2$ morphology, was compared to $Ni(OH)_2$ nanoflakes with planar morphology that are attached to fibrous carbon fabric using drop casting. In aqueous KOH electrolyte, conformal $Ni(OH)_2$ electrode exhibited a specific capacitance of 1416 F/g at 1 A/g which is five times higher than that of 275 F/g at 1 A/g for planar $Ni(OH)_2$ electrode. This sharp increase in specific capacitance in case of conformal $Ni(OH)_2$ can be attributed to more efficient electrolyte ion diffusion, as indicated from Nyquist plots. Moreover, cyclic stability studies of conformal and planer $Ni(OH)_2$ electrodes respectively reveals 34% and 62% drops in specific capacitance after 10000 cycles. The present study demonstrates the crucial effect of pseudocapacitive electrode morphology on electrolyte penetration and supercapacitor performance.

ACKNOWLEDGEMENTS

The authors acknowledge Dr. Dongkyu Cha, Research Scientist at KAUST Advanced Nano Imaging and Characterization Laboratory (ANIC), for his help in TEM characterization, and Dr. Omar El Tall, Research Specialist at KAUST Analytical Core Lab (ACL), for his help in physisorption experiments. Nuha A. Alhebshi acknowledges the support from the KAUST Graduate Fellowship. R. B. Rakhi acknowledges the support from SABIC Postdoctoral Fellowship.

SUPPORTING INFORMATION

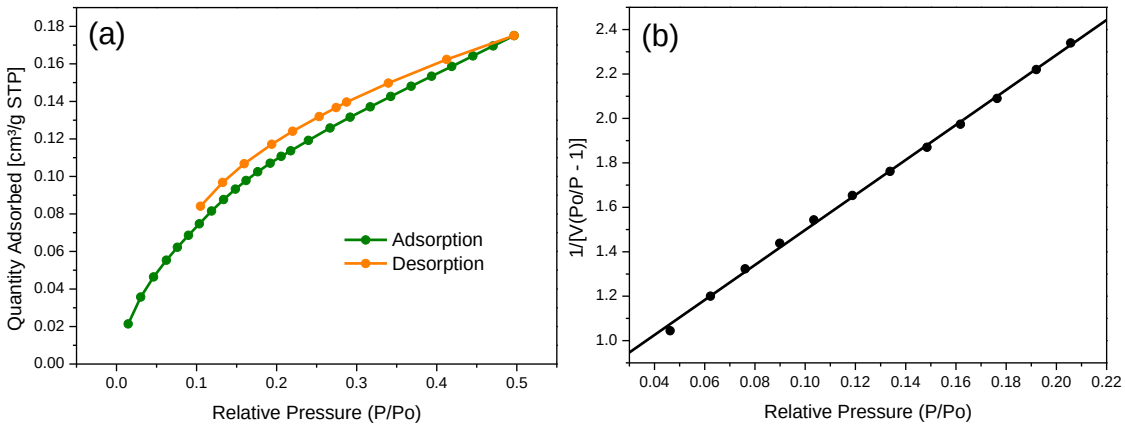

Figure 3.8 Krypton adsorption/desorption isotherm, (b) BET surface area plot of conformal $Ni(OH)_2$ nanoflakes on fibrous carbon fabric.

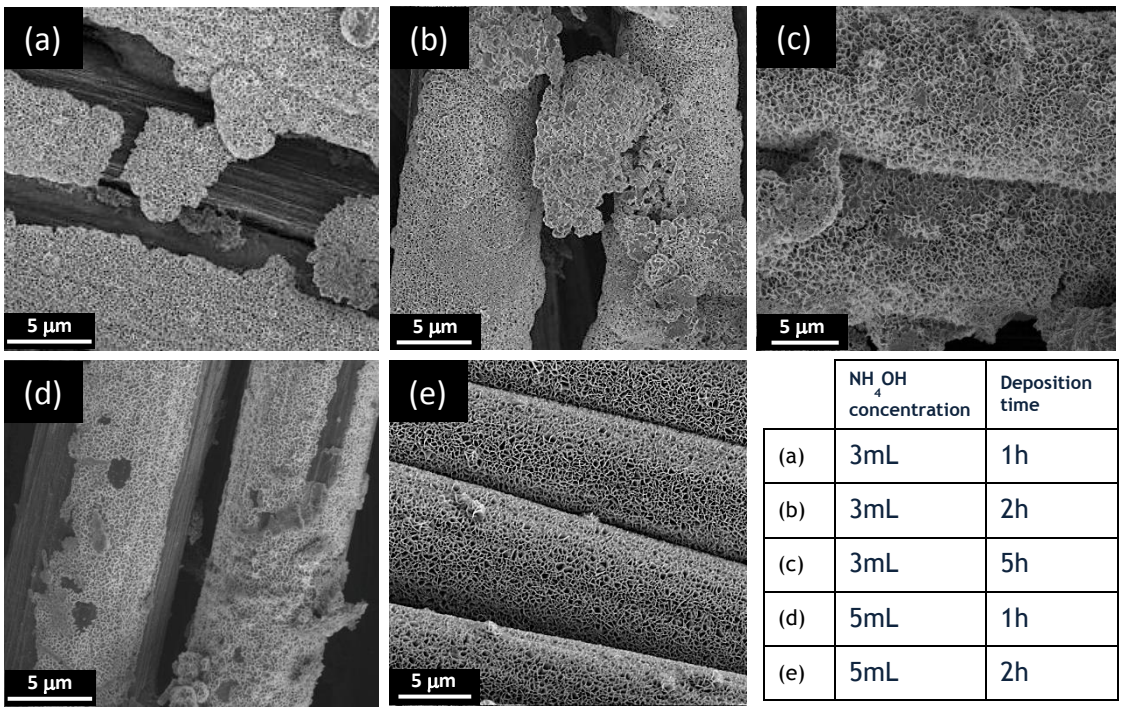

	NH_4OH concentration	Deposition time
(a)	3mL	1h
(b)	3mL	2h
(c)	3mL	5h
(d)	5mL	1h
(e)	5mL	2h

Figure 3.9 SEM images of $Ni(OH)_2$ nanoflakes on fibrous carbon fabric prepared at different synthetic conditions as indicated on the table.

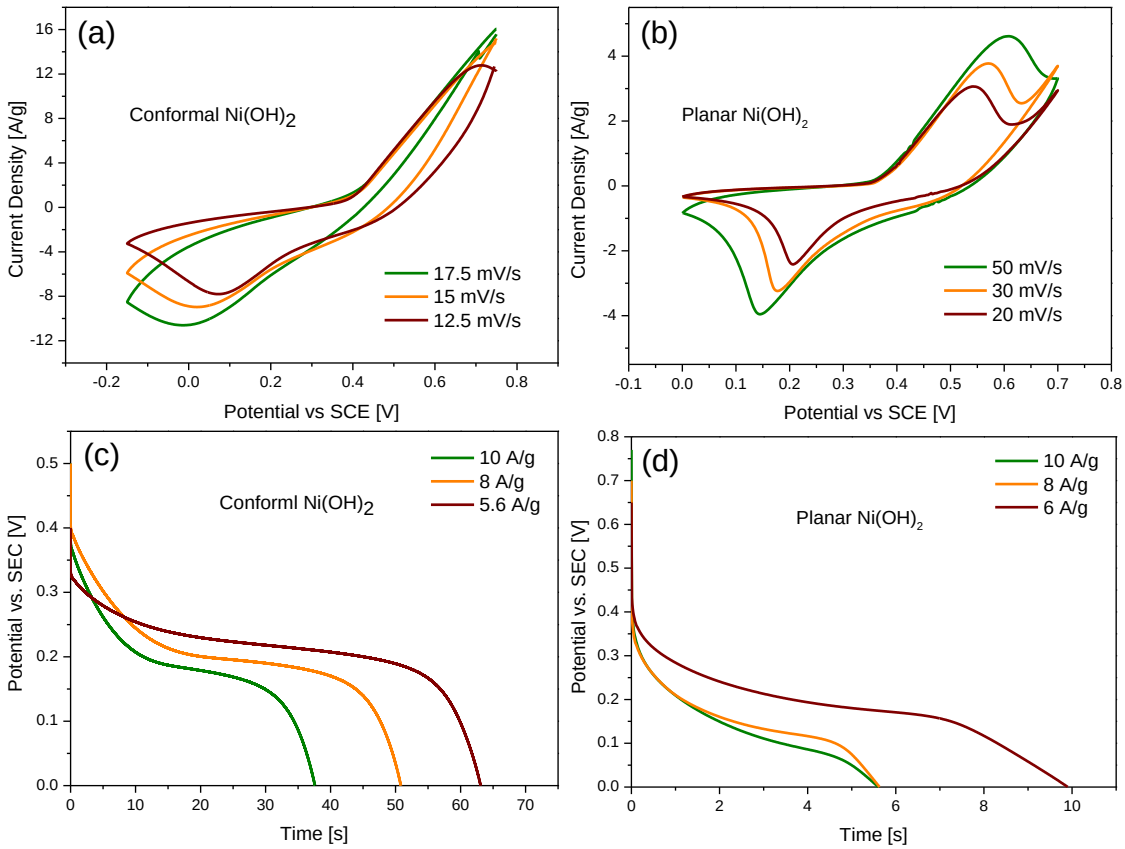

Figure 3.10 CV plots of (a) conformal $Ni(OH)_2$ electrode and (b) planar Ni(OH)2 electrode, both at higher scan rates. Discharge curves of (c) conformal $Ni(OH)_2$ electrode and (d) planar $Ni(OH)_2$ electrode, both at larger current densities.

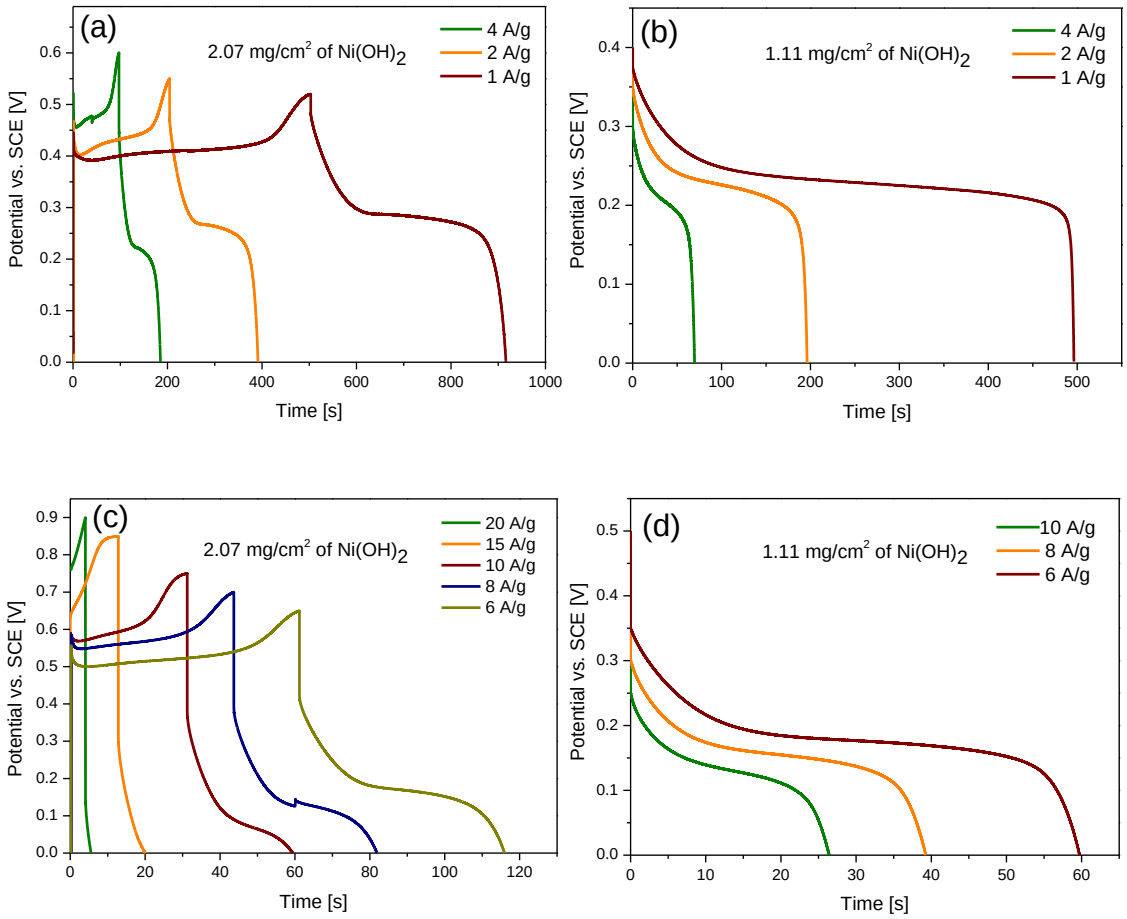

Figure 3.11 (a) and (c) CD plots of conformal $Ni(OH)_2$ electrode containing 2.07 mg/cm^2 of $Ni(OH)_2$ at different current densities. (b) and (d) Discharge plots of conformal $Ni(OH)_2$ electrode containing 1.11 mg/cm^2 of $Ni(OH)_2$ at different current densities.

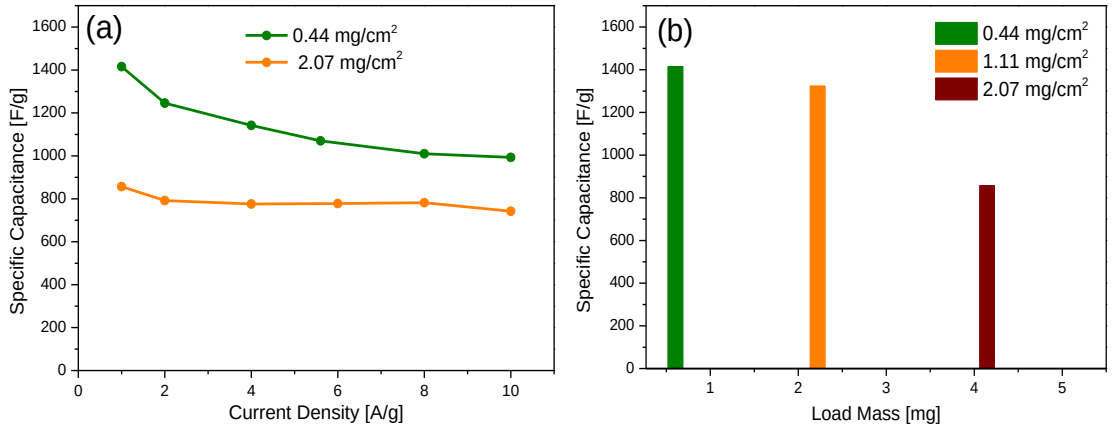

Figure 3.12 Specific capacitance (a) as a function of current densities for conformal $Ni(OH)_2$ electrodes with different mass loadings, and (b) as a function of mass loading for conformal $Ni(OH)_2$ electrodes.

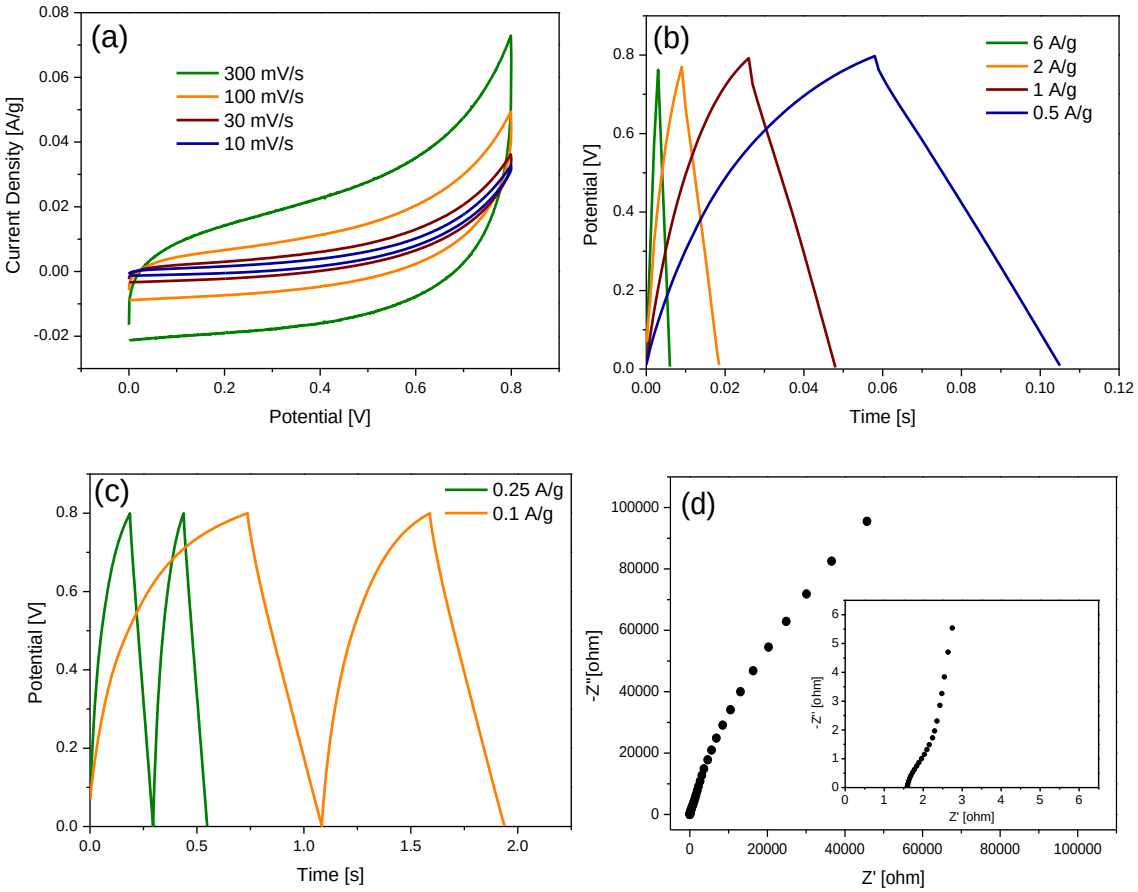

Figure 3.13 Two-electrode measurements of fibrous carbon fabric based symmetric supercapacitor (a) CV curves at different scan rates. (b) Discharge curves at higher current densities. (c) Discharge curves at lower current densities. (d) Nyquist plots with an enlarged scale in the inset.

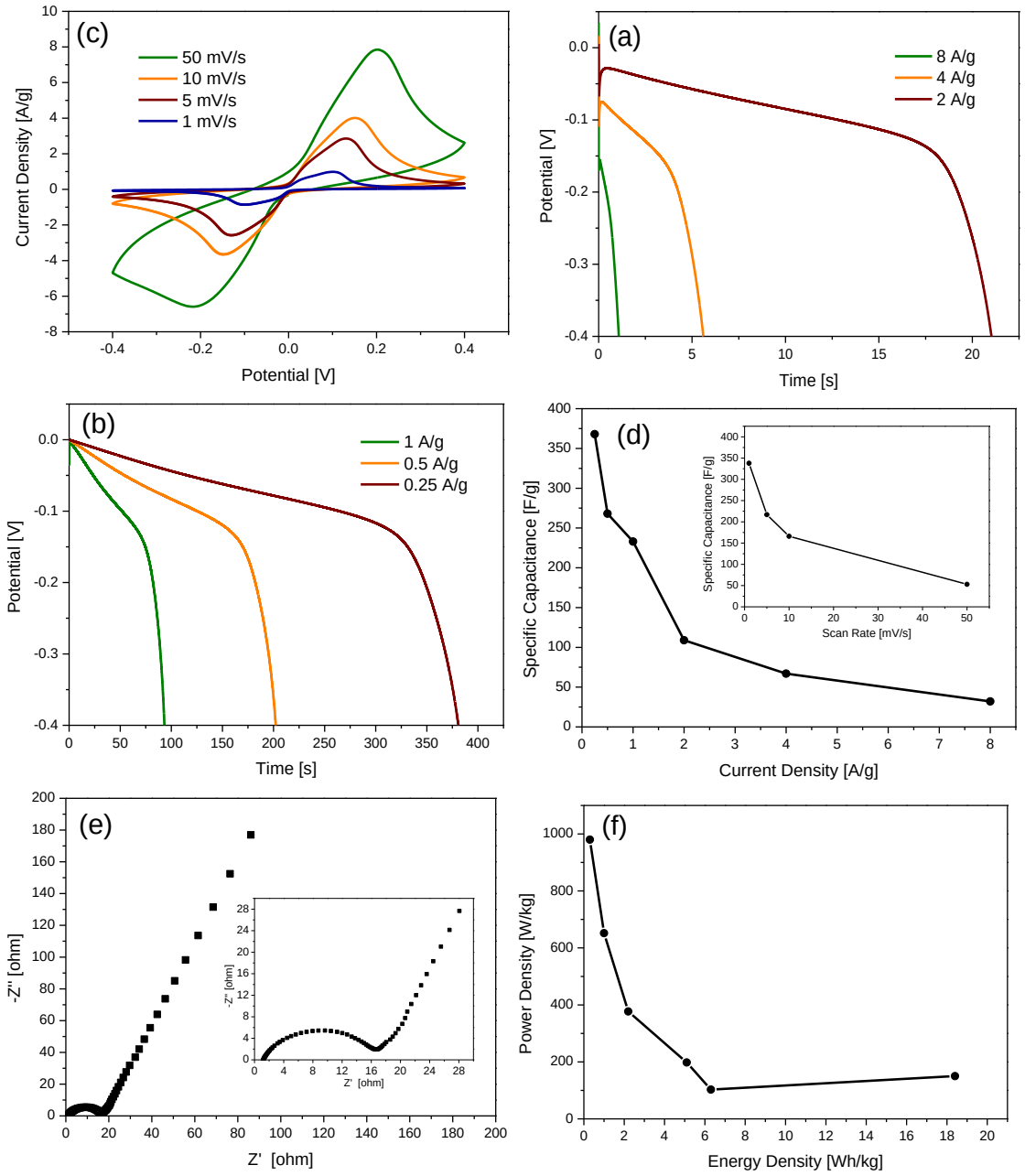

Figure 3.14 Two-electrode measurements of conformal $Ni(OH)_2$ based symmetric supercapacitor (a) CV curves at different scan rates. (b) Discharge curves at higher current densities. (c) Discharge curves at lower current densities. (d) Specific capacitance as a function of current densities (scan rate in the inset). (e) Nyquist plots with an enlarged scale in the inset. (f) Ragone plot. The mass loading per unit of area is 1.67 mg/cm^2 of $Ni(OH)_2$ on each electrode.

The specific capacitance (C_s) of an electrode in half-cell configuration (3-electrode measurements), as a function of scan rates, was calculated from CV curves by applying the equation:

$$\boldsymbol{C_s = \frac{\int i dv}{m\,\Delta V \frac{dv}{dt}}} \qquad \textbf{Equation 3.4}$$

where *i* is variable current [A], *m* is the mass of one electrode's active materials [g], ΔV is discharge voltage [V] and *dv*/*dt* is scan rate [V/s].

The specific capacitance of an electrode in half-cell configuration (3-electrode measurements), as a function of current densities, was calculated from discharge curves by applying the equation:

$$\boldsymbol{C_s = \frac{I\,\Delta t}{m\,\Delta V}} \qquad \textbf{Equation 3.5}$$

where *I* is constant current [A], Δt is discharge time [s], *m* is the mass of one electrode's active materials [g], and ΔV is discharge voltage [V].

It is noticed in the literature that specific capacitance values calculated from CV curves are usually higher than those values calculated from discharge curves. In this study, the results of both calculation methods indicated that conformal $Ni(OH)_2$ electrode exhibited specific capacitances significantly higher than that of planar $Ni(OH)_2$ electrode.

The specific capacitance of an electrode in full-cell configuration (2-electrode measurements), as a function of scan rates, was calculated from CV curves by applying the equation:

$$C_s = \frac{2\,Q}{m\,\Delta V} \qquad \text{Equation 3.6}$$

where Q is the charge of the discharge curve [C], m is the mass of one electrode's active materials [g], and ΔV is discharge voltage [V].

The specific capacitance of an electrode in full-cell configuration (2-electrode measurements), as a function of current densities, was calculated from discharge curves by applying the equation:

$$C_s = \frac{2\,I\,\Delta t}{m\,\Delta V} \qquad \text{Equation 3.7}$$

where all parameters as same as those of **Equation 2.4**

The energy (E) and power (P) densities of an electrode in full-cell configuration (2-electrode measurements), were calculated by applying the equations:

$$E = \frac{1}{2} C_s \Delta V^2 \qquad \text{Equation 3.8}$$

$$P = \frac{E}{\Delta t} \qquad \text{Equation 3.9}$$

where Cs is specific capacitance calculated from discharge curves, ΔV is discharge voltage [V] and Δt is discharge time [s].

Chapter 4 . NICKEL-COPPER AND NICKEL-COBALT HYDORXIDES BASED ELECTRODES

Nuha A. Alhebshi and H. N. Alshareef, *Ternary Ni-Cu-OH and Ni-Co-OH Electrodes for Electrochemical Energy Storage*, **Materials for Renewable and Sustainable Energy**, 4(4), 1-9, doi: 10.1007/s4024301500647 (2015)

ABSTRACT

In this project, Ni–Cu–OH and Ni–Co–OH ternary electrodes have been prepared. Different Ni:Cu and Ni:Co ratios were deposited by chemical bath deposition (CBD) at room temperature on carbon microfibers. Since $Ni(OH)_2$ is notorious for poor cycling stability, the goal of the work was to determine if doping with Cu or Co could improve $Ni(OH)_2$ cycling stability performance and conductivity against reaction with electrolyte. It is observed that the electrodes with Ni:Cu and Ni:Co composition ratio of 100:10 result in the optimum capacitance and cycling stability in both Ni–Cu–OH and Ni–Co–OH electrodes. This improvement in cycling stability can be attributed to the higher redox reversibility as indicated by the smaller CV redox peak separation. In addition, it is found that decreasing Cu and Co ratios, with fixed CBD time, enhances nanoflakes formation, and hence increases electrode capacitance. For the optimum composition (Ni:Co = 100:10), composites of the ternary electrodes with graphene and carbon nanofibers were also tested, with

resultant improvement in potential window, equivalent series resistance, areal capacitance and cycling stability.

4.1. INTRODUCTION

The demand for electrical energy storage devices, batteries and electrochemical supercapacitors is rapidly increasing in many crucial applications such as portable electronics, electric transportation, and renewable energy systems.[2] It is well-known that rechargeable batteries have higher energy but less power than those of electrochemical supercapacitors.[5] Electrochemical supercapacitors can be classified into electrical double layer capacitors (EDLC) and Faradic capacitors. In EDLC, charges are held at the interfacial double layer between a porous material and an electrolyte solution, while charges are stored in Faradic capacitors during Faradic oxidation-reduction (redox) reactions depending upon the electrode potential.[5] Due to the differences in these energy storage mechanisms, Faradic capacitors fundamentally exhibit higher capacitance but weaker charge–discharge cycling stability than those of ELDC. Porous materials with electrical conductivity have been earlier investigated for both fundamental understanding and practical implementations in EDLC.[6,7] For Faradic capacitors and rechargeable batteries, transition metal oxides/hydroxides and intrinsically conductive polymers have been intensively reported in the literature.[8-12]

Nickel hydroxide ($Ni(OH)_2$) nanomaterial is one of the most promising electrode materials for Faradic capacitors and rechargeable alkaline batteries,

due to significant electrochemical redox reactivity,[21] larger specific surface area than that of Ni(OH) bulk material, natural abundance, environmental friendliness, and low cost. However, the main issue of Ni(OH) electrodes is the capacitance decay during charge–discharge (CD) cycling. For instance, a high specific capacitance, 2222 F/g at 1 A/g, has been achieved using Ni(OH) electrode prepared by chemical bath deposition (CBD) on nickel foam at room temperature, but with a capacitance retention of 62% after only 2000 CD cycles at 1 A/g.[24] It has been reported in the same study that the major contributor to such capacitance decay is the phase transformation from α-Ni(OH) or γ-NiOOH to β-Ni(OH) or β-NiOOH phases, at relatively low discharge current densities.[24]

Such problem of low charge–discharge cycling stability has long been recognized for rechargeable Ni/Cd and Ni/MH alkaline batteries, and has been tackled by means of using metal additives such as Co, Ca, Zn and Al.[59-63] Co additive results in a good electrode material for electrochemical supercapacitors because its oxides and hydroxides exhibit high capacitance, while Cu offers excellent electrical conductivity. Recently, metal additives, binary and ternary oxides/hydroxides have been used in Ni-based electrochemical supercapacitors to enhance the cycling stability, electrical conductivity and capacitance. Even though enhanced performances of Ni-based electrochemical supercapacitors have been reported in the literature, many of the synthetic processes used in electrode materials preparation are energy consuming, environmentally unfriendly, and costly. For instance, a cell capacitance retention of 94.5% after 4000 CD cycles at 5 A/g and a cell

capacitance retention of 86% after 47,000 CD cycles at 25 A/g have been reported for (Ni–Co–Cu)$(OH)_2$-CuO//AC asymmetric supercapacitor. However, its cell capacitance of ~58 F/g at 5 A/g and ~54 F/g at 25 A/g was relatively low, and it was prepared by cathodic deposition which requires external energy source.[64]

In contrast to electrodeposition and hydrothermal synthesis methods, chemical bath deposition (CBD) is a highly recommended synthesis method for industrial and commercial implementations because it is simple, scalable, fast, cost effective, does not require external energy source, and can be done at room temperature. $Ni(OH)_2$ and NiO thin films were prepared by CBD for the first time by Pramanik and Bhattacharya.[32] Since then, $Ni(OH)_2$ nanomaterials prepared by CBD have been investigated and utilized as electrodes for electrochemical supercapacitors. For example, a specific capacitance of 1416 F/g at 1 A/g has been reported for conformal coating of $Ni(OH)_2$ nanoflakes electrode, prepared by CBD at room temperature on carbon microfibers, with a capacitance retention of 66% after 10,000 CD cycles at 20 A/g.[65] In addition, Ni-based electrodes with metal additives, binary, and ternary hydroxides have been prepared by CBD and used in electrochemical supercapacitors. A specific capacitance of 1030 F/g at 3 A/g has been reported for Ni–Co binary hydroxides electrode, prepared by CBD at 80 °C on nickel foam, but its cycling stability was studied for only 1000 CD cycles at 15 A/g.[36] Specific capacitances of 1970 F/g at 5 mV/s and 859 F/g at 6 A/g have been reported for Ni–Cu spherical double hydroxide electrode, prepared by CBD at room temperature on Nickel

foam, but with a capacitance retention of 69% after only 1600 CD cycles at 6 A/g.[66]

Reduced graphene oxide (rGO) nanosheets have been also utilized for electrochemical supercapacitors with much better cycling stability than that of metal oxide and hydroxide electrodes.[3] One of the best results for reduced graphene oxide supercapacitors was reported by Bai *et al*.[67] using a modified Hummer's method and hydrothermal reduction, and obtaining a full-cell specific capacitance of 230 F/g at 1 A/g and a capacitance retention of ~89% after 10,000 cycles. However, there are other simpler methods which can be used to prepare reduced graphene oxide, and it is useful to study their performance. One such simple method is the chemical exfoliation of graphite.[43] Chemical exfoliation is an environmentally friendly and cost-effective method as it does not require strong acids (as in Hummer's method), or high temperature and high pressure (as in the hydrothermal method). In addition, it can produce large quantity of electrically conductive graphene since it is exfoliated directly from graphite without forming graphene oxide. An *et al*.[43] have reported a full-cell specific capacitance of 120 F/g at 2 mA for chemically exfoliated graphene-based supercapacitors.

In this project, Ni–Cu–OH and Ni–Co–OH electrodes have been prepared using different Ni:Cu and Ni:Co ratios by CBD at room temperature on carbon microfibers. Effects of changing Ni:Cu and Ni:Co ratios on electrode morphology and electrochemical performance are investigated. For the

optimum composition (Ni:Co = 100:10), composites of the ternary electrodes with graphene and carbon nanofibers were also tested, with resultant improvement in potential window, equivalent series resistance, areal capacitance and cycling stability.

4.2. EXPERIMENTS

4.2.1. Synthesis of Ni-Cu-OH, Ni-Co-OH and G-CNF

Ni–Cu–OH electrodes were prepared by CBD with Ni:Cu ratios of 100:3, 100:10 and 100:25. The chemical bath consisted of 1 M of nickel(II) sulfate hexahydrate ($NiSO_4.6H_2O$), different molarities (0.03, 0.10 and 0.25 M) of copper(II) sulfate pentahydrate ($CuSO_4.5H_2O$) and deionized (DI) water (H_2O) in Pyrex beakers at room temperature. Then, 1.56 mL of ammonium hydroxide solution (30–33% NH_3 in H_2O) and 0.15 M of potassium persulfate ($K_2S_2O_8$) were added subsequently to the mixture. Several pieces of commercial carbon microfibers substrates from Fuel Cell Store (carbon cloth 7302003, 99% carbon content and 11.5 mg/cm^2) were immersed in the chemical bath by clamps at room temperature. The immersed parts of all carbon substrates have the same area of 1.00 cm^2. After 1 h, the coated substrates were taken out, washed several times with DI H_2O and dried in air at room temperature overnight. Ni–Co–OH electrodes with Ni:Co ratios of 100:3, 100:10 and 100:25 were prepared by the same previous procedures but with cobalt(II) chloride hexahydrate ($CoCl_2.6H_2O$) of different molarities (0.03, 0.10 and 0.25 M). All the chemicals

used in this project are of analytical grade (SIGMAALDRICH) and were used without further purification.

Graphene and carbon nanofibers (G-CNF) were prepared using a modified chemical exfoliation process.[43] A mixture of 100 mg of graphite and 16.5 mg of 1-pyrenecarboxylic acid (PCA) in 50 mL of methanol were sonicated for 45 min (BRANSON Ultrasonic Cleaner 2510). Then, 200 mL of DI H_2O was added to the mixture with continuous sonication for several hours. G-CNF were collected by vacuum filtration using nanoporous membranes (Celgard 3501). The collected G-CNF were dissolved in ethanol and casted drop by drop on carbon microfibers substrate at 60 °C followed by washing with DI H_2O several times and drying in air overnight. Finally, G-CNF on carbon microfibers were used as substrates in CBD of the same previous procedure of Ni–Co–OH with Ni:Co ratio of 100:10 and deposition time of 1 h – 2 h to prepare Ni–Co–OH/G-CNF electrodes.

4.2.2. Materials Characterization

The mass loading of each electrode was calculated by weighing the carbon substrate before and after the CBD using a sensitive microbalance from METTLER TOLEDO (XP26, 0.001 mg resolution). The morphology of Ni–Cu–OH, Ni–Co–OH and Ni–Co–OH/G-CNF electrodes were observed by scanning electron microscopy (SEM) at different magnifications. The elemental spectra and mapping distribution in Ni–Cu–OH and Ni–Co–OH electrodes are confirmed by energy dispersive X-ray spectroscopy (EDX). SEM was equipped with EDX from

FEI Company (Nova Nano SEM 630). G-CNF was characterized using X-ray diffraction (XRD) from Bruker Corporation (A D8 Advance System) and Raman spectroscopy from HORIBA Scientific.

4.2.3. Electrochemical Measurements

Ni–Cu–OH, Ni–Co–OH and Ni–Co–OH/G-CNF were used as working electrodes. Saturated calomel electrode (SCE) and a platinum (Pt) wire were used as reference electrode and counter electrode, respectively. The aqueous electrolyte solution was 1 M of potassium hydroxide (KOH). Electrochemical redox reactions were studied by cyclic voltammetry (CV). Electrode capacitances and cycling stability were calculated by chronopotentiometric (galvanostatic) charge–discharge (CD). Equivalent series resistances, charge transfer resistances and diffusion control were studied by electrochemical impedance spectroscopy (EIS). All experiments were carried out in standard three electrode configuration using a multichannel Potentiostat/Galvanostat/ EIS from BioLogic Science Instruments (VMP3).

4.3. RESULTS AND DISCUSSION

4.3.1. Materials Properties

EDX elemental mapping images for Ni–Cu–OH electrode and Ni–Co–OH electrode with Ni:Cu and Ni:Co ratios of 100:10 are shown in **Figure 4.1 (a) and (b)**, respectively. **Figure 4.1 (a)** confirms the presence of carbon, nickel, copper and oxygen in Ni–Cu–OH electrode. In addition, it can be seen that

nickel, copper and oxygen are homogenously distributed around carbon microfibers. **Figure 4.1 (b)** confirms the presence of carbon, nickel, cobalt and oxygen on Ni-Co-OH electrode with homogenous distribution around carbon microfibers. EDX spectra of all Ni-Cu-OH and Ni-Co-OH electrodes of composition 100:3, 100:10 and 100:25 are shown in **Figure 4.7** (of the Supplementary Information).

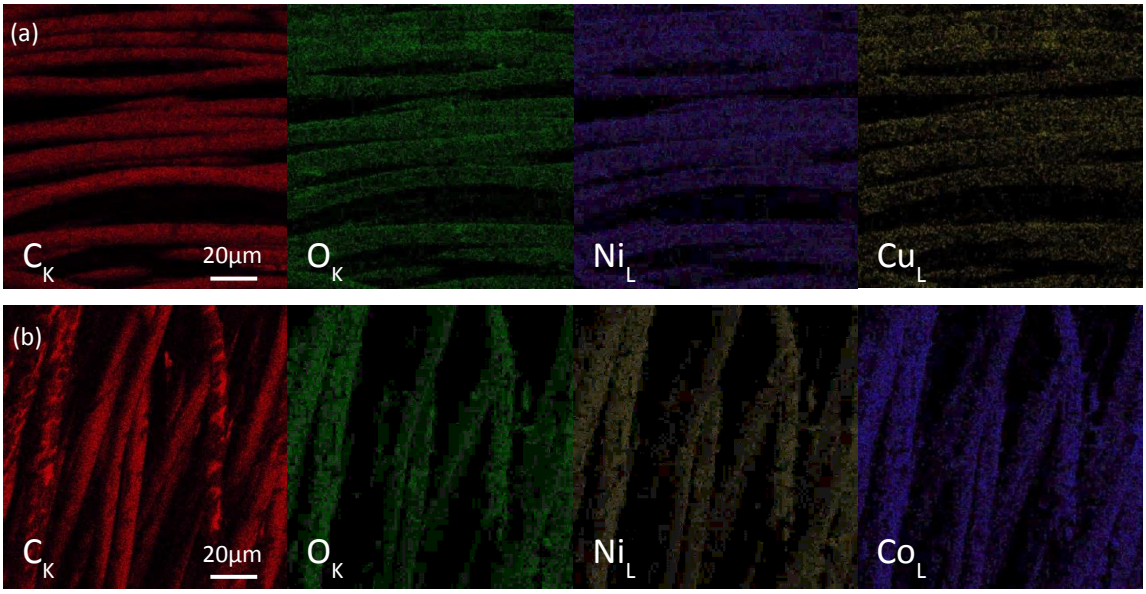

Figure 4.1 (a) and (b) EDX elemental mapping images for Ni-Cu-OH and Ni-Co-OH electrodes, respectively.

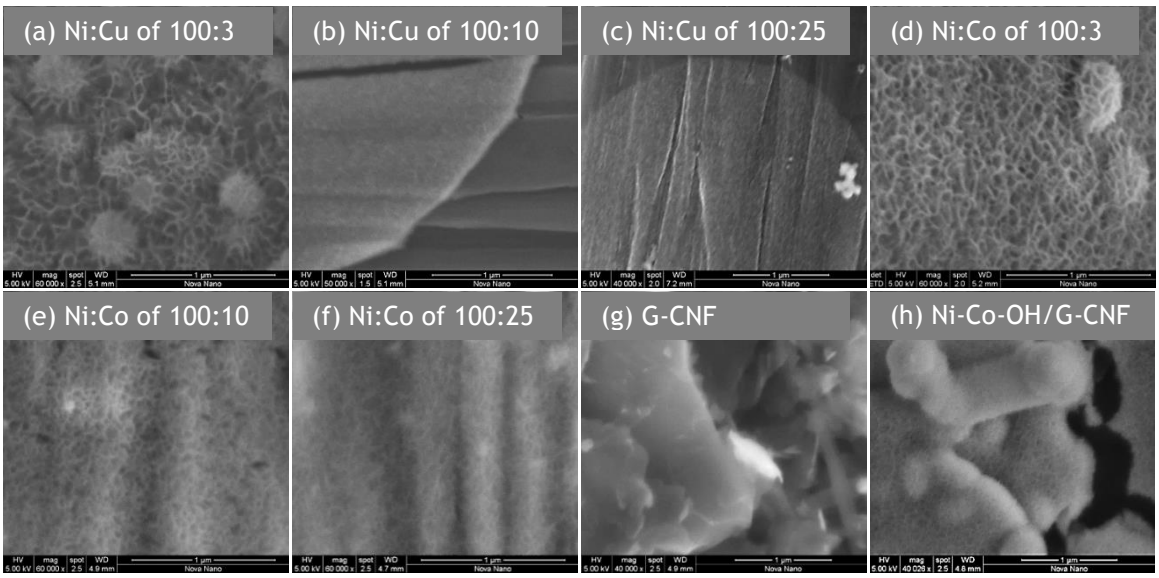

Figure 4.2 SEM images of (a)-(c) Ni-Cu-OH electrodes of 100:3, 100:10 and 100:25, respectively. (d)-(f) Ni-Co-OH electrodes of 100:3, 100:10 and 100:25, respectively. (g) G-CNF electrode. (h) Ni-Co-OH/G-CNF electrode. All electrodes are coated on carbon microfibers substrates.

SEM images in **Figure 4.2 (a)-(c)** show the morphology changes for Ni-Cu-OH electrodes of 100:3, 100:10 and 100:25, respectively. Nanoflakes are clearly shown at Ni:Cu ratio of 100:3 in **Figure 4.2 (a)**, while increasing the Cu content to 100:10 and 100:25 leads to suppression of nanoflake formation and to growth of flat morphology, as shown in **Figure 4.2 (b) and (c)**. SEM images Ni-Co-OH electrode of 100:3, 100:10 and 100:25 in **Figure 4.2 (d)-(f)**, respectively, show nanoflakes morphology at different stages of growth. It seems that nanoflakes in **Figure 4.2 (f)** have grown incompletely. It can be concluded that increasing Co ratio to 100:10 and 100:25 slows nanoflake formation and growth, even though the CBD time was fixed for all studied electrode compositions. Nanoflake morphology is considered as one of the most preferred morphologies for electrochemical supercapacitors due to the large possible interface

between nanoflake surface and electrolyte. Therefore, it is expected that the nanoflake morphology, such as in **Figure 4.2 (a), (d) and (e)**, leads to higher capacitance than the flat morphology, such as in **Figure 4.2 (b), (c) and (f)**. Small magnification SEM images of all Ni–Cu–OH and Ni–Co–OH electrodes of 100:3, 100:10 and 100:25 are shown in **Figure 4.8 (a)-(f)** in the Supplementary Information which shows that the carbon microfibers substrates have been conformally coated. Graphene and carbon nanofibers (G-CNF) can be seen clearly in **Figure 4.2 (g)**. The diameter of an individual CNF is around 200 nm as shown in **Figure 4.8 (g)** of the Supporting Information. **Figure 4.8 (h)** shows Ni–Co–OH coated on G-CNF using Ni:Co ratio of 100:10 and a deposition time of 1 h. Using the same ratio but with a deposition time of 2 h leads to increased nanoflake growth as shown in **Figure 4.8 (h)**.

XRD pattern of G-CNF is compared with that of graphite in **Figure 4.9 (a)** in the Supplementary Information. It can be seen that (002) peak of G-CNF at 26.5° is broader than that of graphite indicating that the interplanar distance between graphene nanosheets is increased and the particles size is decreased. D band and G band of Raman spectrum are shown in **Figure 4.9 (b)** confirming graphene formation in our G-CNF sample. **Figure 4.9 (c)** shows a photograph of G-CNF dissolved homogenously in water and methanol.

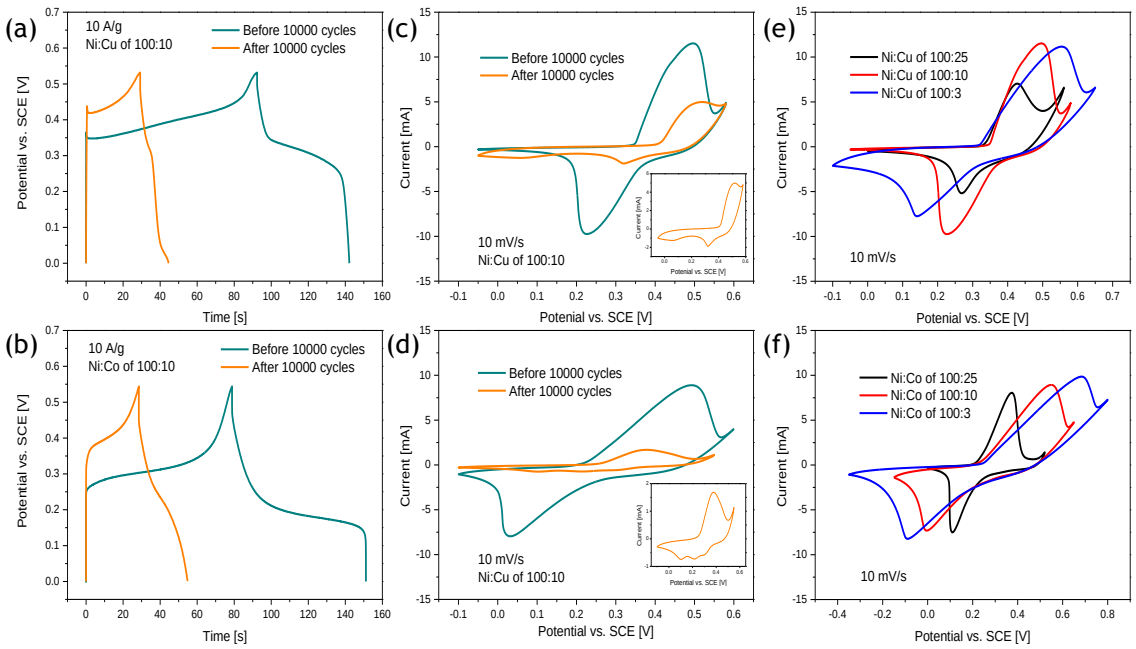

Figure 4.3 (a) and (b) CD curves of Ni-Cu-OH and Ni-Co-OH electrodes of 100:10, respectively. (c) and (d) CV curves of Ni-Cu-OH and Ni-Co-OH electrodes of 100:10, respectively. Enlarged CVs curves after 10000 cycles are shown in the *insets*. (e) and (f) CV curves of Ni-Cu-OH and Ni-Co-OH electrodes, respectively, of 100:25, 100:10 and 100:3.

4.3.2. Electrochemical Performance

Figure 4.3 (a) and (b) shows the CD behavior of Ni-Cu-OH and Ni-Co-OH electrodes of 100:10, respectively. Before 10,000 cycles, there are two separate charging plateaus. The first plateau spans a potential of 0.348 to 0.450 V, while the second plateau spans from 0.450 to 0.532 V. After 10,000 cycles, the first charging plateau is shifted toward higher potential from 0.419 to 0.480 V, while the second plateau covers from 0.480 V to the preset maximum charging potential (0.532 V) which is fixed during all 10,000 cycles. This shift in the range of charging plateaus toward higher potentials indicates can be one of the reasons behind the capacitance decay during long CD cycles

as confirmed and explained in the following CV results section. In addition, there are two separated discharging plateaus after 10,000 cycles instead of one discharging plateau. Similar CD behavior is also observed for Ni-Co-OH electrode as seen in **Figure 4.3 (c)**, but with one broad plateau in the discharge curve consisting of two or more overlapping plateaus. As expected, both Ni-Cu-OH and Ni-Cu-OH electrodes have shorter charging-discharging time after 10,000 cycles, indicating a decrease in capacitance as shown in **Figure 4.4**. All previous changes in the potential plateau, number of plateaus and shape of charging-discharging curves can be due to structural rearrangement in the electrode materials as confirmed by CV curves in **Figure 4.3 (c) and (d)**. CD curves at different current densities of all Ni-Cu-OH and Ni-Co-OH electrodes of 100:3, 100:10 and 100:25 are shown in **Figure 4.10** of the Supplementary Information.

Figure 4.3 (c) and (d) illustrates CV behavior of Ni-Cu-OH and Ni-Co-OH electrodes of 100:10, respectively. Before 10,000 cycles, it can be seen in **Figure 4.3 (c)** that there are two partially overlapping oxidation peaks that can be attributed to $Ni(OH)_2$/NiOOH and $Cu(OH)_2$/CuOOH based on the following well-known reactions in which electrons can be stored and then released, reversely:

$$Ni(OH)_2 + OH^- \leftrightarrow NiOOH + H_2O + e^- \qquad \textbf{Equation 4.1}$$

$$Cu(OH)_2 + OH^- \leftrightarrow CuOOH + H_2O + e^- \qquad \textbf{Equation 4.2}$$

After 10,000 cycles, the oxidation peak of Ni–Cu–OH electrode is shifted towards higher potential than the initial one of the same electrode. In addition, there are two separated reduction peaks after 10,000 cycles instead of the initial overlapping one. These two observations are in agreement with a similar reported case for $Ni(OH)_2$ electrode [24] and can be explained based on Bode's diagram of the electrochemical phase transformation of nickel hydroxide in alkaline solution.[68] One of the Bode's diagram findings is that the redox potential of β-$Ni(OH)_2$/β-NiOOH is higher than that of α-$Ni(OH)_2$/γ-NiOOH. Analogous to Bode's diagram, our Ni–Cu–OH electrode may have α-$Ni(OH)_2$/γ-NiOOH and α-$Cu(OH)_2$/γ-CuOOH coupled phases in the initial cycles and then they may be transformed to β-$Ni(OH)_2$/β-NiOOH and β-$Cu(OH)_2$/β-CuOOH coupled phases due to prolonged cycling in alkaline electrolyte (KOH). Similar CV behavior is also observed for Ni–Co–OH electrode as seen in **Figure 4.3 (d)**. However, three separated reduction peaks are observed after 10,000 cycles, which supports our prediction of the phase transformations from α-$Ni(OH)_2$/γ-NiOOH and α-$Co(OH)_2$/γ-CoOOH in the initial cycles to β-$Ni(OH)_2$/β-NiOOH and β-$Co(OH)_2$/β-CoOOH in the final cycles.

Figure 4.3 (e) and (f) compares the CVs of Ni–Cu–OH and Ni–Co–OH electrodes, respectively, at the same scan rate of 10 mV/s. Based on the well-generalized relationship stating that smaller potential separation between CV redox peaks indicates higher redox reversibility, it can be concluded that our Ni–Cu–OH electrode of 100:25 has better redox reversibility than Ni–Cu–OH electrodes of 100:10 and 100:3 as indicated by **Figure 4.3 (e)**. Similarly, Ni–Co–

OH electrode of 100:25 has better redox reversibility than Ni-Co-OH electrodes of 100:10 and 100:3 as indicated in **Figure 4.3 (f)**. This redox reversibility seems to lead to better cycling stability of the devices. CVs at different scan rates of all Ni-Cu-OH and Ni-Co-OH electrodes of 100:3, 100:10 and 100:25 are shown in **Figure 4.11** of the Supplementary Information.

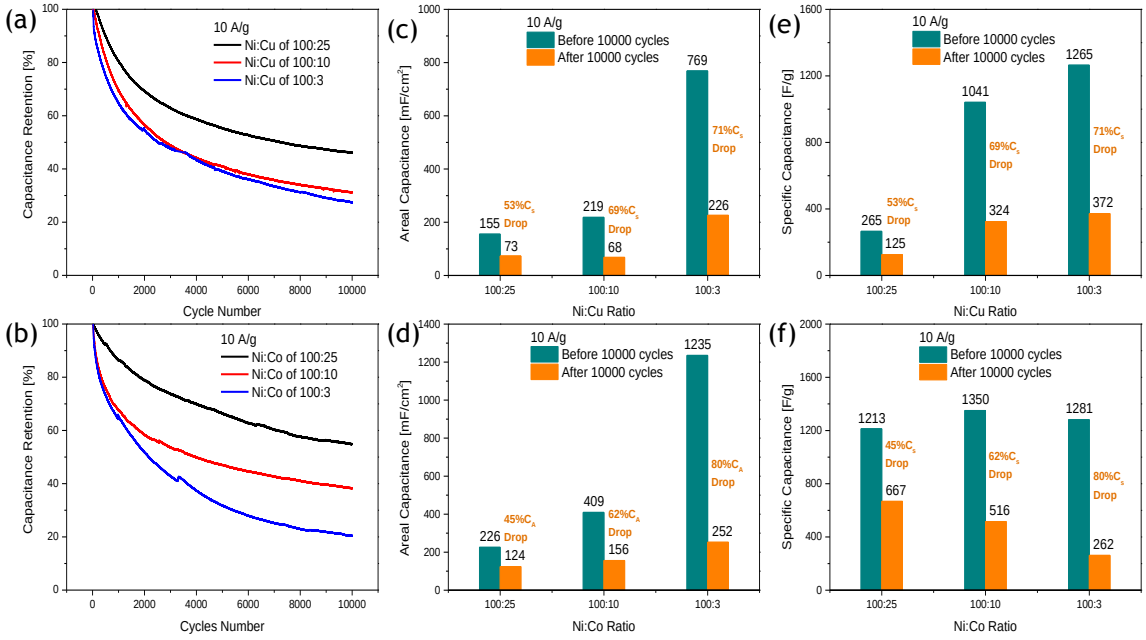

Figure 4.4 (a) and (b) The cycling stability curves of Ni-Cu-OH and Ni-Co-OH electrodes, respectively. (c) and (d) Areal capacitances of Ni-Cu-OH and Ni-Co-OH electrodes, respectively. (e) and (f) Specific capacitances of Ni-Cu-OH and Ni-Co-OH electrodes, respectively.

Figure 4.4 (a) and (b) represents the cycling stability curves of Ni-Cu-OH and Ni-Co-OH electrodes, respectively, of 100:3, 100:10 and 100:25. It can be concluded that using Ni-Cu-OH and Ni-Co-OH electrodes of 100:25 leads to higher capacitance retention during 10,000 CD cycles at 10 A/g, than that of other electrodes of 100:10 and 100:3. This improvement in cycling stability can

be ascribed to the characteristic difference in the redox reversibility as indicated by previous CV curves. In addition, Ni–Co–OH electrode of 100:25 exhibits higher capacitance retention of 55% than 47% exhibited by Ni–Cu–OH of 100:25, after 10,000 CD cycles at 10 A/g. Areal capacitances of Ni–Cu–OH and Ni–Co–OH electrodes are compared in **Figure 4.4 (c) and (d)**, respectively, while specific capacitances are compared in **Figure 4.4 (e) and (f)** for Ni–Cu–OH and Ni–Co–OH electrodes, respectively. As Ni–Cu–OH and Ni–Co–OH electrodes can be used in rechargeable alkaline batteries, areal and specific capacities are calculated and compared in **Figure 4.12** of the Supplementary Information. Both areal and specific capacitances have been calculated from CD curves of **Figure 4.4 (a) and (b)**. It is concluded that using Ni–Cu–OH and Ni–Co–OH electrodes 100:3 leads to better areal capacitance than that of other electrodes of 100:10 and 100:25. Such differences in capacitances are expected due to the different morphologies as shown in previous SEM images. Ni–Co–OH electrode of 100:10 seems to be the optimum composition of our electrode as it has higher capacitance retention than Ni–Cu–OH and Ni–Co–OH electrodes of 100:3 in addition to higher areal and specific capacitances than Ni–Cu–OH and Ni–Co–OH electrodes of 100:25.

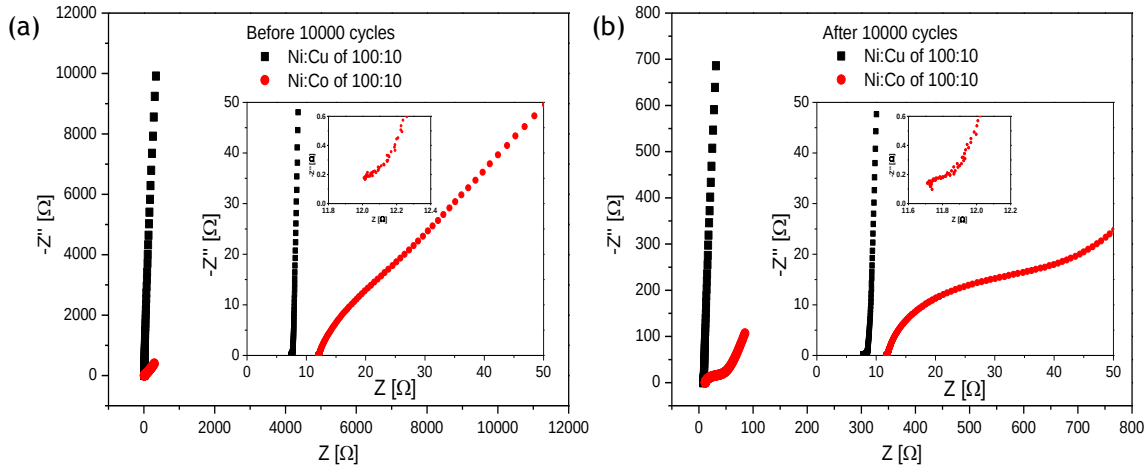

Figure 4.5 (a) and (b) Complex impedance (Nyquist) plots of Ni-Cu-OH and Ni-Co-OH electrodes of 100:10 before and after 10,000 cycles, respectively. Enlarged. Nyquist plots are shown in the *insets*.

Electrochemical impedance spectroscopy results of Ni-Cu-OH and Ni-Co-OH electrodes of 100:10 are represented by the complex impedance (Nyquist) plots in **Figure 4.5 (a) and (b)**, respectively. At low frequencies, the 45° phase angle of Ni-Co-OH electrode's Nyquist plot represents the presence of Warburg impedance (*W*) that is due to diffusion of electrolyte ions to the electrode. At high frequencies, Ni-Cu-OH electrode has smaller equivalent series resistance (ESR) than Ni-Co-OH electrode, as can be seen from the *x*-axis intercept. After 10,000 cycles, the semicircles became more obvious and larger than the initial semicircles. Such increase in charge transfer resistance (R_{CT}) during prolonged cycling is one of the factors behind the decrease in capacitance.

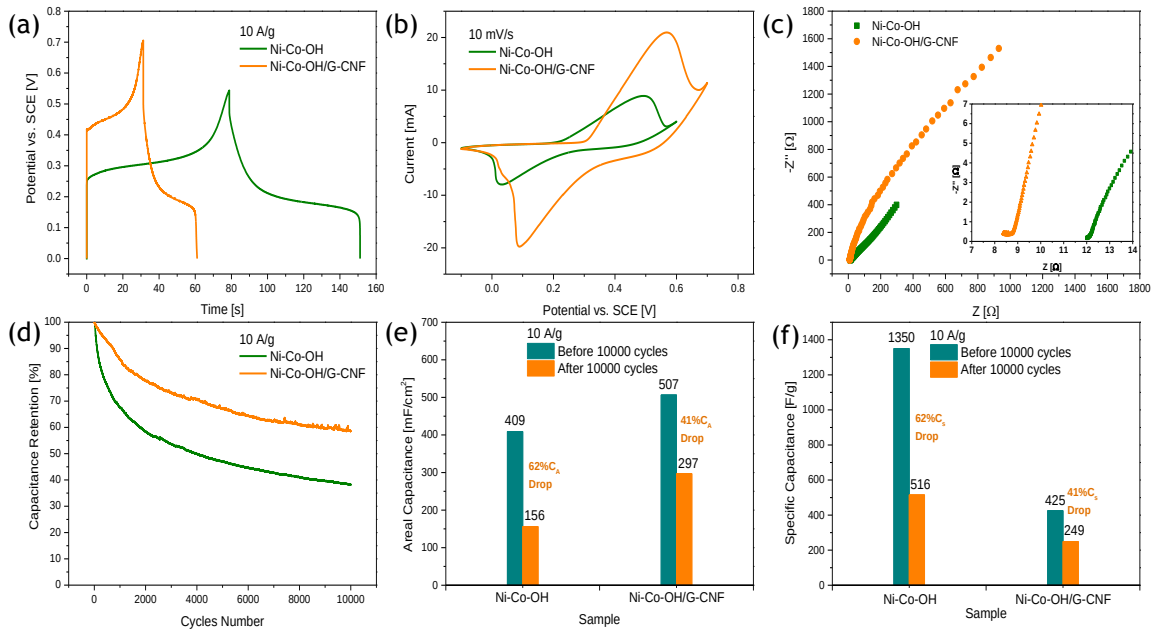

Figure 4.6 (a) CD of Ni-Co-OH and Ni-CoOH/ G-CNF electrodes. (b) CV of Ni-Co-OH and Ni-Co-OH/G-CNF electrodes. (c) Nyquist plot of Ni-Co-OH and Ni-Co-OH/G-CNF electrodes. Enlarged Nyquist plots are shown in the *insets*. (d) Cycling stability curves of Ni-Co-OH and Ni-Co-OH/G-CNF electrodes. (e) and (f) Area and specific capacitances of Ni-Co-OH and Ni-Co-OH/G-CNF electrodes, respectively.

Figure 4.6 shows the electrochemical performance of Ni-Co-OH/G-CNF electrode compared with the previous Ni-Co-OH electrode of Ni:Co ratio of 100:10. Adding G-CNF to Ni-Co-OH electrode leads to increase potential window as seen in CD and CV curves in **Figure 4.6 (a) and (b)**, respectively, as expected. **Figure 4.6 (c)** of Nyquist plot shows that the ESR of Ni-Co-OH/G-CNF is smaller than that of Ni-Co-OH due to the electrical conductivity of graphene. Moreover, adding G-CNF to Ni-Co-OH electrode leads to enhanced capacitance retention over 10,000 cycles as shown in **Figure 4.6 (d).** This improvement in the cycling stability can be explained by the fact that there is no phase transformation involved during the charge-discharge process of G-CNF

electrode. **Figure 4.6 (e) and (f)** represents areal capacitance and specific capacitance, respectively. Ni-Co-OH/G-CNF electrode has higher areal capacitance (507 mF/cm^2) than Ni-Co-OH electrode (409 mF/cm^2). By taking into account that both electrodes have the same substrate area (1 cm^2), the areal capacitances of these electrodes are actually equivalent to their absolute capacitances. The specific capacitances cannot be measured accurately as shown in **Figure 4.6 (f)** due to the big difference in mass loadings of Ni-Co-OH/G-CNF and Ni-Co-OH. The mass loading of Ni-Co-OH/G-CNF (1.19 mg/cm^2) is 4 times higher than that of Ni-Co-OH (0.30 mg/cm^2) because Ni-Co-OH can be deposited on larger surface area when using G-CNF carbon microfibers than using only carbon microfibers. As Ni-Co-OH/G-CNF electrode can be used in rechargeable alkaline batteries, areal and specific capacities are calculated and compared in **Figure 4.12 (c) and (d)** of the Supplementary Information.

4.4. CONCLUSIONS

In this project, Ni-Cu-OH and Ni-Co-OH electrodes were prepared using different Ni:Cu and Ni:Co ratios by CBD at room temperature on carbon microfibers. It is observed that incorporation of Co at lower concentration (100:10) enhances nanoflake formation and hence increases capacitance and cycling stability. The improvement in cycling stability can be ascribed to the characteristic difference in the redox reversibility as indicated by CV curves. Phase transformations of Ni-Cu-OH and Ni-Co-OH electrodes are indicated by the shifting and the splitting of CD plateaus and the shifting and the splitting of

CV redox peaks. Composites based on the ternary hydroxides, graphene and carbon nanofibers on carbon microfibers increase potential window, decrease equivalent series resistance (ESR), areal capacitance and enhance cycling stability.

ACKNOWLEDGMENT

Research reported in this publication was supported by King Abdullah University of Science and Technology (KAUST).

SUPPORTING INFORMATION

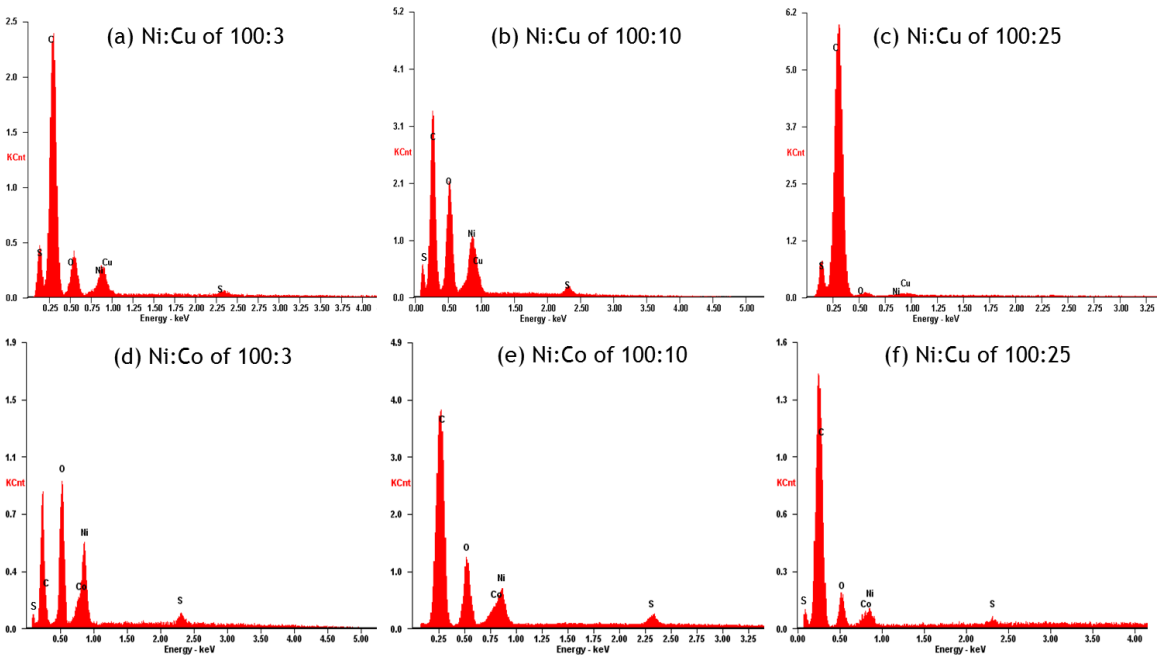

Figure 4.7 (a)-(c) EDX spectra confirm the presence of C, O, Ni and Cu on all Ni-Cu-OH electrodes. (d)-(f) EDX spectra confirm the presence of C, O, Ni and Co on all Ni-Co-OH electrodes.

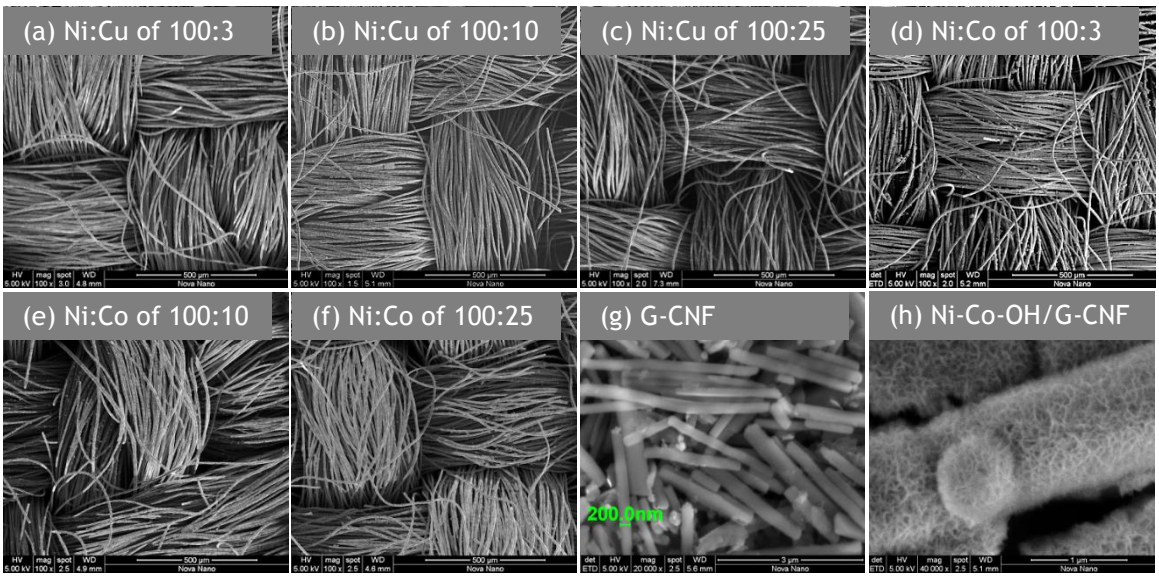

Figure 4.8 (a), (b) and (C) Small magnification SEM images of Ni-Cu-OH electrodes of 100:3, 100:10 and 100:25 Ni:Cu ratios, respectively. (d), (e) and (f) Small magnification images of Ni-Co-OH electrodes of 100:3, 100:10 and 100:25 Ni:Co ratios, respectively. (g) G-CNF electrode. (h) Ni-Co-OH/G-CNF electrode prepared by 2h of CBD.

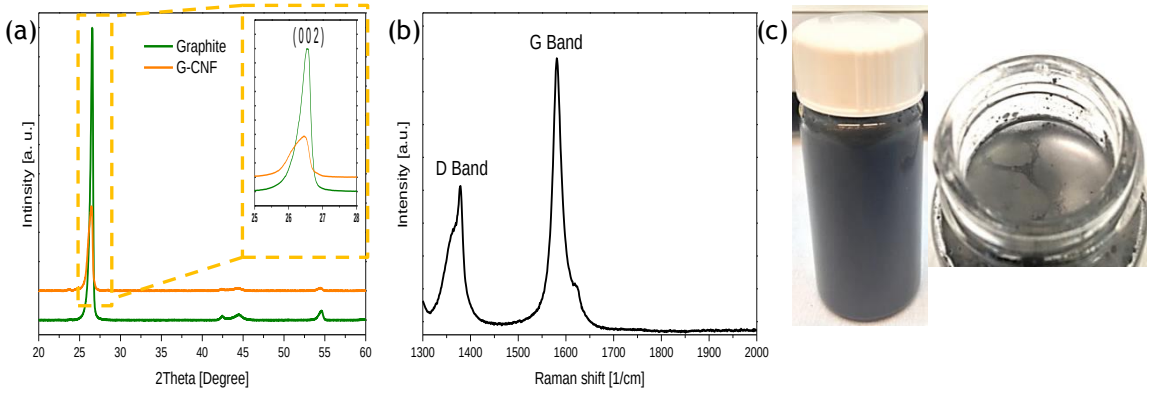

Figure 4.9 (a) XRD pattern of graphite and G-CNF. (b) Raman spectrum of G-CNF. (c) Photographs of G-CNF in water and methanol.

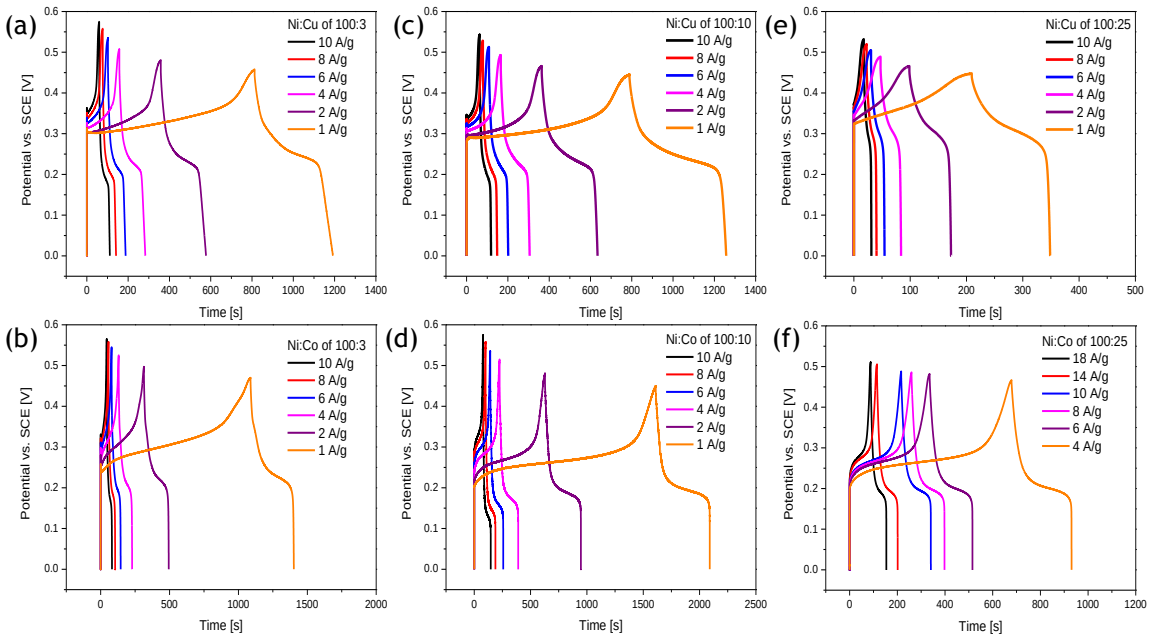

Figure 4.10 (a), (b) and (c) Charge-discharge plots of Ni-Cu-OH electrodes of 100:3, 100:10 and 100:25 Ni:Cu ratios, respectively. (d), (e) and (f) Charge-discharge plots of Ni-Co-OH electrodes of 100:3, 100:10 and 100:25 Ni:Co ratios, respectively.

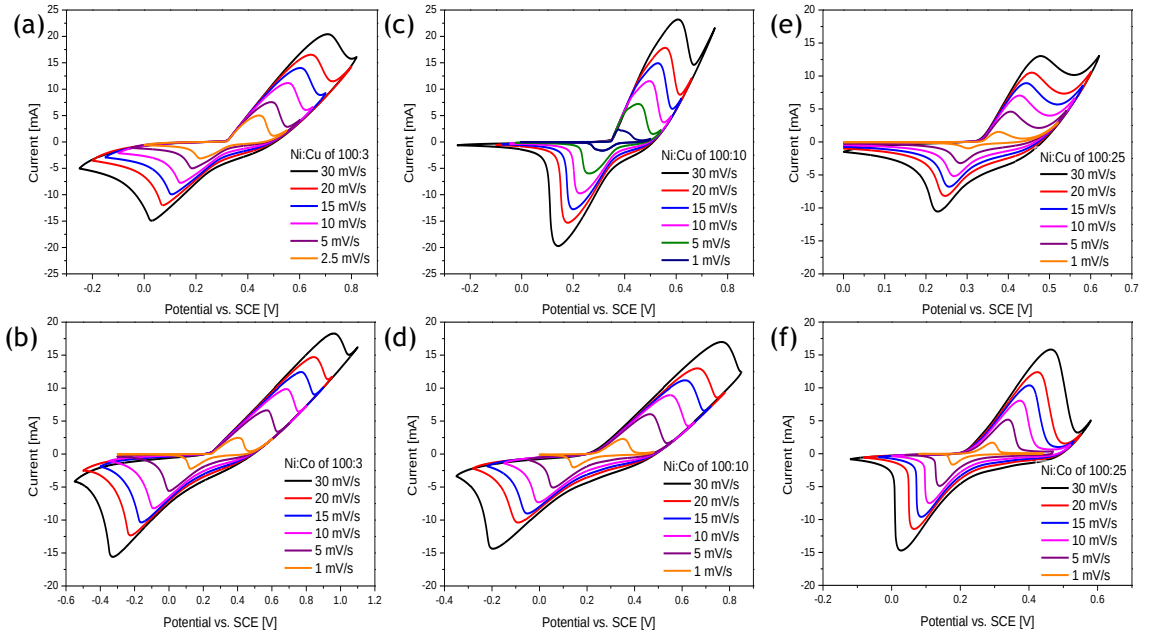

Figure 4.11 (a), (b) and (c) CV plots of Ni-Cu-OH electrodes of 100:3, 100:10 and 100:25 Ni:Cu ratios, respectively. (d), (e) and (f) CV plots of Ni-Co-OH electrodes of 100:3, 100:10 and 100:25 Ni:Co ratios, respectively.

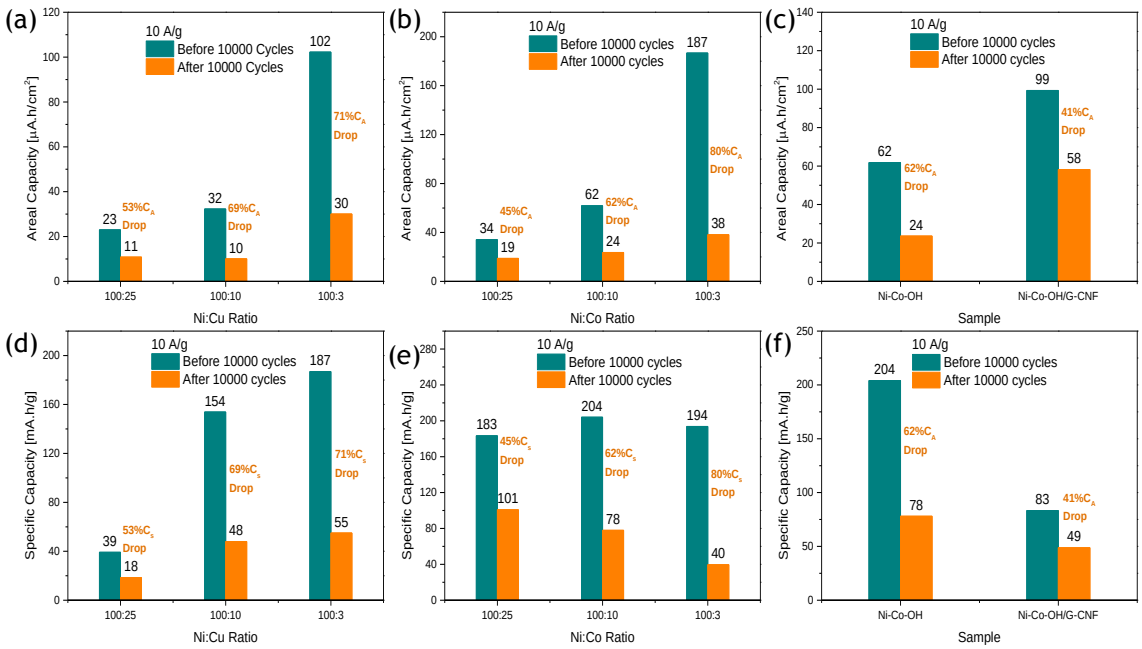

Figure 4.12 (a) and (b) Areal capacity of Ni-Cu-OH and Ni-Co-OH electrodes, respectively. (c) Areal capacity of Ni-Co-OH (100:10) and Ni-Co-OH/G-CNF electrodes. (d) and (e) Specific capacity of Ni-Cu-OH and Ni-Co-OH electrodes, respectively. (f) Specific capacity of Ni-Co-OH (100:10) and Ni-Co-OH/G-CNF electrodes.

Chapter 5 . NICKEL-BASED ASYMMETRIC SUPERCAPACITORS

Nuha A. Alhebshi and H. N. Alshareef, *Flexible and low-cost asymmetric supercapacitors based on Ni-Co-OH and Graphene-carbon nanofibers Electrodes*, to be submitted.

ABSTRACT

In this project, we have fabricated $Ni(OH)_2$ based asymmetric supercapacitors with enhanced electrochemical performance, flexible-electrodes, low-cost fabrication process, and environmentally friendly materials. Ni-based electrodes have been prepared by chemical bath deposition (CBD). Graphene and carbon nanofibers (G-CNF) electrodes have been prepared by chemical exfoliation method. Both electrodes have been deposited at room temperature on flexible carbon microfibers as current collectors. $Ni(OH)_2$//Graphene asymmetric supercapacitor results in an areal capacitance of 253 mF/cm^2 at 5 mA/cm^2 which is higher than reported 185 mF/cm^2 at 5 mA/cm^2 for NiO//rGO asymmetric supercapacitor prepared by hydrothermal method. Ni-Co-OH/G-CNF//Graphene asymmetric supercapacitor results in a maximum power of 23 mW within 2.2 V which is higher than the maximum power and the maximum operating voltage of our $Ni(OH)_2$//Graphene (15.94 mW within 1.8 V).

5.1. INTRODUCTION

The recent trend in supercapacitors research has been trending toward fabricating asymmetric supercapacitors.[38] Asymmetric supercapacitors consist of two dissimilar electrodes; e.g., one of its electrodes can be porous materials and the other electrode can be transition metal oxide/hydroxides. The main feature of asymmetric supercapacitors is a wider cell voltage than symmetric supercapacitors, which can in principle lead to higher energy density and better capacitance by utilization of both storage mechanisms of electrical double layer and redox reactions.

An asymmetric supercapacitor of $Ni(OH)_2$/CNT//reduced graphene oxide (rGO), prepared by modified hummers method and CBD, has been reported with a specific capacitance of 78.33 F/g and a specific energy of 35.24 Wh/kg at 2 A/g.[34] Similar asymmetric supercapacitor of $Ni(OH)_2$/CNT//activated carbon (AC), prepared by chemical vapor deposition (CVD) and CBD, has been reported with a specific energy of 50.6 Wh/kg and a cycling stability of 17% C_s loss after 3000 cycles.[35] It has been achieved a higher specific energy, 77.8 Wh/kg, for a $Ni(OH)_2$/rGO//porous graphene asymmetric supercapacitor, with a cell voltage of 1.6 V, specific capacitance of 218.4 F/g and 5.7% C_s loss after 3000 cycles.[39] Ni-Co-OH//rGO asymmetric supercapacitor, prepared by CBD and chemical reduction, has been reported with a cell voltage of 1.5 V and a specific power range from 0.32 kW/kg to 5 kW/kg.[36] $Co_3O_4/Ni(OH)_2$//rGO asymmetric supercapacitor, prepared by CBD, hydrothermal and chemical

reduction, has been reported with a specific capacitance of 95.7 F/g at 5 mA/cm^2.[37]

5.2. EXPERIMENTAL METHODS

5.2.1. Synthesis of Graphene and Carbon Nanofibers Electrodes

Graphene and carbon nanofibers (G-CNF) were prepared by chemical exfoliation. A mixture of 100 mg of graphite and 16.5 mg of 1-pyrenecarboxylic acid (PCA) in 50 mL of methanol were sonicated for 45 minutes (BRANSON Ultrasonic Cleaner 2510). Then, additional 200 mL of DI H_2O was added to the mixture with continuous sonication for several hours. G-CNF were collected by vacuum filtering using nanoporous membrane (Celgard 3501). The collected G-CNF were dissolved in ethanol and casted drop by drop on carbon microfibers substrate at 60^oC followed by washing with DI H_2O several times and drying in air overnight. For comparison purposes, a commercial graphene was dissolved with polytetrafluoroethylene (PTFE) in ethanol and casted drop by drop on carbon microfibers substrate at 60 ^oC followed by washing with DI H_2O several times and drying in air overnight.

5.2.2. Synthesis of $Ni(OH)_2$ and Ni-Co-OH/G-CN Electrodes

$Ni(OH)_2$ and Ni-Co-OH electrodes were prepared by CBD with Ni:Co ratios of 100:0 and 100:10, respectively. The chemical bath consisted of fixed 1M of Nickel(II) Sulfate Hexahydrate ($NiSO_4.6H_2O$), changed molarities (0M and 0.10M) of Cobalt(II) Chloride Hexahydrate ($CoCl_2.6H_2O$) and deionized (DI) water (H_2O)

in Pyrex beakers at room temperature. Then, 1.56 mL of ammonium hydroxide solution (30-33% NH_3 in H_2O) and 0.15M of potassium persulfate ($K_2S_2O_8$) were added subsequently to the mixture. Several pieces of commercial carbon microfibers substrates from Fuel Cell Store (carbon cloth 7302003, 99% carbon content and 11.5 mg/cm^2) were immersed in the chemical bath by clamps at room temperature. The immersed parts of all carbon substrates have the same area of 1.00 cm^2. After 2 h, the coated substrates were taken out, washed several times by DI H_2O and dried in air at room temperature overnight. All the chemicals used in this project are analytical grade (SIGMA-ALDRICH) and without further purification. Finally, G-CNF on carbon microfibers were used as substrates in CBD of the same previous procedure of Ni-Co-OH to prepare Ni-Co-OH/G-CNF electrodes.

5.2.3. Materials Characterization

The mass loading of each electrode was calculated by weighing the carbon substrate before and after the CBD using a sensitive microbalance from METTLER TOLEDO (XP26, 0.001 mg resolution). The morphology of G-CNF, $Ni(OH)_2$, Ni-Co-OH/G-CNF electrodes were observed by scanning electron microscope (SEM) at different magnifications.

5.2.4. Electrochemical Measurements

For full-cell measurements, two asymmetric supercapacitors have been fabricated. First, $Ni(OH)_2$ was used as a positive electrode and graphene was used as a negative electrode for comparison proposes. Second, Ni-Co-OH on G-

CNF were used as a positive electrode and graphene was used as a negative electrode. The aqueous electrolyte solution was 1M of potassium hydroxide (KOH). Electrochemical redox reactions were studied by cyclic voltammetry (CV). Electrode capacitances and cycling stability were calculated by chronopotentiometry charge-discharge (CD). Equivalent series resistances, charge transfer resistances and the diffusion control were studied by electrochemical impedance spectroscopy (EIS). All experiments were carried out using a multi-channel Potentiostat/ Galvanostat/ EIS from BioLogic Science Instruments (VMP3).

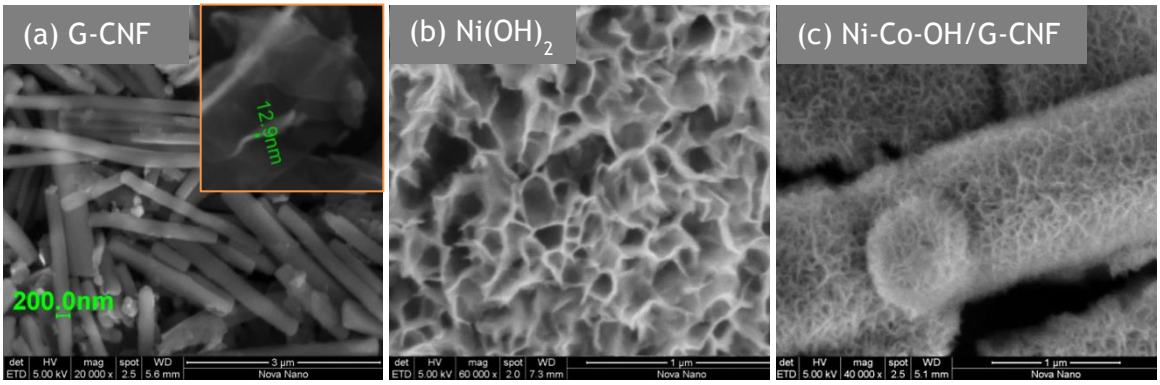

Figure 5.1 SEM images of (a) Carbon nanofibers (graphene in inset). (b) Nickel hydroxide. (c) Nickel-cobalt hydroxides on graphene and carbon nanofibers.

5.3. RESULTS AND DISCUSSIONS

5.3.1. Materials Properties

Figure 5.1 (a) shows the morphology of G-CNF. It can be seen that the carbon nanofiber diameter is around 200 nm and the graphene thickness is around 13 nm. **Figure 5.1 (b)** shows that $Ni(OH)_2$ has nanoflakes morphology in

which preferred for electrolyte penetration into the electrode. Similar nanoflakes morphology has been seen for Ni-Co-OH on G-CNF as shown in **Figure 5.1 (c).** In addition, it can be shown that Ni-Co-OH nanoflakes were coated conformally around carbon nanofibers. All G-CNF, $Ni(OH)_2$ and Ni-Co-OH/G-CNF samples were coated conformally on carbon microfibers as shown in **Figure 5.7** of the Supporting Information.

5.3.2. Electrochemical Performance

Figure 5.2 shows an illustration of our asymmetric supercapacitor configuration. In $Ni(OH)_2$//Graphene asymmetric supercapacitor, $Ni(OH)_2$ was used as a positive electrode (cathode) and graphene was used as negative electrode (anode) separated by nanoporous polypropylene separator as seen in **Figure 5.2 (a).** In Ni-Co-OH//Graphene asymmetric supercapacitor, the hydroxide was used as a positive electrode, and graphene was used as negative electrode separated by nanoporous polypropylene separator as seen in **Figure 5.2 (b).** In **Figure 5.2 (c)**, stainless steel coin cell was used to test our asymmetric supercapacitors in full cell configuration as a standard-elementary cell. Our flexible electrodes can be further implemented in flexible cells.

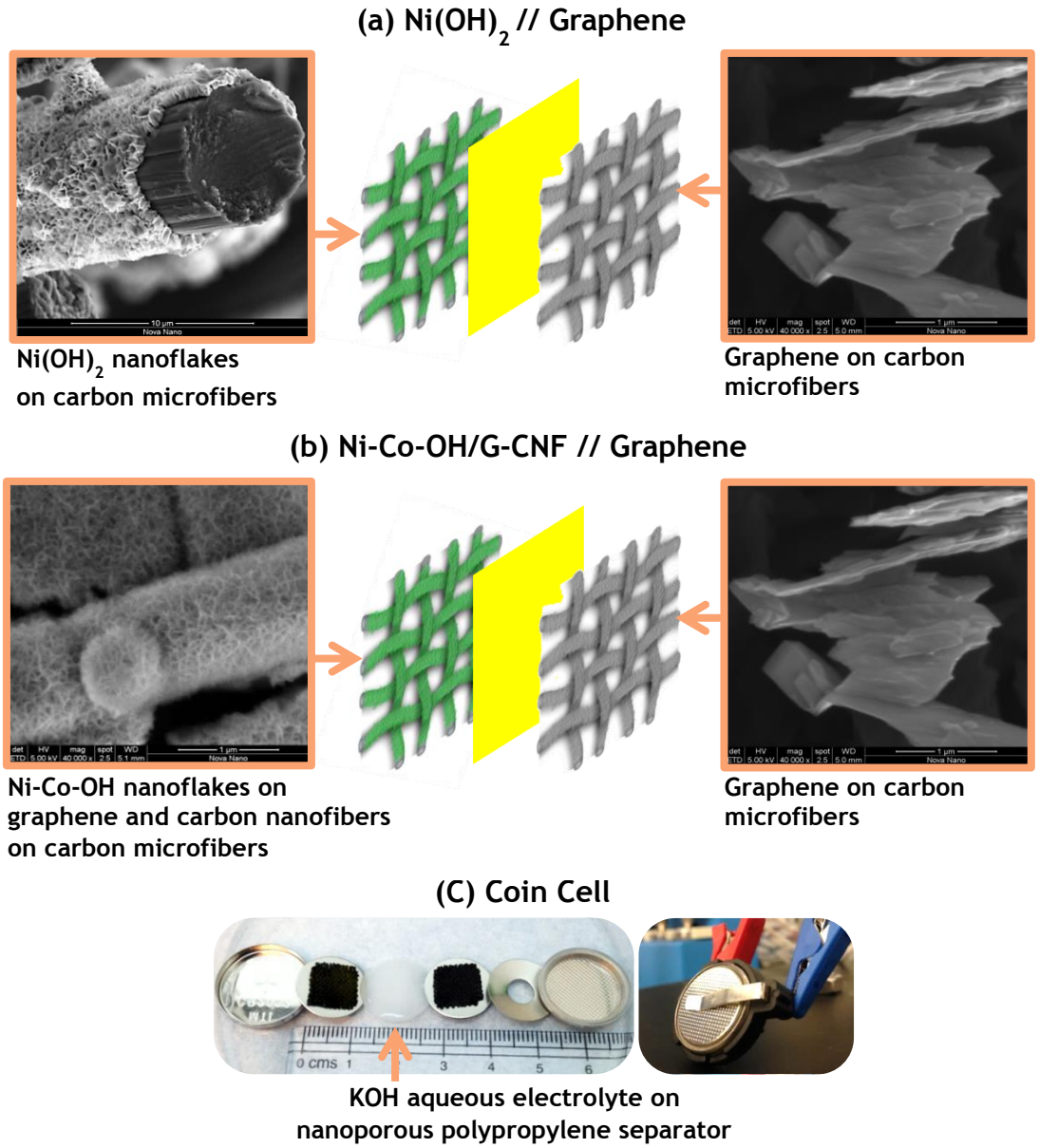

Figure 5.2 (a) SEM images and sketch of $Ni(OH)_2$ and graphene electrodes. (b) SEM images and sketch of Ni-Co-OH/G-CNF and graphene electrodes. (c) Photographs of an asymmetric supercapacitor in coin cell.

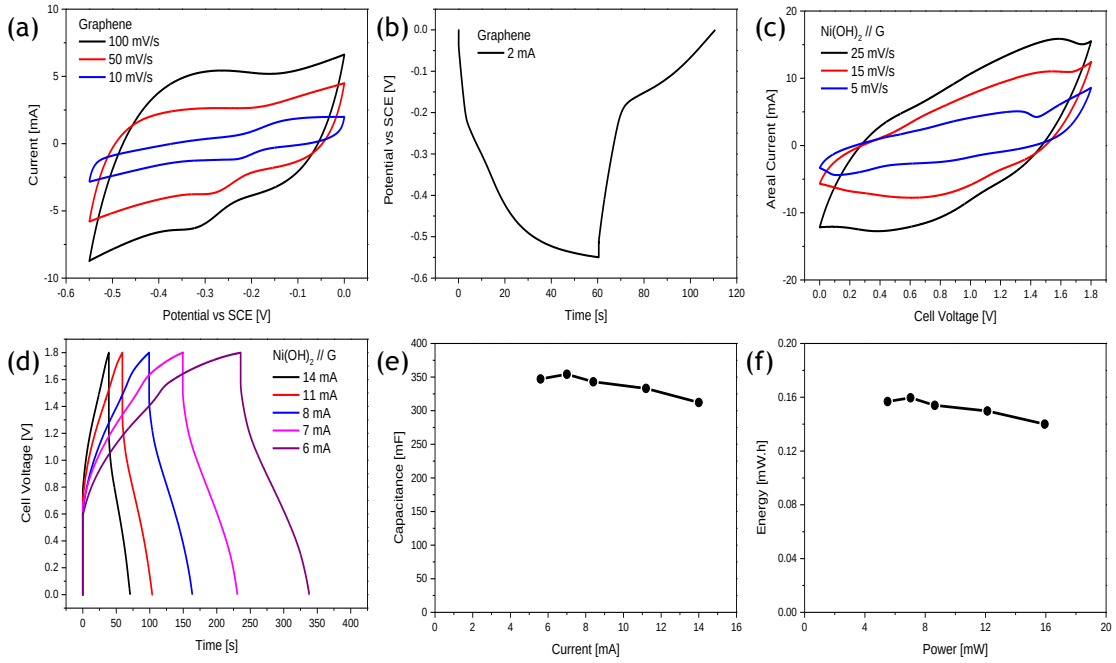

Figure 5.3 (a) and (b) CV and CD curves of graphene electrode, respectively. (c) and (d) CV and CD of $Ni(OH)_2$//Graphene asymmetric supercapacitor, respectively. (e) Capacitance of $Ni(OH)_2$//Graphene asymmetric supercapacitor at different current values. (d) Energy and power of $Ni(OH)_2$//Graphene asymmetric supercapacitor.

Figure 5.3 (a) shows CV curves of graphene electrode at different scan rates (from 10 mV/s to 100 mV/s) in the negative potential range (from 0 V to -0.55 V). A capacitance of 193.2 mF at 2 mA has been achieved by the graphene electrode as calculated from the CD curve of **Figure 5.3 (b)** using **Equation 5.1**.

CV and CD curves of $Ni(OH)_2$//Graphene asymmetric supercapacitor are shown in **Figure 5.3 (c) and (d)** at different scan rates and current values, respectively. Our $Ni(OH)_2$//Graphene asymmetric supercapacitor can be charged and discharged in scan rates up to 25 mV/s within a cell voltage of 1.8

V which is wider than 1.7 V reported for NiO//reduced graphene oxide (rGO) asymmetric supercapacitor prepared by hydrothermal method.[69]

Figure 5.3 (e) shows the capacitance of $Ni(OH)_2$//Graphene asymmetric supercapacitor at different current values as calculated using **Equation 5.1**. The areal capacitance at different current values is shown in **Figure 5.8 (a)** of the Supporting Information. The areal capacitance of our $Ni(OH)_2$//Graphene asymmetric supercapacitor (253 mF/cm^2 at 5 mA/cm^2) is higher than that of NiO//rGO asymmetric supercapacitor (185 mF/cm^2 at 5 mA/cm^2) prepared by hydrothermal method.[69]

Figure 5.3 (f) shows the energy and power of $Ni(OH)_2$//Graphene asymmetric supercapacitor. The areal energy and areal power are shown in **Figure 5.8 (b)** of the Supporting Information. Our $Ni(OH)_2$//Graphene asymmetric supercapacitor have a maximum energy of 0.16 mW.h at a power of 7.03 mW and a maximum power of 15.94 mW at an energy of 0.14 mW.h.

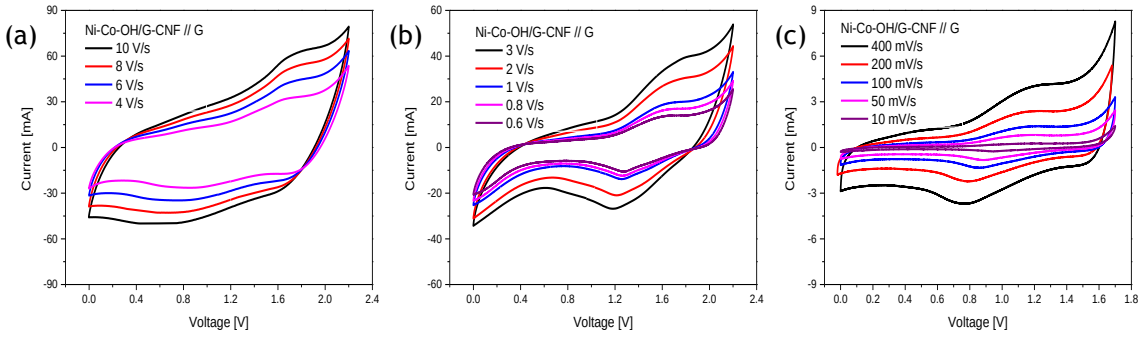

Figure 5.4 CV curves of Ni-Co-OH/G-CNF//Graphene asymmetric supercapacitor at different scan rates.

CV curves of Ni-Co-OH/G-CNF//Graphene asymmetric supercapacitor are shown in **Figure 5.4.** Both the redox peaks and the semi-rectangular CV shape can be clearly seen until a higher scan rate (10 V/s) than our previous $Ni(OH)_2$//Graphene (25 mV/s). This improvement in scan rates can be due to inserting graphene and carbon nanofibers between Ni-Co-OH and carbon microfibers, facilitating a quicker permeability of electrolyte ions onto the nanofibrous design of Ni-Co-OH/G-CNF electrode than the microfibrous design of $Ni(OH)_2$ electrode.

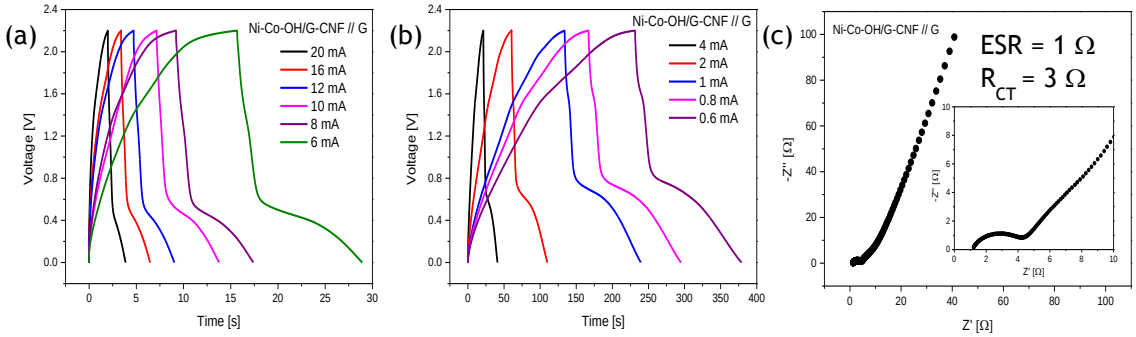

Figure 5.5 (a) and (b) CD curves of Ni-Co-OH/G-CNF//Graphene asymmetric supercapacitor at different current values. (c) Complex plane of electrochemical impedance spectroscopy (Nyquist plot) of Ni-Co-OH/G-CNF//Graphene asymmetric supercapacitor with an enlarged scale in the inset.

CD curves of Ni-Co-OH/G-CNF//Graphene asymmetric supercapacitor are shown in **Figure 5.5 (a) and (b)**. Ni-Co-OH/G-CNF//Graphene asymmetric supercapacitor can be charged and discharged at wide constant current range from 0.6 mA up to 20 mA. In addition, the operating voltage of 2.2 V is wider than the operating voltage of our previous $Ni(OH)_2$//Graphene (1.8 V). Such improvement in operating voltage can be due to adding graphene and carbon nanofibers to Ni-Co-OH on the same electrode. In fact, Ni-Co-OH and G-CNF

can be considered as two capacitors connected in series because one side of G-CNF is directly connected to the current collector (carbon microfibers) and the other side of G-CNF is directly connected to the Ni-Co-OH nanoflakes. It is well known that the equivalent voltage of the two series capacitors is the sum of the voltage of individual capacitors.

Complex plane of electrochemical impedance spectroscopy (Nyquist plot) of Ni-Co-OH/G-CNF//Graphene asymmetric supercapacitor is shown in **Figure 5.5 (c)**. An equivalent series resistance (ESR) of 1 Ω is calculated from the intercept of the x-axis, while a charge transfer resistance (R_{CT}) of 3 Ω is calculated from the diameter of the semi-circle.

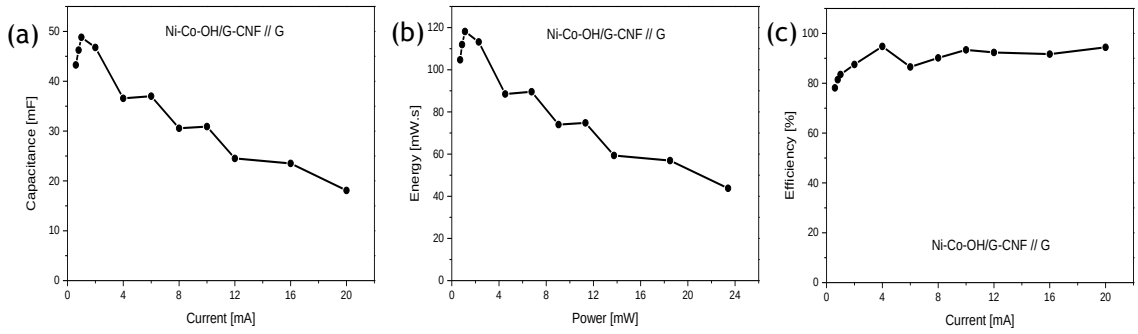

Figure 5.6 (a) Capacitance of Ni-Co-OH/G-CNF//Graphene asymmetric supercapacitor at different current values. (d) Energy and power diagram (Ragone plot) of Ni-Co-OH/G-CNF//Graphene asymmetric supercapacitor. (c) Efficiency of Ni-Co-OH/G-CNF//Graphene asymmetric supercapacitor at different current values.

Capacitance of Ni-Co-OH/G-CNF//Graphene asymmetric supercapacitor at different current values is calculated by **Equation 5.1** and shown in **Figure 5.6 (a).** The maximum capacitance of 49 mF at 1 mA for Ni-Co-OH/G-CNF//Graphene asymmetric supercapacitor is lower than the capacitance of

our previous $Ni(OH)_2$//Graphene asymmetric supercapacitor due to the fact that is the reciprocal of the equivalent capacitance of two series capacitors is the sum of the reciprocals of the individual capacitances. As mentioned earlier, Ni-Co-OH and G-CNF can be considered as two capacitors connected in series. Therefore, it is expected to have lower capacitance for Ni-Co-OH/G-CNF than $Ni(OH)_2$.

Energy and power plot of $Ni(OH)_2$//Graphene asymmetric supercapacitor is shown in **Figure 5.6 (b)**. A maximum energy of 118 mW.s is recorded at 1 mA, while a maximum power of 23 mW is achieved at 20 mA. In addition, a power of 16.12 mW at 14 mA is slightly higher than the maximum power of our previous $Ni(OH)_2$//Graphene asymmetric supercapacitor (15.94 mW at 14 mA). Such improvement in the power can be due to the higher electrical conductivity of Co, graphene and carbon nanofiber than $Ni(OH)_2$.

Efficiency of Ni-Co-OH/G-CNF//Graphene asymmetric supercapacitor at different current values is shown in **Figure 5.6 (c)**. At low current, where the charge time is longer than at higher current, the low charge-discharge efficiency of 78% can be ascribed to the self-discharge or leakage during the long charge time. At high current, the charge-discharge efficiency is stabilized around 92%.

5.4. CONCLUSIONS

$Ni(OH)_2$ and Ni-Co-OH electrodes were prepared by chemical bath deposition *in-situ* on carbon microfibers at room temperature. G-CNF electrodes were prepared by chemical exfoliation method. $Ni(OH)_2$//Graphene and Ni-Co-OH/G-CNF//Graphene asymmetric supercapacitors were fabricated in KOH aqueous electrolyte. $Ni(OH)_2$//Graphene asymmetric supercapacitor results in an areal capacitance of 253 mF/cm^2 at 5 mA/cm^2 which is higher than reported 185 mF/cm^2 at 5 mA/cm^2 for NiO//rGO asymmetric supercapacitor prepared by hydrothermal method. Ni-Co-OH/G-CNF//Graphene asymmetric supercapacitor results in a maximum power of 23 mW within 2.2 V which are higher than the maximum power and the operating voltage of our $Ni(OH)_2$//Graphene (15.94 mW within 1.8 V). Our asymmetric supercapacitors are featured by not only their enhanced electrochemical performance, but also by their flexible-electrodes, low-cost fabrication process and environmentally friendly materials.

ACNOWLEDGMENTS

This research was supported by King Abdullah University of Science and Technology (KAUST).

SUPPORTING INFORMATION

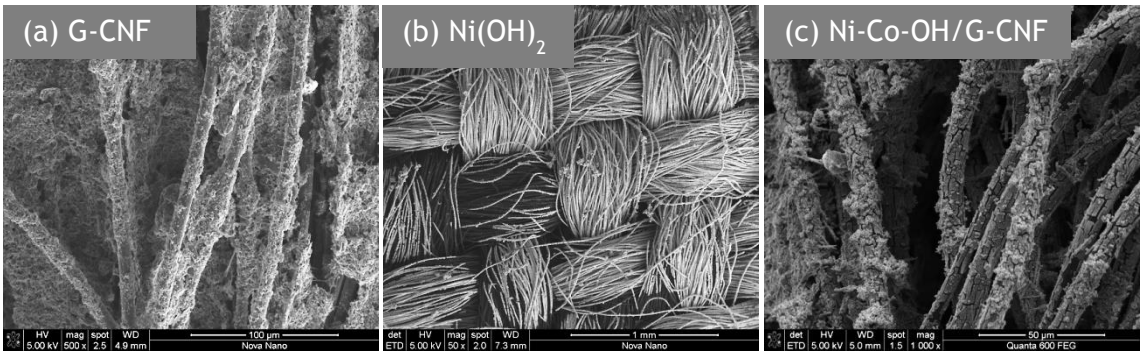

Figure 5.7 Low magnification SEM images of (a) Graphene and carbon nanofibers. (b) Nickel hydroxide. (c) Nickel-cobalt hydroxides on graphene and carbon nanofibers. All are coated on carbon microfibers substrates.

$$C = \frac{I\,\Delta t}{\Delta V} \qquad \textbf{Equation 5.1}$$

where C is capacitance [mF], I is applied constant current [mA], Δt is discharge time range [s], and ΔV is discharge potential range [V].

$$q = C\,\Delta V = I\,\Delta t \qquad \textbf{Equation 5.2}$$

where q is electrical charge [C].

$$\frac{1}{C_{cell}} = \frac{1}{C^{+}} + \frac{1}{C^{-}} \qquad \textbf{Equation 5.3}$$

where C^{+} and C^{-} are capacitances of positive and negative electrodes, respectively [mF].

$$E = \frac{1}{2} C \, \Delta V^2$$ Equation 5.4

$$P = \frac{E}{\Delta t}$$ Equation 5.5

where *E* is energy [mW.s] and *P* is power [mW].

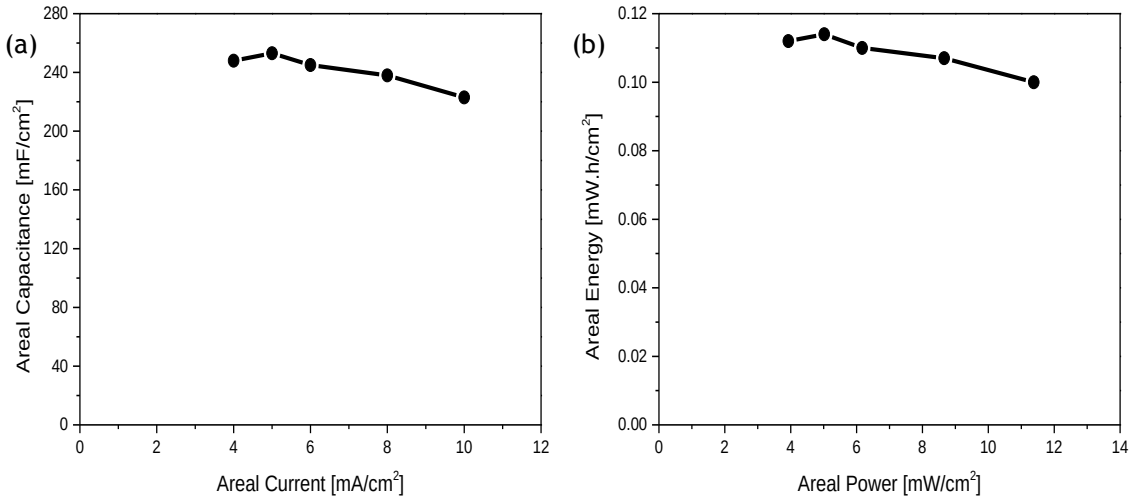

Figure 5.8 (a) Areal capacitance of $Ni(OH)_2$//Graphene asymmetric supercapacitor at different current values. (b) Areal energy and areal power of $Ni(OH)_2$//Graphene asymmetric supercapacitor.

Chapter 6 . ON-CHIP SUPERCAPACITORS USING NICKEL HYDROXIDE NANOFLAKES

N. Kurra*, Nuha A. Alhebshi* and H. N. Alshareef, *Microfabricated Pseudocapacitors Using $Ni(OH)_2$ Electrodes Exhibit Remarkable Volumetric Capacitance and Energy Density*. **Advanced Energy Materials**, 5, 1401303, doi: 10.1002/aenm.201401303 (2015) *Contributed equally

ABSTRACT

Metal hydroxide based microfabricated pseudocapacitors with impressive volumetric stack capacitance and energy density are demonstrated. A combination of top-down photolithographic process and bottom-up chemical synthesis is employed to fabricate the micro-pseudocapacitors (μ-pseudocapacitors). The resulting $Ni(OH)_2$-based devices show several excellent characteristics including high-rate redox activity up to 500 V s^{-1} and an areal cell capacitance of 16 mF cm^{-2} corresponding to a volumetric stack capacitance of 325 F cm^{-3}. This volumetric capacitance is two-fold higher than carbon and metal oxide based μ-supercapacitors with interdigitated electrode architecture. Furthermore, these μ-pseudocapacitors show a maximum energy density of 21 mWh cm^{-3}, which is superior to the Li-based thin film batteries. The heterogeneous growth of $Ni(OH)_2$ over the Ni surface during the chemical bath deposition is found to be the key parameter in the formation of uniform monolithic $Ni(OH)_2$ nanosheets with vertical orientation, responsible for the

remarkable properties of the fabricated devices. Additionally, functional tandem configurations of the μ-pseudocapacitors are shown to be capable of powering a light-emitting diode.

6.1. INTRODUCTION

The nanotechnology revolution has promoted technological advances with increasing levels of miniaturization of electronic, energy harvesting, and energy storage devices.[70,71] As an example, small scale energy storage devices are currently in high demand to power up microelectronic devices such as microelectromechanical systems (MEMS), microsensors and nanorobotics.[72,73] A planar configuration of the energy storage devices is essential to allow more robust integration of on-chip energy storage devices to power up microelectronic devices.[74,75] However, thin film based energy storage devices suffer from the poor power density due to limited diffusion of the ions in this architecture.[76,77] To circumvent the poor rate capabilities of thin-film based supercapacitors, the interdigitated electrode geometry is a better option because there is no separator in this case, allowing the fast movement of ions in the same plane.[74,78] These micro-supercapacitors (μ-SCs), which exhibit high power density when compared to microbatteries, and good frequency response, can be thought of replacement for the bulk Al-based electrolytic capacitors.[79,80]

Various fabrication techniques such as photolithography,[81] laser scribing,[82] ink jet printing,[83] micromolding[84] in combination with the other

deposition techniques such as electrochemical,[85] electrophoretic,[86] chemical vapor deposition,[87] sputtering techniques[88] have been employed in building the μ-SC devices. Carbon based μ-SCs have been fabricated by employing different forms of carbon materials such as carbide derived carbon, activated carbon, onion like carbon, carbon nanotubes, graphene, reduced graphene oxide.[81,83,86,87,89,90] As these carbon materials store the charge through the formation of electrochemical double layers (EDLs), they have exhibited lower values of areal capacitance in the range of 0.1-6 mF cm^{-2}.[86,87,89-91] In order to enhance the areal capacitance, several pseudocapacitive materials such as MnO_2,[88] RuO_2,[92] MoS_2[93] and even conducting polymers were electrodeposited over the current collectors.[94,95] Generally, due to fast reversible redox reactions or Faradaic charge transfer at the surface of electroactive species, pseudocapacitors exhibit much higher specific capacitance when compared to that of carbon-based materials. The geometric parameters such as the width, length and the spacing between the finger electrodes are important in arriving at the optimized values of capacitance and rate capability of a μ-SC.[96] $Ni(OH)_2$ has been the high capacity pseudocapacitve material with its well-defined redox electrochemistry, was employed as an electrode material for high energy density applications.[27,65,97] However, the electrochemical behavior of $Ni(OH)_2$ electrodes in the planar interdigitated configuration has not been studied yet. Hence, it is always interesting to study the redox behavior of the $Ni(OH)_2$ in the in-plane geometry in two-electrode configuration.

Here, we use a simple strategy for fabricating on-chip planar interdigitated electrodes with pseudocapacitive metal hydroxide coatings. Specifically, $Ni(OH)_2$ μ-SCs are fabricated by following the conventional photolithography protocol to deposit metal layers over the patterned photoresist with subsequent chemical synthesis of $Ni(OH)_2$. Different chemical synthesis methods and metallic nucleation layers were tested. The fabricated μ-pseudocapacitors show an areal cell capacitance of 16 mF cm^{-2} with a volumetric stack capacitance of 325 F cm^{-3} in 1 M KOH electrolyte. The high rate capability of these μ-pseudocapacitor devices are realized through the appearance of redox peaks even at higher scan rates of 500 V s^{-1} in a two-electrode configuration. Further, solid state and flexible $Ni(OH)_2$ micropseudocapacitors were fabricated employing polyvinyl alcohol (PVA)/KOH gel electrolyte. This solid-state device showed cycling stability up to 80% capacitance retention after 1000 cycles. The tandem configuration of these $Ni(OH)_2$ μ-pseudocapacitors was employed to demonstrate the glowing of a light-emitting diode (LED).

6.2. EXPERIMENTAL METHODS

6.2.1. Photolithography of Current Collector Substrates

Glass substrates (Fischer) were cut into 1 in × 1 in size, cleaned with a soap solution to remove the dirt, followed by ultrasonication in acetone, isopropyl alcohol, and deionized water sequentially for 5 min each, and then dried by blowing nitrogen. Plastic substrates based on PEN sheets were

employed to fabricate flexible solid-state μ-SCs. Photoresist AZ9260 was spun coated at 3000 rpm for 60 s over the glass or PEN substrates to get 10 μm thick photoresist layers. Photoresist coated substrates were soft baked at 110 °C for 3 min. The UV exposure was carried out using an EVG contact aligner at a constant dose of 1800 mJ cm^{-2} through the Cr/Glass mask having the interdigitated patterns. After exposure, samples were developed in AZ726 developer solution for 6 min, which resulted in the formation of patterns in the photoresist layer. Metal layers of 50 nm Ni/200 nm Pt/20 nm Ti were deposited by sputtering (Equiment Support Co., Cambridge, England) technique over the patterned photoresist layer. Before the lift-off process, the samples were immersed in the CBD bath containing precursor for the $Ni(OH)_2$ for 1–2 h. During the CBD process, $Ni(OH)_2$ nanoflakes were precipitated on the entire substrate uniformly. The lift-off was then performed in acetone to remove the unexposed photoresist layer along with the metal layers and $Ni(OH)_2$deposits present on it. This process resulted in the $Ni(OH)_2$ deposit over the interdigitated planar Ni/Pt/Ti electrodes. 30 fingers were used (15 electrodes for each polarity) with a typical width of each finger 100 μm, and spacing between the fingers of 50 μm; the total area of all the fingers was 0.15 cm^2.

6.2.2. Chemical Bath Deposition of $Ni(OH)_2$ Nanoflakes

After deposition of Ni/Pt/Ti metal layers on the patterned photoresist substrates, before the lift-off process, the substrates were dipped in a chemical bath containing a clear-green mixture of 5.26 g of nickel(II) sulfate

hexahydrate ($NiSO_4.6H_2O$) in 20 mL of deionized (DI) water (H_2O).[65] 1.6 mL of ammonium hydroxide solution (30–33% NH_3 in H_2O) was added drop by drop. Then, 1.35 g of potassium persulfate ($K_2S_2O_8$) in 33 mL of deionized (DI) water (H_2O) was added to the mixture with stirring for few seconds at room temperature. As the reactions progressed, the mixture became dense, and the color turned to dark blue. The solution was then kept without stirring at room temperature for 1–2 h. After the CBD process, the samples were washed with deionized water several times followed by drying at room temperature in a fume hood overnight. Electrodeposition of $Ni(OH)_2$ was performed in a standard three-electrode configuration with Ni/Pt/Ti/Glass as working electrode, Ag/AgCl as reference and Pt as counter electrodes, 0.1 M $NiSO_4$ + 0.5 M Na_2SO_4 as electrolyte at a constant potential of –0.9 V at room temperature for 15 min.

6.2.3. Materials Characterization

The structural aspects of the $Ni(OH)_2$ nanoflakes was analyzed using XRD. $Ni(OH)_2$ films were deposited over the plane Ni/Pt/Ti/Glass substrate in order to do thin film XRD. A D8 Advance System from Bruker Corporation, equipped with Cu Kα X-ray source (λ = 0.15406 nm) was used. Surface morphology and microstructure were imaged by SEM (Nova Nano 630 instrument, FEI Co., The Netherlands). Energy-dispersive spectroscopy (EDS) analysis was performed with an EDAX Genesis instrument (Mahwah, NJ) attached to the SEM column. The film thicknesses were measured using a Veeco Dektak 150 surface

profilometer. The bonding aspects of the $Ni(OH)_2$ nanoflakes were investigated using Raman spectroscopy (LabRAM ARAMIS, Horiba-Jobin Yvon). Raman spectra were acquired with notch filters cutting at 100 cm^{-1} using a He-Ne laser (633 nm, 5 mW at source) and a laser spot size of 1.5 μm.

6.2.4. Electrochemical Measurements

The electrochemical properties of $Ni(OH)_2$ μ-pseudocapacitors were investigated in a two-electrode configuration using an electrochemical workstation (CHI 660D, CH Instruments Incorporation). CV, galvanostatic CD, and electrochemical impedance spectroscopy (EIS) measurements were performed in 1 M KOH and PVA/KOH gel electrolytes. PVA/KOH gel electrolyte was prepared by mixing 1.2 g of KOH with 2 g of PVA in 20 mL of water followed by rigorous stirring at 85 °C until the formation of a clear gel. Solid-state devices were fabricated by dropping 10 μL of the gel electrolyte across the finger electrodes followed by drying at room temperature.

CV experiments were carried out at different scan rates selected from 10 mV s^{-1} to 500 V s^{-1} in a two-electrode configuration. CD experiments were performed at different current densities selected from 50 μA cm^{-2} to 250 μA cm^{-2}. The EIS was performed in the frequency range from 100 kHz to 0.1 Hz at open circuit potential by applying a small sinusoidal potential of 10 mV signal. Electrochemical cycling stability was measured using VMP3 multichannel electrochemical workstation (Bio-Logic). All measurements were carried out at room temperature.

6.3. RESULTS AND DISCUSSIONS

6.3.1. Materials Properties

The 3D schematic illustration for the fabrication process of our μ-SC is shown in **Figure 6.1**. The protocol involves a conventional photolithography process to fabricate the planar interdigitated finger electrodes over a glass or a plastic substrate. Initially, photoresist was spun coated on a glass slide as shown in **Figure 6.1 (a)**, which was then UV exposed through a Cr mask followed by developing to obtain the interdigitated patterns on the photoresist as shown in **Figure 6.1 (b)**. Our strategy was to deposit the metal layers followed by chemical deposition of $Ni(OH)_2$ before the lift-off process. Since Au was the most commonly used current collector in fabricating microsupercapacitors,[88,92,94,96] initially a Au/Ti bilayer was used to deposit $Ni(OH)_2$ by CBD process. However, it was found that the growth of $Ni(OH)_2$ over the Au current collector is non-uniform and grows in the form of domain-like structures (see Supporting Information, **Figure 6.7 (a)**). These domain-like structures of $Ni(OH)_2$ exhibited poor adhesion and peeled off during electrochemical measurements, presenting a serious challenge in fabricating $Ni(OH)_2$ μ-SCs over Au current collectors. The uniform growth of $Ni(OH)_2$ over the current collector is essential in order to achieve reliable and stable electrochemical performance. It was anticipated that Ni surface due to its chemical compatibility may aid in the heterogeneous growth of $Ni(OH)_2$ film at the expense of preventing the aggregation of Ni^{+2} species at the interface of

solution/Ni surface. Indeed, it was observed that the growth of $Ni(OH)_2$ over the Ni surface was uniform (see Supporting Information, **Figure 6.7 (b)**). It appears that the homogeneous growth is dominating over the heterogenous film growth in the case of Au surface, leading to the formation of aggregated $Ni(OH)_2$ domain structures (see schematic in **Figure 6.7**, Supporting Information). It can be anticipated that the surface energy and the interfacial strain across the metal/$Ni(OH)_2$ interface have the strong influence on the uniform growth of $Ni(OH)_2$ during the chemical bath deposition (CBD) process.

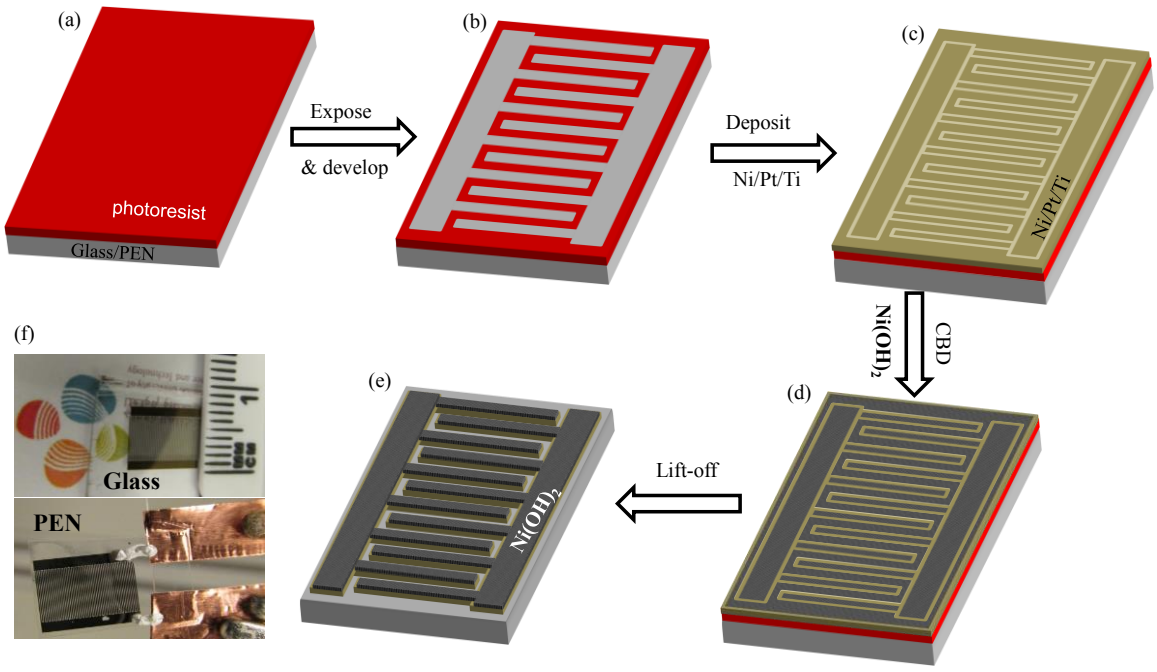

Figure 6.1 Fabrication of $Ni(OH)_2$ μ-pseudocapacitor devices. (a)-(c) Schematic illustration of the conventional photolithography process up to the metal layer deposition. (d) CBD of $Ni(OH)_2$ over the entire chip before the lift-off process. (e) Lift-off using acetone after the CBD process. (f) Photographs showing the $Ni(OH)_2$ μ-pseudocapacitor devices fabricated on glass and PEN substrates.

CBD is a bottom-up approach in which supersaturated solution gets precipitated as a solid phase over a given substrate. This method involves with

various distinct steps such as nucleation, coalescence and subsequent growth by aggregation of the particles.[98] Hence, the uniform growth of $Ni(OH)_2$ is expected when there is a homogeneous formation of nucleation centers, which happens through the rapid decomposition of clusters of metal precursor molecules (in this case, $Ni(OH)_2$). These nucleation centers aid in the further growth of the film through coalesce and aggregation of species. The important step here is the formation of homogenous nucleation centers which is guided by the surface energy of the substrate material besides the other parameters (bath composition, temperature, etc.). During the growth process, the nanosheets of $Ni(OH)_2$ get corrugated together in order to lower the surface energy, leading to the uniform and monolithic formation of $Ni(OH)_2$ deposit.[66,98] In our case, we found that Au surface is not assisting the homogeneous formation of nucleation centers, resulting in the growth of $Ni(OH)_2$ domains. It can be anticipated that other than Ni, stainless steel and graphitic substrates may be expected to work the same as Ni.[65,98] However, chemical bath composition and temperature conditions may be optimized for controlling the growth of $Ni(OH)_2$films over the other substrates.[99]

It was observed that while doing electrochemical measurements, $Ni(OH)_2$/Ni electrodes were getting delaminated in 1 M KOH electrolyte (see inset of **Figure 6.7 (b)**, Supporting Information). Hence, we have devised a metal tri-stack consisting of a thin layer of Ni (50 nm) deposited over the Pt/Ti metal fingers. The thin layer of Ni increases the rate of heterogeneous film growth over the homogeneous aggregation of particles resulting in uniform

growth of $Ni(OH)_2$ during the CBD process, while the bottom Pt/Ti current collector was found to be quite stable in 1 M KOH electrolyte. Thus, the metal layers (Ni/Pt/Ti) deposited over the patterned photoresist layer by sputter deposition, as shown in **Figure 6.1 (c)**, used for all of the μ-pseudocapacitors fabiated in this study. We found that the Ti layer was essential to provide strong adhesion between the Ni/Pt film and the glass or plastic substrates, and hence delamination of metal films could be avoided. On the other hand, the thin layer of Ni (thickness, 50 nm) can promote the uniform nucleation and growth of $Ni(OH)_2$ nanosheets during the CBD process. Finally, Pt, which is inert, plays the role of current collector. Before the lift-off process, the metal-coated, patterned photoresist substrate was dipped in a chemical bath containing the nickel hydroxide precursor for 1–2 h at room temperature in order to precipitate the $Ni(OH)_2$ nanoflakes over the entire surface as shown in **Figure 6.1 (d)**. This sample was then washed with deionized water to remove the unreacted initial precursor moieties followed by drying in a fume hood at room temperature. Next, the lift-off process was carried out in acetone to remove the $Ni(OH)_2$ and metal layers present on the unexposed regions of the photoresist layer (**Figure 6.1 (e)**). The final outcome of the above microfabrication process is the formation of planar interdigitated $Ni(OH)_2$ nanoflakes over the Ni/Pt/Ti current collectors. As the final step in the process is the lift-off after the CBD process of $Ni(OH)_2$, which results in clean interdigitated finger electrodes without any pseudocapacitive material in the interspaces of the electrode patterns. $Ni(OH)_2$ based micropseudocapacitors

fabricated over the glass and plastic PEN substrates are shown in **Figure 6.1 (f)**.

Figure 6.2 (a) shows a scanning electron microscopy (SEM) image illustrating the uniform growth of $Ni(OH)_2$ in a clean interdigitated pattern, without having any deposits in between the fingers. The morphology of the $Ni(OH)_2$ consists of vertically grown nanoflakes in the monolithic form with a typical thickness of 500 nm, as shown in **Figure 6.2 (b) and (c)**. The X-ray diffraction (XRD) pattern in **Figure 6.2 (d)** shows that nickel hydroxide grown by CBD has mixed phases of α-$Ni(OH)_2$ (JCPDS 00-038-0715) and $4Ni(OH)_2$-NiOOH (JCPDS 00-006-0044). The XRD pattern also shows Ni (JCPDS 00-004-0850) and Pt (JCPDS 00-044-1294) peaks from the current collector. Nickel hydroxide was predicted to have polycrystalline nature based on the fact that the $Ni(OH)_2$-phase can be oxidized to the NiOOH-phase by persulfate, as indicated in the following molecular level heterogeneous reaction:[42,100]

$$2Ni(OH)_2 + S_2O_8^{2-} \rightarrow 2NiOOH + 2SO_4^{2-} + 2H^+ \qquad \textbf{Equation 6.1}$$

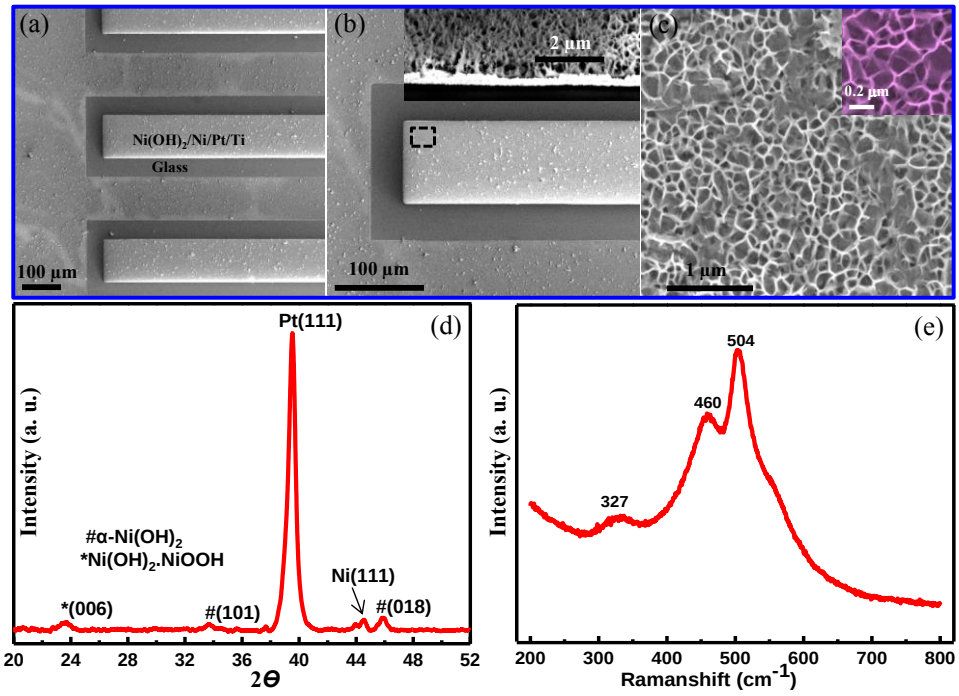

Figure 6.2 (a) and (b) SEM images showing the $Ni(OH)_2$ finger electrodes. The inset shows the tilt view of the CBD of $Ni(OH)_2$. (c) Zoom-in image shows the uniform vertical growth of nanoflakes of $Ni(OH)_2$ over the Ni/Pt/Ti current collectors, inset shows the interconnected vertically grown $Ni(OH)_2$ nanosheets. (d) XRD pattern and (e) Raman spectrum of $Ni(OH)_2$ grown by CBD.

Raman spectrum was recorded to confirm the bonding aspects of $Ni(OH)_2$ nanofalkes as shown in **Figure 6.2 (e)**. The 460 cm^{-1} band can be attributed to the Ni-O(H) stretching mode, while the bands at 327 and 504 cm^{-1} can be assigned to $E_u(T)$ and $A_{2u}(T)$ lattice vibrations of $Ni(OH)_2$.[101]

6.3.2. Electrochemical Performance

$Ni(OH)_2$ interdigitated finger electrodes were investigated in 1 M KOH electrolyte in a two-electrode configuration. The cyclic voltammetry (CV) curves at different scan rates are shown in **Figure 6.3**. At low scan rate of 10 mV s^{-1}, the voltammogram exhibits the currents, which are due to oxygen

evolution and redox reactions of $Ni(OH)_2$, as indicated in **Figure 6.3 (a)**. The redox peaks at 89 mV and -6 mV correspond to the oxidation and reduction of the $Ni(OH)_2$, respectively as shown in **Figure 6.3 (a)**. The sudden hike in the current above the anodic potential of 0.4 V can be attributed to the evolution of oxygen gas according to the following reaction:

$$4OH^- \rightarrow O_2 + 2H_2O + 4e^- \qquad \textbf{Equation 6.2}$$

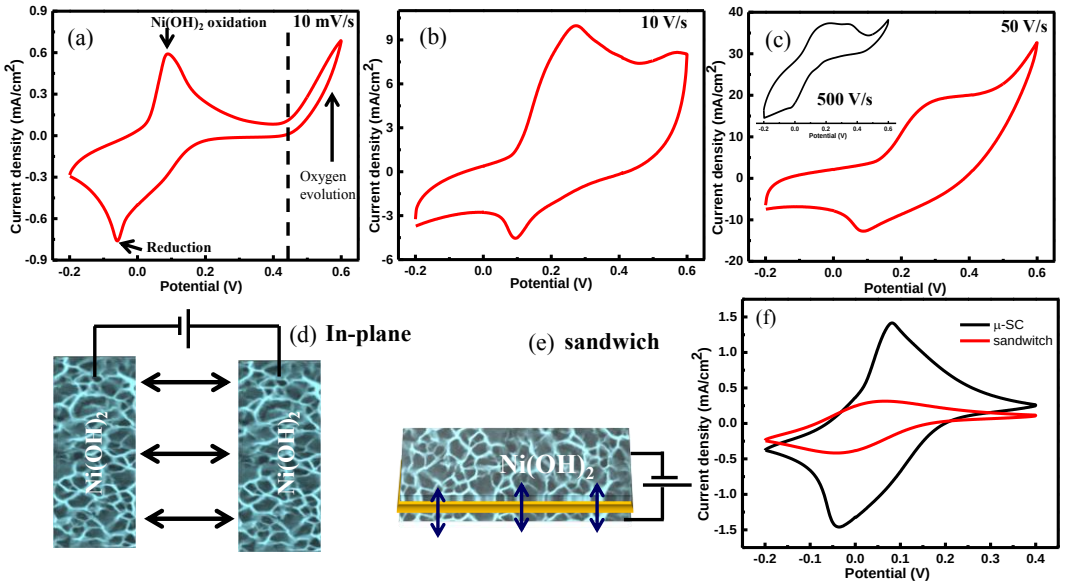

Figure 6.3 (a)-(c) Cyclic voltammograms of CBD $Ni(OH)_2$ finger electrodes at different scan rates in a two-electrode configuration in 1 M KOH electrolyte. The inset shows CV data collected at higher scan rate of 500 V s^{-1}. Schematic illustrating the d) in-plane and (e) sandwich configuration of the $Ni(OH)_2$ electrodes. (f) Comparison of CV data for planar vs sandwich configurations of a $Ni(OH)_2$ pseudosupercapacitor device at 40 mV s^{-1}.

The CV curves display the redox peaks of $Ni(OH)_2$ even at higher scan rates of 10 and 50 V s^{-1} in a two-electrode configuration as shown in **Figure 6.3 (b) and (c)**, indicating the high rate capability of the $Ni(OH)_2$ μ-pseudocapacitor. The observation of high rate redox active behavior can be

attributed to the in-plane configuration of the interdigitated finger electrodes. As there is no separator involved in this design, the fast movement of the electrolyte ions in this planar configuration is responsible for the observation of the redox peaks at higher scan rates up to 500 V s^{-1}, which is otherwise impossible in a conventional sandwich configuration (see **Figure 6.3 (d) and (e)**). The CV curves of planar versus sandwich configuration of $Ni(OH)_2$ pseudocapacitor devices are shown in **Figure 6.3 (f)**. The current values are almost three times higher for the interdigitated planar $Ni(OH)_2$ pseudocapacitor when compared to the sandwich configuration. The redox behavior of $Ni(OH)_2$ was suppressed at a scan rate of 500 mV s^{-1} in the sandwich configuration, which is due to diffusion limitations in this configuration (see Supporting Information, **Figure 6.8**). Due to diffusion limited problems of electrolyte ions at higher scan rates, it was not possible to capture the redox activity of the $Ni(OH)_2$ in the sandwich configuration. In order to avoid the problems associated with the oxygen evolution at higher anodic potentials (above 0.4 V), the potential was limited up to 0.4 V to capture the redox activity of the $Ni(OH)_2$ only.

The typical CV curves of $Ni(OH)_2$ μ-pseudocapacitor in 1 M KOH electrolyte at different scan rates in the potential window of –0.2 to 0.4 V are displayed in **Figure 6.4 (a)-(d).** Two strong redox peaks are observed at a lower scan rate of 10 mV s^{-1}; these are due to reversible formation of Ni^{+2}/Ni^{+3} redox couple in a basic medium as shown in **Equation 6.3**. The oxidation of Ni^{+2} to Ni^{+3} due to extraction of proton from the $Ni(OH)_2$in alkaline medium is seen as

the oxidation peak marked in **Figure 6.4 (a)**. The reverse process happens during the reduction reaction: :[102,103]

$$Ni(OH)_2 + OH^- \leftrightarrow NiOOH + H_2O + e^- \qquad \textbf{Equation 6.3}$$

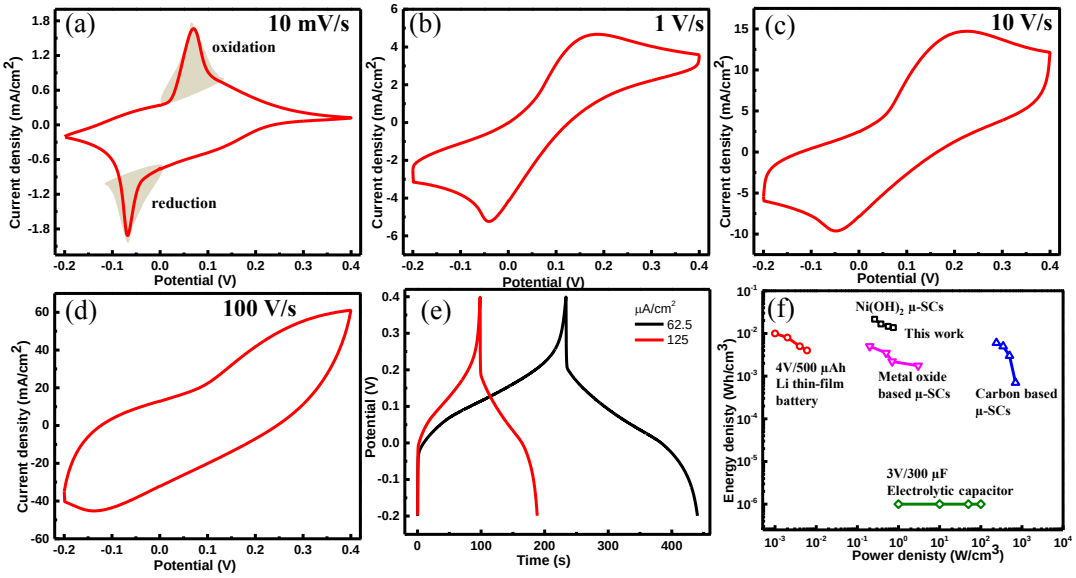

Figure 6.4 (a)-(d) Cyclic voltammograms of a $Ni(OH)_2$ µ-pseudocapacitor at different scan rates in 1 M KOH electrolyte. (e) Charge-discharge curves at different current densities. (f) Ragone plot showing the comparison of energy and power density of Li thin-film batteries, electrolytic capacitors, carbon and metal oxide based µ-SCs with respect to $Ni(OH)_2$ µ-pseudocapacitor.

Even at higher scan rates of 1 V s^{-1} and 10 V s^{-1}, the redox peaks are still observed, indicating the fast redox reactions of $Ni(OH)_2$ in this planar interdigitated architecture as shown in **Figure 6.4 (b) and (c)**. The high rate redox activity of the $Ni(OH)_2$ µ-pseudocapacitors with high rate Faradaic reactions contributing to the higher values of pseudocapacitance. The charge-discharge curves are seen typical of $Ni(OH)_2$ at current densities of 62.5 and 125 µA cm^{-2} are shown in **Figure 6.4 (e)**. The areal cell capacitance was

calculated from the discharge curve and found to be 16 mF cm^{-2}, which is at least two times higher when compared to carbon-based interdigitated microsupercapacitors (0.1–6 mF cm^{-2})[81-83,89-91,104] The bare Ni/Pt/Ti electrodes, without having the $Ni(OH)_2$ deposit, have exhibited areal cell capacitance of 15–20 μF cm^{-2} in 1 M KOH electrolyte (see Figure S3, Supporting Information). It is clear that Ni has a negligible contribution towards the cell capacitance shown by $Ni(OH)_2$. CV data and charge–discharge (CD) for a 1 h CBD $Ni(OH)_2$ μ-pseudocapacitor are shown in the Supporting Information, **Figure 6.10**. Pseudocapacitive materials such as MnO_2, RuO_2 and MoS_2 have exhibited an areal capacitance in the range of 1–10 mF cm^{-2}.[88,92,94] Similarly, the electrodeposited $Ni(OH)_2$ exhibited an areal capacitance of 1.5 mF cm^{-2}, signifying that the CBD process is the better option in the fabrication of $Ni(OH)_2$ based μ-pseudocapacitors with remarkable performance under the fabrication conditions adapted in this study (see **Figure 6.11**, Supporting Information). This is because CBD is an easily scalable process and is very cost-effective, especially if done at room temperature as we have done in our study. Wang and co-workers have demonstrated the effect of electrodeposition temperature on the electrochemical performance of $Ni(OH)_2$ over Ni foam substrate.[105] Similarly, the processing conditions such as bath composition, temperature and nucleation layers can be optimized to arrive at the enhanced electrochemical performance of the $Ni(OH)_2$ μ-pseudocapacitors by the electrodeposition method. Volumetric stack capacitance of the device was calculated by considering the total volume of the device and found to be 325 F

cm^{-3}, which is high compared to the various μ-supercapacitor devices reported in the literature and superior to carbon based μ-supercapacitors (180 F cm^{-3}).[81-83,86,87,89,90] The Ragone plot for the $Ni(OH)_2$ μ-pseudocapacitors at different current densities is shown in **Figure 6.4 (f)**. The device exhibits a maximum energy density of 21 mWh cm^{-3} at a power density of 262.5 mW cm^{-3}. This energy density of the $Ni(OH)_2$ μ-pseudocapacitor is superior to the Li based thin-film batteries (10 mWh cm^{-3}), μ-SCs based on carbon materials (*E* = 0.15–9 mWh cm^{-3}) and metal oxide materials (1–5 mWh cm^{-3}).[88,106] Due to high rate capability of the $Ni(OH)_2$ μ-pseudocapacitor, it can deliver a maximum power density of 750 mW cm^{-3} at an energy density of 14 mWh cm^{-3}. This clearly signifies that the importance of the interdigitated architecture of the electrodes with suitable pseudocapacitive coatings, such as $Ni(OH)_2$, can have energy densities that are superior to those of Li-based thin-film batteries.

The flexible nature of the $Ni(OH)_2$ μ-SC devices was investigated by employing the polyvinyl alcohol (PVA)/KOH gel electrolyte. These devices were fabricated on a flexible polyethylene naphthalate (PEN) sheet following the photolithography and CBD process. A small amount of the PVA/KOH gel electrolyte was applied across the finger electrodes followed by drying under ambient conditions. CV curves exhibit redox peaks up to scan rate of 2 V s^{-1}, indicating the fast redox behavior of $Ni(OH)_2$ even with the gel electrolyte as shown in **Figure 6.5 (a)**. At higher scan rates, CVs exhibit rectangular behavior as the rate of the redox reaction may not be compatible with the diffusion rate of electrolyte ions present in the polymer matrix as shown in **Figure 6.5 (b)**.

Furthermore, it can be seen from **Figure 6.5 (c)** that the CV curves under the bent configuration remain the same as that of the normal device. The inset shows a photograph of the bent $Ni(OH)_2$ μ-pseudocapacitor device. The charge-discharge curves show the typical pseudocapacitive nature of $Ni(OH)_2$, as illustrated by a strong deviation from the triangular nature of EDLs (see **Figure 6.5 (d)**). This solid state device showed an areal cell capacitance of 2 mF cm^{-2} at a current density of 12 μA cm^{-2}, comparable to the $Ni(OH)_2$/graphene based thin film solid state devices.[103] **Figure 6.5 (e)** shows a Nyquist plot of the $Ni(OH)_2$ μ-SC, which exhibits a semicircle in the high frequency region with charge-transfer resistance of 2.6 kΩ . The insulating nature of the $Ni(OH)_2$ deposit can be the major factor for this large value of charge transfer resistance. The electrochemical cycling stability of the solid-state device was tested for 1000 cycles, demonstrating capacitance retention up to 80%, as shown in **Figure 6.5 (f)**.

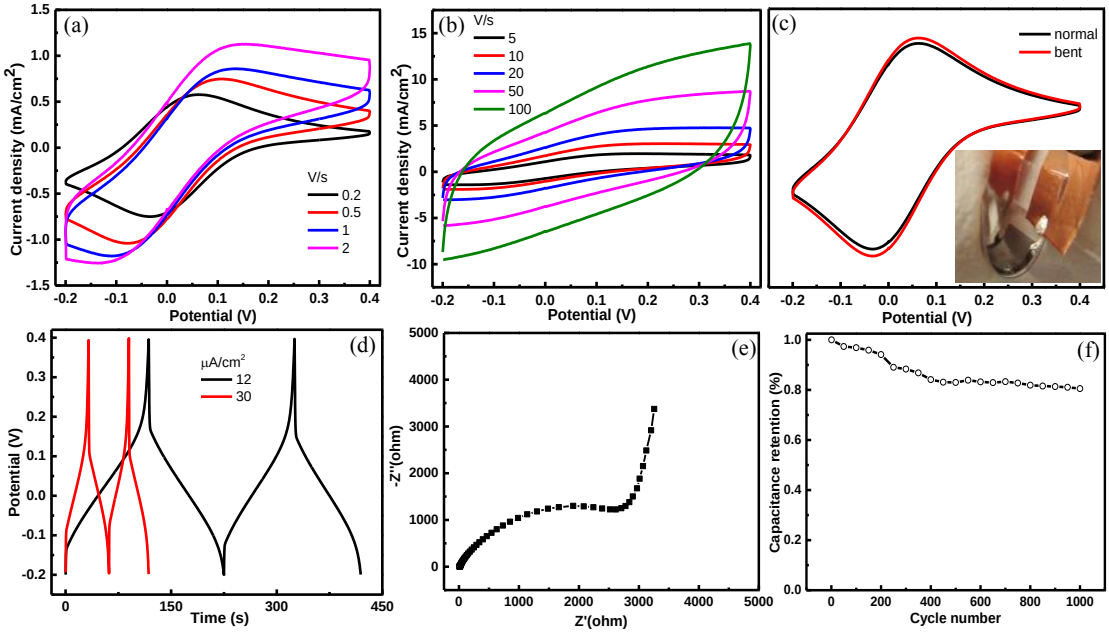

Figure 6.5 Solid state flexible $Ni(OH)_2$ pseudocapacitor. (a) and (b) CVs of the solid state device with PVA/KOH gel electrolyte at different scan rates. (c) CV scan of the device under normal and bent conditions at scan rate of 200 mV s^{-1}, The inset shows a photograph of the bent $Ni(OH)_2$ pseudocapacitor device. (d) Charge–discharge curves at current densities of 12 and 30 μA cm^{-2}. (e) Nyquist plot of the solid state device. (f) Electrochemical cycling stability of the device over 1000 cycles.

As these μ-SC devices can deliver less power; they may not be suitable for practical applications. However, tandem configuration of these devices may fetch extended voltage window or current based on the series and parallel combinations, respectively. Here, we demonstrate the tandem configuration of the $Ni(OH)_2$ μ-SCs in both series and parallel combinations. The potential window has been extended up to 0.8 V when two cells are connected in a series manner at the expense of reduction in the current values as shown in **Figure 6.6 (a) and (b)**. There is a shift and the broadness of the redox peaks was observed for the two cells connected in series compared to the single cell with relatively sharp redox peaks. Similarly, charge–discharge curves of the

series-connected devices showed less time for the discharge as compared to the single cell device as shown in **Figure 6.6 (c)**. In contrast, for the parallel combination of the μ-SC cells, the discharge time was found to be higher when compared to the single cell as expected (shown in **Figure 6.6 (d)**). Hence, the series and parallel combination of these $Ni(OH)_2$ μ-pseudocapacitors was used to extend the potential and current values, which can be harnessed in an external circuit to light an LED. The inset in **Figure 6.6 (d)** shows the glowing red LED powered from the tandem configuration of these $Ni(OH)_2$ based μ-pseudocapacitors for almost 45 s after charging for 20 s.

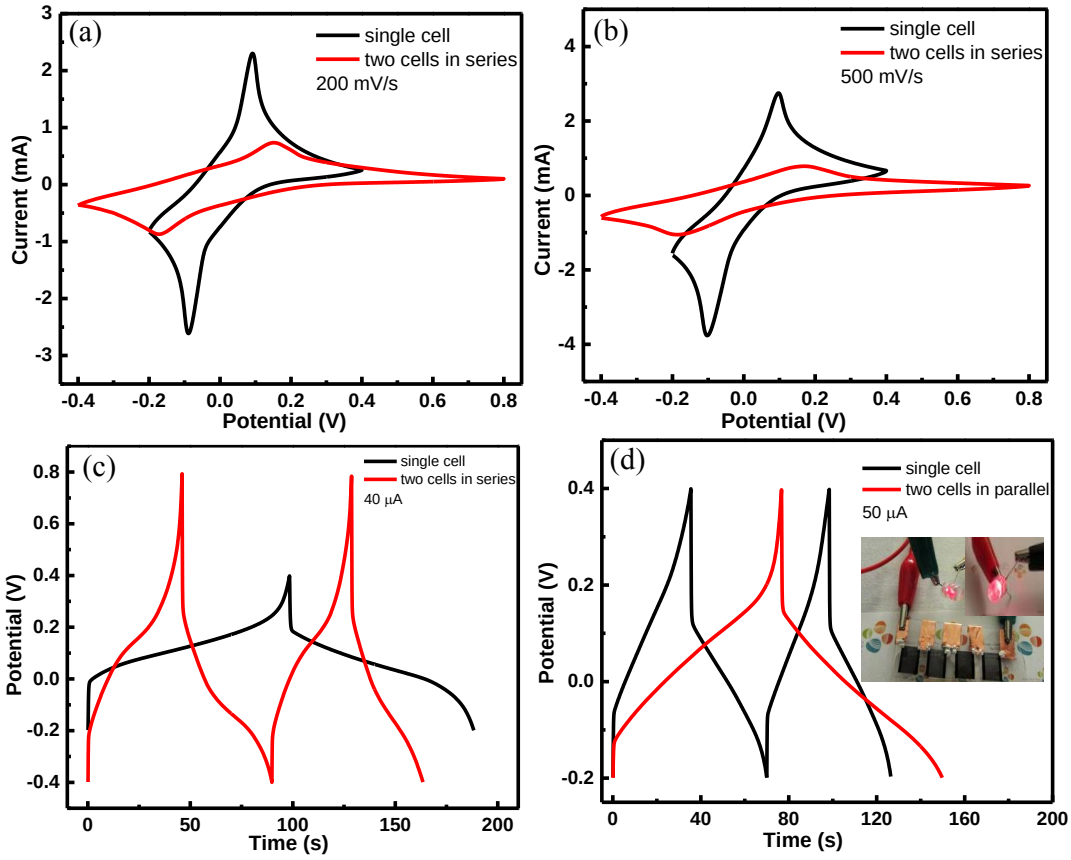

Figure 6.6 (a) and (b) CVs of the series connected $Ni(OH)_2$ μ-pseudocapacitor at different scan rates. Charge–discharge curves of the tandem configuration of $Ni(OH)_2$ μ-pseudocapacitor in (c) series and (d) parallel combinations. The inset shows the red LED powered using a tandem configuration of the $Ni(OH)_2$ μ-pseudocapacitor devices.

It is noteworthy that contributions from both the geometry and the material are important to achieve the better performance of the μ-SCs. The capacitance of a microsupercapacitor is directly proportional to the ratio of the width (w) to the finger spacing (s), i.e., w/s.[96] As the width of the finger increases, capacitance increases whereas the power density can be increased by reducing the spacing between the fingers. Hence, the high scan rate ability is associated with the high power density and high cell capacitance (high energy density), and can be controlled through the geometric parameters of

the device. In our case, the width of the each finger is 100 μm while the spacing between the fingers is 50 μm. That means the *w*/*s* ratio is 2, and we were able to achieve high scan rates up to 500 V s^{-1}. The RC time constant of the device depends on the geometric parameters such as w/s, responsible for achieving the high scan rate ability of the μ-SC devices. Lower the value of RC time constant higher the scan rate ability. For our $Ni(OH)_2$ micro-pseudocapacitors, we have found that RC time constant is in the range of 430 μs; $\tau = RC$ = 0.027 Ω cm^2 × 16 mF cm^{-2} = 432 μs, where *R* is the equivalent series resistance (ESR), obtained from the high frequency region of the Nyquist plot and *C* is the cell capacitance of the device. Recently, Dinh *et al.*, have made similar observations with the demonstration of high scan rate ability of the microsuercapacitors based on CNTs and RuO_2.[92] The experimental data was supported by the simulations involving computation of RC time constants with respect to the interspacing between the fingers. [92] Reduced spacing between the fingers will give rise to lower values of ESR, which in turn result in the higher power density with high cell capacitance and then high scan rate capability. However, depositing pseudocapactive materials over the finger electrodes while reducing the spacing between the fingers without shorting the positive and negative electrodes is a challenging aspect.

$Ni(OH)_2$ has been the active transition metal hydroxide material with its well-defined redox electrochemistry and high specific capacitance, and became an attractive candidate material in commercial alkaline batteries and also as a pseudocapacitor electrode material for high energy denisty

applications.[27,65,97] From our study, it is clear that $Ni(OH)_2$ has been proven to exhibit high performance when patterned in the form of interdigitated finger electrodes to realize the successful fabrication of μ-pseudocapacitor devices.

Thus, the materials such as carbonaceous materials with high porosity and high conductivity needed to be grown thicker to have higher total surface area for achieving large capacitance values. As the metal oxides/hydroxides are poorly conducting, optimal thickness is required to maintain higher values of energy density and power density. Width/spacing (*w*/*s*) ratio of the electrodes should be high for the higher values of cell capacitance and also short migration distance of ions for the fast charge/discharge rates.[96]

6.4. CONCLUSIONS

High rate redox, solid state, and flexible micropseudocapacitors were fabricated using conventional lithography and CBD. The $Ni(OH)_2$-based μ-pseudocapacitors showed high rate redox activity up to 500 V s^{-1}, with an area cell capacitance of 16 mF cm^{-2} and a volumetric stack capacitance of 325 F cm^{-3}, which is superior to carbon and metal oxide based μSCs. These μSCs showed a maximum energy density of 21 mWh cm^{-3}, which is superior to the Li-based thin film batteries. These remarkable characteristics of the $Ni(OH)_2$ μ-pseudocapacitors can be attributed to the uniform monolithic heterogenous growth of $Ni(OH)_2$ over the Ni surface during the chemical bath deposition. Tandem configuration of these $Ni(OH)_2$ based micropseudocapacitors was employed to demonstrate the lighting of an LED.

ACKNOWLEDGEMENTS

Narendra Kurra and Nuha A. Alhebshi contributed equally to this work. Research reported in this publication was supported by King Abdullah University of Science and Technology (KAUST), and by King Abdulaziz City for Science and Technology (KACST) under project number T-K-11-286. The authors also thank Muhammad Shahid for useful discussions, and the Advanced Nanofabrication, Imaging and Characterization Laboratory at KAUST for their excellent support. N.K. acknowledges the support from SABIC Postdoctoral Fellowship.

SUPPORTING INFORMATION

Areal cell capacitance (C_{cell}):

$$\boldsymbol{C_{cell} = \frac{i.\Delta t}{A_t.\Delta V}} \qquad \textbf{Equation 6.4}$$

Volumetric stack capacitance (C_{vol}):

$$\boldsymbol{C_{vol} = \frac{i.\Delta t}{v_t.\Delta V}} \qquad \textbf{Equation 6.5}$$

Volumetric Energy (E):

$$\boldsymbol{E = \frac{1}{2} C_{vol}\, V^2} \qquad \textbf{Equation 6.6}$$

Volumetric Power (P):

$$\boldsymbol{P = \frac{E}{\Delta t}} \qquad \textbf{Equation 6.7}$$

where i is the discharge current density, A_t is the total area of the all finger electrodes in cm^2, C_{cell} is the cell capacitance, C_{vol} is the volumetric stack capacitance, v_t is the volume of the all finger electrodes, ΔV is the potential window, Δt is the discharge time.

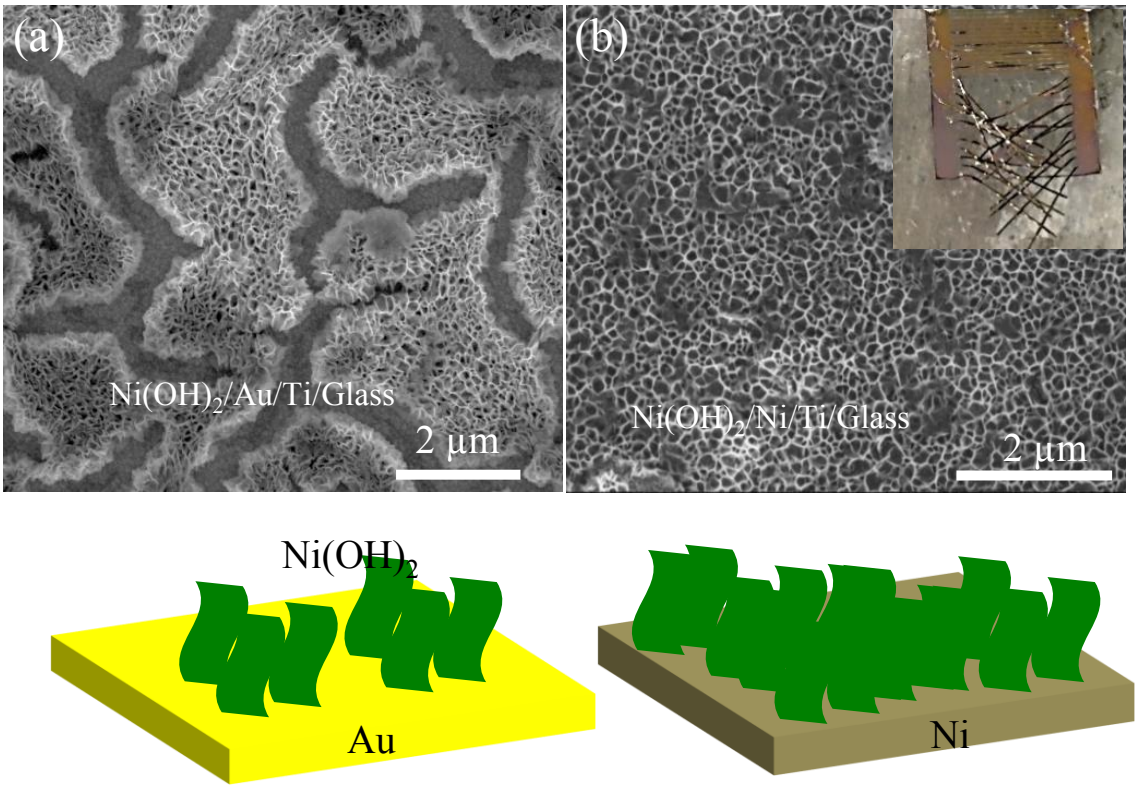

Figure 6.7 (a) Domain kind of growth of $Ni(OH)_2$ over the Au/Ti/Glass surface. (b) Uniform growth of $Ni(OH)_2$ over the Ni/Ti/Glass surface. Inset shows the delamination of Ni finger electrodes during the electrochemical measurements in 1M KOH electrolyte. By using the tristakc (Ni/Pt/Ti) both uniform and well-adhering $N(OH)_2$ nanosheets were observed, as shown in main mansucrip. The schematic shows the difference in the nucleation process of $Ni(OH)_2$ over the Au and Ni surfaces, respectively during the CBD process.

However, in our case, we have observed that the growth of $Ni(OH)_2$ over the Au current collector is non-uniform and seem to grow in the form of domain-like structures (see Supporting information, **Figure 6.7 (a)**). The

growth of $Ni(OH)_2$ was seen uniform and monolithic over the Ni surface (see **Figure 6.7 (b)**), but these fingers were getting delaminated while doing electrochemical measurements in 1M KOH electrolyte. Hence, we have chosen a thin layer of Ni (thickness, 50 nm) over the Pt/Ti metal fingers. As the top Ni surface helps in the uniform growth of $Ni(OH)_2$ during the CBD process while the bottom Pt/Ti current collector was found to be quite stable in 1M KOH electrolyte.

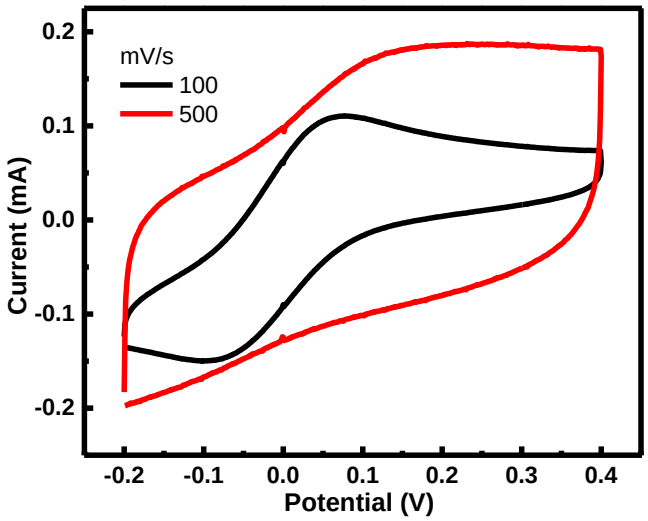

Figure 6.8 CVs of $Ni(OH)_2$ thin film supercapacitor in sandwich geometry at scan rates of 100 and 500 mV/s. At higher scan rate of 500 mV/s, the redox peaks are not prominent in this sandwich geometry while in planar interdigitated configuration, redox behavior is seen even at a scan rate of 500 V/s.

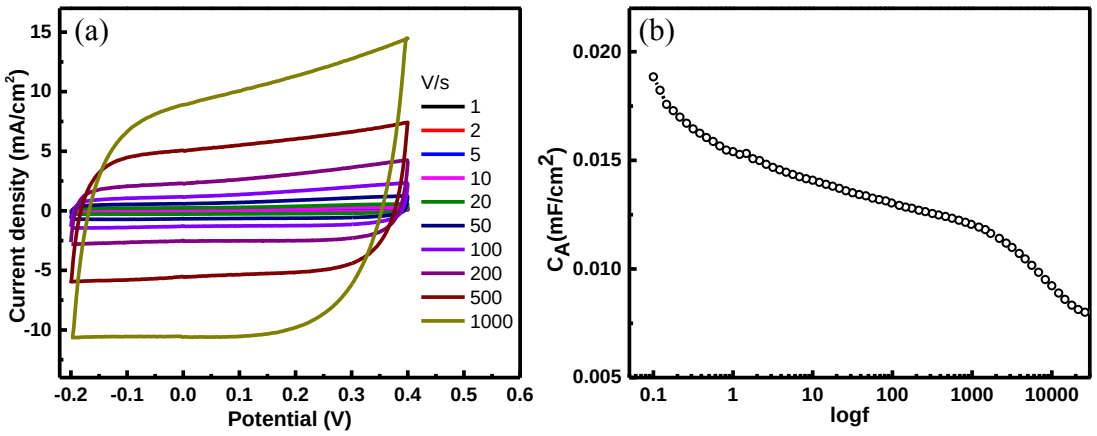

Figure 6.9 (a) CVs of bare Ni/Pt/Ti/glass interdigitated finger electrodes in 1M KOH electrolyte. (b) Areal cell capacitance with frequency of Ni/Pt/Ti μ-SC.

Bare Ni/Pt/Ti/glass electrodes exhibit an areal capacitance of 15-20 μF/cm^2 in 1M KOH electrolyte.

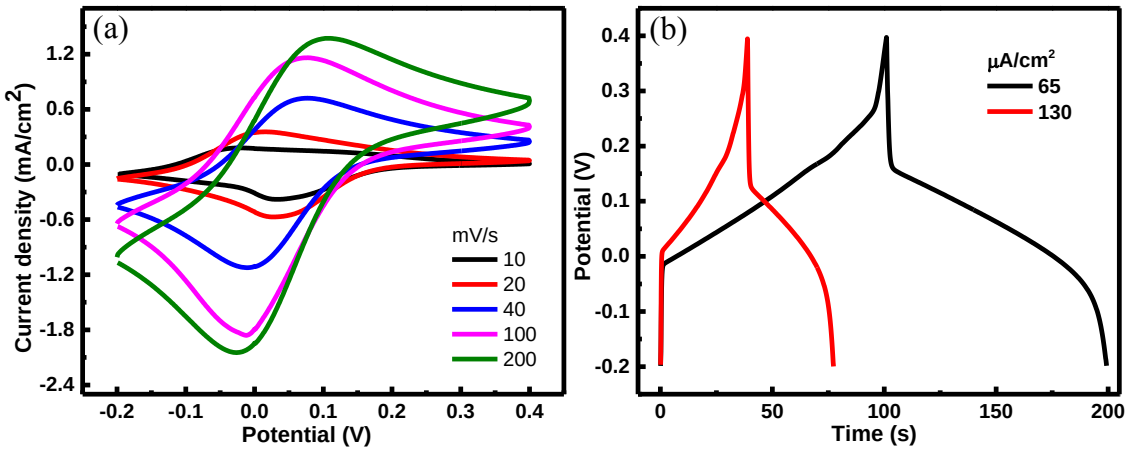

Figure 6.10 (a) CV and (b) CD curves for the 1hr CBD $Ni(OH)_2$ micropseudocapacitor.

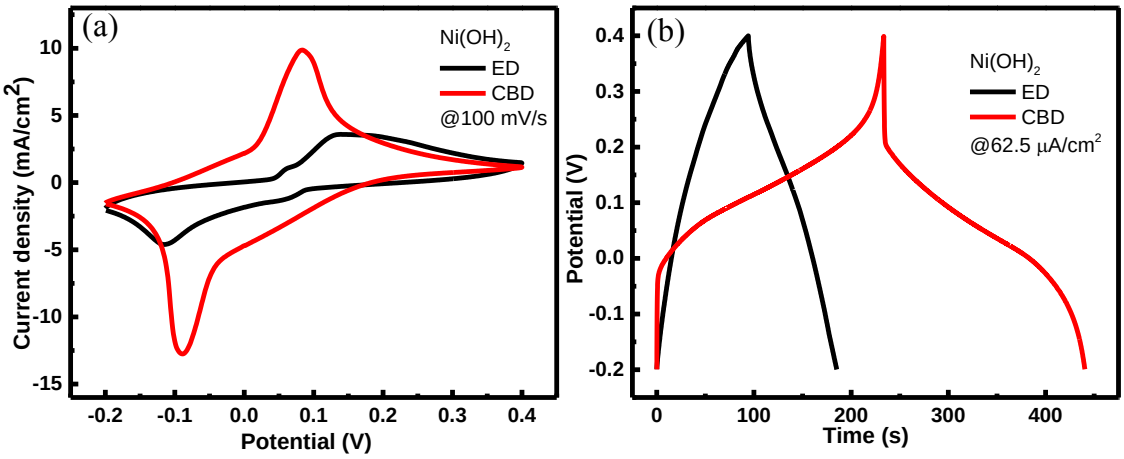

Figure 6.11 Comparison of (a) CV and (b) CD curves of CBD vs. electrodeposited $Ni(OH)_2$ micropseudocapacitors.

The electrodeposited $Ni(OH)_2$ micropseduocapacitors showed almost an order of magnitude less energy denisty compared to CBD process. However, the optimisation process for the electrodeposition may be required in order to achieve the better performance of the micropseudocapacior devices based on $Ni(OH)_2$.

SUMMARY

In this dissertation, we have studied and developed Ni-based electrode materials and devices for capacitive energy storage for both conventional and on-chip energy storage applications. The specific objectives of this research were to fabricate Ni-based electrochemical supercapacitors with high capacitance, wide operating voltage, good stability, and low cost. In addition, we wanted to study the basic aspects of the electrochemical behavior of Ni-based electrodes and devices. The main results of this work can be summarized in the following points:

- A uniform and conformal coating of nanostructured $Ni(OH)_2$ flakes on carbon microfibers has been deposited *in-situ* by a simple chemical bath deposition (CBD) at room temperature.

- The microfibers conformally-coated with $Ni(OH)_2$ nanoflakes exhibit five times higher specific capacitance compared to planar (non-conformal) $Ni(OH)_2$ nanoflakes electrodes prepared by drop casting of $Ni(OH)_2$ on the carbon microfibers (1416 F/g vs. 275 F/g).

- Ni-Cu-OH and Ni-Co-OH ternary electrodes have been prepared with different Ni:Cu and Ni:Co ratios by CBD at room temperature on carbon microfibers.

- It is observed that the electrodes with Ni:Cu and Ni:Co composition ratio of 100:10 results in an optimum capacitance and cycling stability. In

addition, it is found that decreasing Cu and Co ratios enhances nanoflakes formation, and hence increases electrode capacitance.

- For the optimum composition (Ni:Co = 100:10), Ni-Co-OH with graphene and carbon nanofibers (G-CNF) electrode was tested, with resultant improvement in electrode potential window, equivalent series resistance, and cyclic stability.

- $Ni(OH)_2$//Graphene and Ni-Co-OH/G-CNF//Graphene asymmetric supercapacitors have been fabricated at room temperature on carbon microfibers with KOH electrolyte.

- $Ni(OH)_2$//Graphene asymmetric supercapacitor results in an areal capacitance of 253 mF/cm^2 at 5 mA/cm^2 which is higher than reported 185 mF/cm^2 at 5 mA/cm^2 for NiO//rGO asymmetric supercapacitor prepared by hydrothermal method.

- Ni-Co-OH/G-CNF//Graphene asymmetric supercapacitor results in a maximum power of 23 mW within 2.2 V which are higher than the maximum power and the operating voltage of our $Ni(OH)_2$//Graphene (15.94 mW within 1.8 V).

- Our asymmetric supercapacitors are featured by not only their enhanced electrochemical performance, but also by their flexible-electrodes, low-cost fabrication process and environmentally friendly materials.

- A novel combination of top-down photolithographic process and bottom-up CBD synthesis has been developed to fabricate $Ni(OH)_2$-based micro supercapacitors (μ-supercapacitors).

- The resulting $Ni(OH)_2$-based devices show high-rate redox activity up to 500 V/s and an areal cell capacitance of 16 mF/cm^2 corresponding to a volumetric stack capacitance of 325 F/cm^3. This volumetric capacitance is 2-fold higher than carbon and metal oxide based μ-supercapacitors with interdigitated electrode architecture. Furthermore, these μ-supercapacitors show a maximum energy density of 21 mWh/cm^3, which is superior to the Li-based thin film batteries.

Future Directions

Our recommendation regarding the future research prospects can be summarized in the following points:

- It is recommended to utilize *in-situ* characterizing techniques to detect any morphological or structural changes on electrodes during charge-discharge processes. For example, electrochemical potentiostat and analytical electrochemistry TEM tip have been already combined for *in-situ* electrochemical studies.[107] Such detailed studies can provide further insight on the factors behind decreasing capacitance during prolong cycling.

- The effect of using different dopants with $Ni(OH)_2$ electrodes and different electrolytes can be investigated to further improve the device resistance, power and cycling stability.
- For our Ni-Co-OH/G-CNF conventional supercapacitors on carbon flexible substrate, we recommend to utilize the advantageous of substrate flexibility by designing and fabricating a cylindrical cell that can contain larger area of folded-in (scrolled) electrodes than in the stainless steel coin cell used in the research of this dissertation as an elementary prototype.
- For our $Ni(OH)_2$ on-chip supercapacitors on metallic/glass and flexible substrates, we recommend to add Co, graphene and carbon nanofibers to $Ni(OH)_2$. Such hybridizing may reduce the resistance, increase the power and cycling stability as have been achieved for our Ni-Co-OH/G-CNF conventional supercapacitors.

APPENDIX. TERMINOLGY

Capacitor "An Arrangement of conductors separated by an insulator (dielectric) used to store charge or introduce reactant into an alternating-current circuit."[108]

Capacitance "The property of a conductor or system of conductors that describes its ability to store electric charge. The capacitance *(C)* is given by *Q*/*V*, where *Q* is stored charge on one conductor and *V* the potential difference between the two conductors (or between a single conductor and earth); it is measured in farads."[108]

Cell " (in physical chemistry) A system in which two electrodes are in contact with an electrolyte. The electrodes are metals or carbon plates or rods or, in some cases, liquid metals (e.g. mercury). In an electrolytic cell a current from an outside source is passed through the electrolyte to produce chemical change. In a voltaic cell, spontaneous reactions between the electrodes and electrolyte(s) produce a potential difference between the two electrodes."[108]

Electrode "A conductor that emits or collects electrons in a cell."[108]

Electrode potential "The potential difference produced between the electrode and the solution in a half cell. It is not possible to measure this directly since any measurement involves completing the circuit with the electrolyte, thereby introducing another half cell. S*tandard electrode potentials* $E^{\varnothing}$; are defined by measuring the potential relative to a standard

hydrogen half cell using 1.0 molar solution in 25^{o}C. The convention is to designate the cell so that the oxidized form is written first. For example, $Pt(s)|H_2(g)H^+(aq)|Zn^{2+}(aq)|Zn(s)$ The e.m.f of this cell is -0.76 volt (i.e. the zinc electrode is negative). Thus the standard electrode potential of the $Zn^{2+}|Zn$ half cell is -0.76V. Electrode potentials are also called *reduction potentials.* "[108]

Electrolyte "A liquid that conducts electricity as a result of the presence of positive or negative ions. Electrolytes are molten ionic compunds or solutions containing ions, i.e. solution of ionic salts or of compounds that ionize in solution. Liquid metals, in which the conduction is by free electrons, are not usually regarding as electrolytes. Solid conductors of ions, as in the sodium-sulphur cell, are also known as electrolytes."[108]

Electromotive force (e.m.f) "The greatest potential difference that can be generated by a particular source of electric current. In practice this may be observable only when the source is not supplying current, because of its internal resistance."[108]

Energy "A measure of a system's ability to do work. Like work itself, it is measured in joules. Energy is conveniently classified into two forms: *potential energy* is the energy stored in a body or system as a consequence of its position, shape, or state (this includes gravitational energy, electrical energy, nuclear energy, and chemical energy); *kinetic energy* is energy of motion and

is usually defined as the work that will be done by the body possessing the energy when it is brought to rest."[108]

Half cell "An electrode in contact with a solution of ions, forming part of a cell. Various types of half cells exist, the simplest consisting of a metal electrode immersed in a solution of metal ions. Gas half cells have a gold or platinum plate in a solution with gas bubbled over the metal plate. The commonest is the hydrogen half cell. Half cells can also be formed by a metal in contact with an insoluble salt or oxide and a solution. The calomel half cell is an example of this. Half cells are commonly referred to as *electrodes*."[108]

Power (in physics) "Symbol *P*. The rate at which work is done or energy is transferred. In SI unit it is measured in watts (joules per seconds)."[108]

REFERENCES

1 BCC_Research. Supercapacitors: Technology Developments and Global Markets. Report No. EGY068A, *BCC Research*, Wellesley, MA, USA (2011).

2 BCC_Research. Supercapacitors: Technology Developments and Global Markets. Report No. EGY068B, *BCC Research*, Wellesley, MA, USA (2015).

3 Burke, A. Ultracapacitor technologies and application in hybrid and electric vehicles. *International Journal of Energy Research* **34**, 133-151, doi:10.1002/er.1654 (2010).

4 Kötz, R. & Carlen, M. Principles and applications of electrochemical capacitors. *Electrochimica Acta* **45**, 2483-2498, doi:10.1016/S0013-4686(00)00354-6 (2000).

5 Conway, B. E. Electrochemical Supercapacitors: Scientific Fundamentals and Technological Applications. *Springer* (1999).

6 Salunkhe, R. R. *et al.* Nanoarchitectured Graphene-Based Supercapacitors for Next-Generation Energy-Storage Applications. *Chemistry – A European Journal* **20**, 13838-13852, doi:10.1002/chem.201403649 (2014).

7 Faraji, S. & Ani, F. N. The development supercapacitor from activated carbon by electroless plating—A review. *Renewable and Sustainable Energy Reviews* **42**, 823-834, doi:10.1016/j.rser.2014.10.068 (2015).

8 Augustyn, V., Simon, P. & Dunn, B. Pseudocapacitive oxide materials for high-rate electrochemical energy storage. *Energy & Environmental Science* **7**, 1597-1614, doi:10.1039/c3ee44164d (2014).

9 Faraji, S. & Ani, F. N. Microwave-assisted synthesis of metal oxide/hydroxide composite electrodes for high power supercapacitors - A review. *Journal of Power Sources* **263**, 338-360, doi:10.1016/j.jpowsour.2014.03.144 (2014).

10 Feng, L., Zhu, Y., Ding, H. & Ni, C. Recent progress in nickel based materials for high performance pseudocapacitor electrodes. *Journal of Power Sources* **267**, 430-444, doi:10.1016/j.jpowsour.2014.05.092Review (2014).

11 Zhang, K. *et al.* Nanostructured Mn-based oxides for electrochemical energy storage and conversion. *Chemical Society Reviews* **44**, 699-728, doi:10.1039/c4cs00218k (2015).

12 Abdelhamid, M. E., O'Mullane, A. P. & Snook, G. A. Storing energy in plastics: a review on conducting polymers & their role in electrochemical energy storage. *RSC Advances* **5**, 11611-11626, doi:10.1039/c4ra15947k (2015).

13 V. D. Patake, C. D. L. a. O. S. J. Electrodeposited ruthenium oxide thin films for supercapacitor: Effect of surface treatments. *Appl. Surf. Sci.* **255**, 4192, doi:10.1016/j.apsusc.2008.11.005 (2009).

14 C. C. Hu, Y. H. H. a. K. H. C. Annealing effects on the physicochemical characteristics of hydrous ruthenium and ruthenium-iridium oxides for electrochemical supercapacitors. *J. Power Sources* **108**, 117, doi:10.1016/S0378-7753(02)00011-3 (2002).

15 J. Yan, T. W., J. Cheng, Z. Fan and M. Zhang. Preparation and electrochemical properties of lamellar MnO_2 for supercapacitors. *Mater. Res. Bull.* **45**, 210, doi:10.1016/j.materresbull.2009.09.016 (2010).

16 C. C. Hu, C. M. H. a. K. H. C. Anodic deposition of porous vanadium oxide network with highpower characteristics for pseudocapacitors. *J. Power Sources* **185**, 1594., doi:10.1016/j.jpowsour.2008.08.017 (2008).

17 Ivey., B. B. a. D. G. Anodic deposition of manganese oxide electrodes with rod-like structures for application as electrochemical capacitors. *J. Power Sources* **195**, 2110, doi:10.1016/j.jpowsour.2009.10.045 (2010).

18 Xia, X. *et al.* Graphene Sheet/Porous NiO Hybrid Film for Supercapacitor Applications. *Chemistry – A European Journal* **17**, 10898-10905, doi:10.1002/chem.201100727 (2011).

19 Patil, U. M., Salunkhe, R. R., Gurav, K. V. & Lokhande, C. D. Chemically deposited nanocrystalline NiO thin films for supercapacitor application. *Applied Surface Science* **255**, 2603-2607, doi:10.1016/j.apsusc.2008.07.192 (2008).

20 S. G. Kandalkar, J. L. G. a. C. D. L. Preparation of cobalt oxide thin films and its use in supercapacitor application. *Appl. Surf. Sci.* **254**, 5540, doi:10.1016/j.apsusc.2008.02.163 (2008).

21 Carbonio, R. E., Macango, V. A., Giordano, M. C., Vilche, J. R. & Arvia, A. J. A Transition in the Kinetics of the $Ni(OH)_2$ / NiOOH Electrode Reaction. *Journal of the Electrochemical Society* **129**, 983-991, doi:10.1149/1.2124077 (1982).

22 Brodd, R. in Batteries for Sustainability (ed Ralph J. Brodd) Ch. 13, 423-443, *Springer New York* (2013).

23 Brousse, T., Bélanger, D. & Long, J. W. To Be or Not To Be Pseudocapacitive? *Journal of the Electrochemical Society* **162**, A5185-A5189, doi:10.1149/2.0201505jes (2015).

24 Hu, G., Li, C. & Gong, H. Capacitance decay of nanoporous nickel hydroxide. *Journal of Power Sources* **195**, 6977-6981, doi:10.1016/j.jpowsour.2010.03.093 (2010).

25 Gong, L., Liu, X. & Su, L. Facile Solvothermal Synthesis $Ni(OH)_2$ Nanostructure for Electrochemical Capacitors. *Journal of Inorganic and Organometallic Polymers and Materials* **21**, 866-870, doi:10.1007/s10904-011-9519-1 (2011).

26 Li, H. *et al.* Characterization and supercapacitor application of coin-like β-nickel hydroxide nanoplates. *Electrochimica Acta* **58**, 89-94, doi:10.1016/j.electacta.2011.08.120 (2011).

27 Lu, Z., Chang, Z., Zhu, W. & Sun, X. Beta-phased $Ni(OH)_2$ nanowall film with reversible capacitance higher than theoretical Faradic capacitance. *Chemical Communications* **47**, 9651-9653, doi:10.1039/C1CC13796D (2011).

28 Yan, H. *et al.* l-Lysine assisted synthesis of β-$Ni(OH)_2$ hierarchical hollow microspheres and their enhanced electrochemical capacitance performance. *Electrochimica Acta* **87**, 880-888, doi:10.1016/j.electacta.2012.08.090 (2013).

29 Patil, U. M., Gurav, K. V., Fulari, V. J., Lokhande, C. D. & Joo, O. S. Characterization of honeycomb-like "β-$Ni(OH)_2$" thin films synthesized by chemical bath deposition method and their supercapacitor application. *Journal of Power Sources* **188**, 338-342, doi:10.1016/j.jpowsour.2008.11.136 (2009).

30 Dubal, D. P., Fulari, V. J. & Lokhande, C. D. Effect of morphology on supercapacitive properties of chemically grown β-$Ni(OH)_2$ thin films. *Microporous and Mesoporous Materials* **151**, 511-516, doi:10.1016/j.micromeso.2011.08.034 (2012).

31 Yuan, Y. F. *et al.* Nickel foam-supported porous $Ni(OH)_2$/NiOOH composite film as advanced pseudocapacitor material. *Electrochimica Acta* **56**, 2627-2632, doi:10.1016/j.electacta.2010.12.001 (2011).

32 Pramanik, P. & Bhattacharya, S. A Chemical Method for the Deposition of Nickel Oxide Thin Films. *Journal of the Electrochemical Society* **137**, 3869-3870, doi:10.1149/1.2086316 (1990).

33 Bukovec, P., Bukovec, N., Orel, B. & Wissiak, K. Thermal analysis of nickel oxide films. *Journal of Thermal Analysis and Calorimetry* **40**, 1193-1196, doi:10.1007/BF02546882 (1993).

34 Salunkhe, R. R. *et al.* Large-scale synthesis of coaxial carbon nanotube/$Ni(OH)_2$ composites for asymmetric supercapacitor application. *Nano Energy* **11**, 211-218, doi:10.1016/j.nanoen.2014.09.030 (2015).

35 Tang, Z., Tang, C.-h. & Gong, H. A High Energy Density Asymmetric Supercapacitor from Nano-architectured $Ni(OH)_2$/Carbon Nanotube Electrodes. *Advanced Functional Materials* **22**, 1272-1278, doi:10.1002/adfm.201102796 (2012).

36 Sun, X. *et al.* Morphology controlled high performance supercapacitor behaviour of the Ni–Co binary hydroxide system. *Journal of Power Sources* **238**, 150-156, doi:10.1016/j.jpowsour.2013.03.069 (2013).

37 Tang, C.-h., Yin, X. & Gong, H. Superior Performance Asymmetric Supercapacitors Based on a Directly Grown Commercial Mass 3D Co_3O_4@$Ni(OH)_2$ Core–Shell Electrode. *ACS Applied Materials & Interfaces* **5**, 10574-10582, doi:10.1021/am402436q (2013).

38 Chae, J. H., Ng, K. C. & Chen, G. Z. Nanostructured materials for the construction of asymmetrical supercapacitors. *Proceedings of the Institution of Mechanical Engineers, Part A: Journal of Power and Energy* **224**, 479-503, doi:10.1243/09576509jpe861 (2010).

39 Yan, J. *et al.* Advanced Asymmetric Supercapacitors Based on $Ni(OH)_2$/Graphene and Porous Graphene Electrodes with High Energy Density. *Advanced Functional Materials* **22**, 2632-2641, doi:10.1002/adfm.201102839 (2012).

40 Schneller, T., Waser, R., Kosec, M. & Payne, D. CHEMICAL SOLUTION DEPOSITION OF FUNCTIONAL OXIDE THIN FILMS. 319 (*Springer-Verlag Wien,* 2013).

41 Bukovec, P., Bukovec, N., Orel, B. & Wissiak, K. S. Thermal analysis of nickel oxide films. *Journal of Thermal Analysis* **40**, 1193-1196, doi:10.1007/bf02546882 (1993).

42 Han, S.-Y. *et al.* The Growth Mechanism of Nickel Oxide Thin Films by Room-Temperature Chemical Bath Deposition. *Journal of the Electrochemical Society* **153**, C382-C386, doi:10.1149/1.2186767 (2006).

43 An, X. *et al.* Stable Aqueous Dispersions of Noncovalently Functionalized Graphene from Graphite and their Multifunctional High-Performance Applications. *Nano Letters* **10**, 4295-4301, doi:10.1021/nl903557p (2010).

44 Viculis, L. M., Mack, J. J. & Kaner, R. B. A Chemical Route to Carbon Nanoscrolls. *Science* **299**, 1361, doi:10.1126/science.1078842 (2003).

45 Adams, T. M. & Layton, R. A. INTRODUCTORY MEMS-Fabrication and Applications. 65, *Springer Science+Business Media* (2010).

46 Will, K. Photoresists, *MicroChemicals GmbH Company*, <http://www.microchemicals.com/products/photoresists.html> (2015).

47 Egerton, R. F. *Physical Principles of Electron Microscopy*. 11, *Springer Science+Business Media, Inc.* (2005).

48 Hammond, C. Basics of Crystallography and Diffraction. *OUP Oxford* (2009).

49 Leng, Y. Materials Characterization Introduction to Microscopic and Spectroscopic Methods. 2 edn, 5-7, *Wiley-VCH Verlag GmbH & Co.* (2013).

50 Béguin, F. & Frąckowiak, E. 115-120, Wiley-VCH Verlag GmbH & Co. KGaA, Weinheim, Germani (2013).

51 Conway, B. E. *Electrochemical Supercapacitors: Scientific Fundamentals and Technological Applications*. 6-7, Springer (1999).

52 Jiang, H., Lee, P. S. & Li, C. 3D carbon based nanostructures for advanced supercapacitors. *Energy and Environmental Science* **6**, 41-53, doi:10.1039/c2ee23284g (2013).

53 Deng, W., Ji, X., Chen, Q. & Banks, C. E. Electrochemical capacitors utilising transition metal oxides: An update of recent developments. *RSC Advances* **1**, 1171-1178, doi:10.1039/c1ra00664a (2011).

54 Yin, Z. & Zheng, Q. Controlled synthesis and energy applications of one-dimensional conducting polymer nanostructures: An overview. *Advanced Energy Materials* **2**, 179-218, doi:10.1002/aenm.201100560 (2012).

55 Deshmukh, P. R., Pusawale, S. N., Jagadale, A. D. & Lokhande, C. D. Supercapacitive performance of hydrous ruthenium oxide ($RuO_2 \bullet nH_2O$) thin films deposited by SILAR method. *Journal of Materials Science* **47**, 1546-1553, doi:10.1007/s10853-011-5946-1 (2012).

56 Patil, U. M., Gurav, K. V., Fulari, V. J., Lokhande, C. D. & Joo, O. S. Characterization of honeycomb-like "β-$Ni(OH)_2$" thin films synthesized by chemical bath deposition method and their supercapacitor application. *Journal of Power Sources* **188**, 338-342, doi:10.1016/j.jpowsour.2008.11.136 (2009).

57 Dubal, D. P., Fulari, V. J. & Lokhande, C. D. Effect of morphology on supercapacitive properties of chemically grown β-$Ni(OH)_2$ thin films. *Microporous and Mesoporous Materials* **151**, 511-516, doi:10.1016/j.micromeso.2011.08.034 (2012).

58 Yuan, Y. F. *et al.* Nickel foam-supported porous $Ni(OH)_2$/NiOOH composite film as advanced pseudocapacitor material. *Electrochimica Acta* **56**, 2627-2632, doi:10.1016/j.electacta.2010.12.001 (2011).

59 Kamath, P. V. *et al.* Stabilized α-$Ni(OH)_2$ as Electrode Material for Alkaline Secondary Cells. *Journal of the Electrochemical Society* **141**, 2956-2959, doi:10.1149/1.2059264 (1994).

60 Watanabe, K.-i., Koseki, M. & Kumagai, N. Effect of cobalt addition to nickel hydroxide as a positive material for rechargeable alkaline batteries. *Journal of Power Sources* **58**, 23-28, doi:10.1016/0378-7753(95)02272-4 (1996).

61 Chen, J., Bradhurst, D. H., Dou, S. X. & Liu, H. K. Nickel Hydroxide as an Active Material for the Positive Electrode in Rechargeable Alkaline Batteries. *Journal of the Electrochemical Society* **146**, 3606-3612, doi:10.1149/1.1392522 (1999).

62 Liu, B., Zhang, Y., Yuan, H., Yang, H. & Yang, E. Electrochemical studies of aluminum substituted α-$Ni(OH)_2$ electrodes. *International Journal of Hydrogen Energy* **25**, 333-337, doi:10.1016/S0360-3199(99)00026-9 (2000).

63 Jayashree, R. S. & Vishnu Kamath, P. Suppression of the α → β-nickel hydroxide transformation in concentrated alkali: Role of dissolved cations. *Journal of Applied Electrochemistry* **31**, 1315-1320, doi:10.1023/a:1013876006707 (2001).

64 Lien, C. H., Hu, C. C., Hsu, C. T. & Wong, D. S. H. High-performance asymmetric supercapacitor consisting of Ni-Co-Cu oxy-hydroxide nanosheets and activated carbon. *Electrochemistry Communications* **34**, 323-326, doi:10.1016/j.elecom.2013.07.032 (2013).

65 Alhebshi, N. A., Rakhi, R. B. & Alshareef, H. N. Conformal coating of $Ni(OH)_2$ nanoflakes on carbon fibers by chemical bath deposition for efficient supercapacitor electrodes. *Journal of Materials Chemistry A* **1**, 14897-14903, doi:10.1039/C3TA12936E (2013).

66 Zhang, L., Tang, C., Yin, X. & Gong, H. Substrate-assisted self-organization of Ni-Cu spherical double hydroxide (SDH) and its excellent pseudo-capacitive performance. *Journal of Materials Chemistry A* **2**, 4660-4666, doi:10.1039/c3ta14374k (2014).

67 Bai, Y., Rakhi, R. B., Chen, W. & Alshareef, H. N. Effect of pH-induced chemical modification of hydrothermally reduced graphene oxide on supercapacitor performance. *Journal of Power Sources* **233**, 313-319, doi:10.1016/j.jpowsour.2013.01.122 (2013).

68 Bode, H., Dehmelt, K. & Witte, J. Zur kenntnis der nickelhydroxidelektrode—I.Über das nickel (II)-hydroxidhydrat. *Electrochimica Acta* **11**, 1079-IN1071, doi:10.1016/0013-4686(66)80045-2 (1966).

69 Luan, F. *et al.* High energy density asymmetric supercapacitors with a nickel oxide nanoflake cathode and a 3D reduced graphene oxide anode. *Nanoscale* **5**, 7984-7990, doi:10.1039/C3NR02710D (2013).

70 Drexler, K. E. *Engines of Creation -The Coming Era of Nanotechnology*. Anchor, Reprint edition edn, (1987).

71 Wang, Z. L. Toward self-powered sensor networks. *Nano Today* **5**, 512-514, doi:10.1016/j.nantod.2010.09.001 (2010).

72 Simjee, F. & Chou, P. H. in Low Power Electronics and Design, ISLPED'06. *Proceedings of the 2006 International Symposium on.* 197-202 (2006).

73 Wang, Z. L. & Wu, W. Nanotechnology-Enabled Energy Harvesting for Self-Powered Micro-/Nanosystems. *Angewandte Chemie International Edition* **51**, 11700-11721, doi:10.1002/anie.201201656 (2012).

74 Beidaghi, M. & Gogotsi, Y. Capacitive energy storage in micro-scale devices: recent advances in design and fabrication of micro-supercapacitors. *Energy & Environmental Science* **7**, 867-884, doi:10.1039/c3ee43526a (2014).

75 Xiong, G., Meng, C., Reifenberger, R. G., Irazoqui, P. P. & Fisher, T. S. A Review of Graphene-Based Electrochemical Microsupercapacitors. *Electroanalysis* **26**, 30-51, doi:10.1002/elan.201300238 (2014).

76 Li, Y., Xie, H., Li, J. & Wang, J. Magnetron sputtering deposited $MnO_{1.9}$ thin film for supercapacitor. *Materials Letters* **102–103**, 30-32, doi:10.1016/j.matlet.2013.03.098 (2013).

77 Yoo, J. J. *et al.* Ultrathin Planar Graphene Supercapacitors. *Nano Letters* **11**, 1423-1427, doi:10.1021/nl200225j (2011).

78 Gao, W. *et al.* Direct laser writing of micro-supercapacitors on hydrated graphite oxide films. *Nat Nano* **6**, 496-500, doi:10.1038/nnano.2011.110 (2011).

79 Long, J. W., Dunn, B., Rolison, D. R. & White, H. S. Three-Dimensional Battery Architectures. *Chemical Reviews* **104**, 4463-4492, doi:10.1021/cr020740l (2004).

80 Miller, J. R., Outlaw, R. A. & Holloway, B. C. Graphene Double-Layer Capacitor with ac Line-Filtering Performance. *Science* **329**, 1637-1639, doi:10.1126/science.1194372 (2010).

81 Pech, D. *et al.* Ultrahigh-power micrometre-sized supercapacitors based on onion-like carbon. *Nat Nano* **5**, 651-654, doi:10.1038/nnano.2010.162 (2010).

82 El-Kady, M. F. & Kaner, R. B. Scalable fabrication of high-power graphene micro-supercapacitors for flexible and on-chip energy storage. *Nat Commun* **4**, 1475, doi:10.1038/ncomms2446 (2013).

83 Pech, D. *et al.* Elaboration of a microstructured inkjet-printed carbon electrochemical capacitor. *Journal of Power Sources* **195**, 1266-1269, doi:10.1016/j.jpowsour.2009.08.085 (2010).

84 Xue, M. *et al.* Structure-Based Enhanced Capacitance: In Situ Growth of Highly Ordered Polyaniline Nanorods on Reduced Graphene Oxide Patterns. *Advanced Functional Materials* **22**, 1284-1290, doi:10.1002/adfm.201101989 (2012).

85 Sung, J.-H., Kim, S.-J. & Lee, K.-H. Fabrication of microcapacitors using conducting polymer microelectrodes. *Journal of Power Sources* **124**, 343-350, doi:10.1016/S0378-7753(03)00669-4 (2003).

86 Chmiola, J., Largeot, C., Taberna, P.-L., Simon, P. & Gogotsi, Y. Monolithic Carbide-Derived Carbon Films for Micro-Supercapacitors. *Science* **328**, 480-483, doi:10.1126/science.1184126 (2010).

87 Lin, J. *et al.* 3-Dimensional Graphene Carbon Nanotube Carpet-Based Microsupercapacitors with High Electrochemical Performance. *Nano Letters* **13**, 72-78, doi:10.1021/nl3034976 (2013).

88 Si, W. *et al.* On chip, all solid-state and flexible micro-supercapacitors with high performance based on MnO_x/Au multilayers. *Energy & Environmental Science* **6**, 3218-3223, doi:10.1039/c3ee41286e (2013).

89 Beidaghi, M. & Wang, C. Micro-Supercapacitors Based on Interdigital Electrodes of Reduced Graphene Oxide and Carbon Nanotube Composites with Ultrahigh Power Handling Performance. *Advanced Functional Materials* **22**, 4501-4510, doi:10.1002/adfm.201201292 (2012).

90 Huang, P. *et al.* Micro-supercapacitors from carbide derived carbon (CDC) films on silicon chips. *Journal of Power Sources* **225**, 240-244, doi:10.1016/j.jpowsour.2012.10.020 (2013).

91 Wu, Z. S., Parvez, K., Feng, X. & Müllen, K. Graphene-based in-plane micro-supercapacitors with high power and energy densities. *Nat Commun* **4**, doi:10.1038/ncomms3487 (2013).

92 Dinh, T. M., Armstrong, K., Guay, D. & Pech, D. High-resolution on-chip supercapacitors with ultra-high scan rate ability. *Journal of Materials Chemistry A* **2**, 7170-7174, doi:10.1039/c4ta00640b (2014).

93 Sung, J.-H., Kim, S.-J. & Lee, K.-H. Fabrication of all-solid-state electrochemical microcapacitors. *Journal of Power Sources* **133**, 312-319, doi:10.1016/j.jpowsour.2004.02.003 (2004).

94 Cao, L. *et al.* Direct Laser-Patterned Micro-Supercapacitors from Paintable MoS_2 Films. *Small* **9**, 2905-2910, doi:10.1002/smll.201203164 (2013).

95 Wang, K. *et al.* An All-Solid-State Flexible Micro-supercapacitor on a Chip. *Advanced Energy Materials* **1**, 1068-1072, doi:10.1002/aenm.201100488 (2011).

96 Shen, C., Wang, X., Zhang, W. & Kang, F. A high-performance three-dimensional micro supercapacitor based on self-supporting composite materials. *Journal of Power Sources* **196**, 10465-10471, doi:10.1016/j.jpowsour.2011.08.007 (2011).

97 Salunkhe, R. R., Jang, K., Lee, S.-w. & Ahn, H. Aligned nickel-cobalt hydroxide nanorod arrays for electrochemical pseudocapacitor applications. *RSC Advances* **2**, 3190-3193, doi:10.1039/c2ra01220k (2012).

98 Patil, U. M., Gurav, K. V., Kim, J. H., Lokhande, C. D. & Jun, S. C. Bath temperature impact on morphological evolution of $Ni(OH)_2$ thin films and their supercapacitive behaviour. *Bull Mater Sci* **37**, 27-33, doi:10.1007/s12034-014-0617-x (2014).

99 Vidales-Hurtado, M. A. & Mendoza-Galván, A. Electrochromism in nickel oxide-based thin films obtained by chemical bath deposition. *Solid State Ionics* **179**, 2065-2068, doi:10.1016/j.ssi.2008.07.003 (2008).

100 Shieh, S. R. & Duffy, T. S. Raman spectroscopy of $Co(OH)_2$ at high pressures: Implications for amorphization and hydrogen repulsion. *Physical Review B* **66**, 134301, doi:10.1103/PhysRevB.66.134301 (2002).

101 Nam, K.-W., Lee, E.-S., Kim, J.-H., Lee, Y.-H. & Kim, K.-B. Synthesis and Electrochemical Investigations of $Ni_{1-x}O$ Thin Films and $Ni_{1-x}O$ on Three-Dimensional Carbon Substrates for Electrochemical Capacitors. *Journal of the Electrochemical Society* **152**, A2123-A2129, doi:10.1149/1.2039647 (2005).

102 Dong, X. *et al.* Flexible and Wire-Shaped Micro-Supercapacitor Based on $Ni(OH)_2$-Nanowire and Ordered Mesoporous Carbon Electrodes. *Advanced Functional Materials* **24**, 3405-3412, doi:10.1002/adfm.201304001 (2014).

103 Xie, J. *et al.* Layer-by-layer β-$Ni(OH)_2$/graphene nanohybrids for ultraflexible all-solid-state thin-film supercapacitors with high electrochemical performance. *Nano Energy* **2**, 65-74, doi:10.1016/j.nanoen.2012.07.016 (2013).

104 Kurra, N., Kiruthika, S. & Kulkarni, G. U. Solution processed sun baked electrode material for flexible supercapacitors. *RSC Advances* **4**, 20281-20289, doi:10.1039/c4ra02934h (2014).

105 Wang, Y.-M., Zhao, D.-D., Zhao, Y.-Q., Xu, C.-L. & Li, H.-L. Effect of electrodeposition temperature on the electrochemical performance of a $Ni(OH)_2$ electrode. *RSC Advances* **2**, 1074-1082, doi:10.1039/C1RA00613D (2012).

106 Wang, X. *et al.* Manganese oxide micro-supercapacitors with ultra-high areal capacitance. *Nanoscale* **5**, 4119-4122, doi:10.1039/c3nr00210a (2013).

107 Team, H. S. C. Analytical electrochemistry TEM tip, *Hummingbird Scientific Company*, <http://hummingbirdscientific.com/products/liquid/liquid-system-electrochemistry/> (2015).

108 Isaacs, A. Dictionary of Physics. 6th edn, *Constable and Robinson Ltd* (2005).